Effects of microRNA overexpression on cone photoreceptor survival and structure in health and disease

Doctoral thesis

to obtain a doctorate PhD

from the Faculty of Medicine

of the University of Bonn

Julia Sophie Pawlick

from Kreuztal, Germany

2025

Written with authorization of

the Faculty of Medicine of the University of Bonn

First reviewer: Prof. Dr. Volker Busskamp

Second reviewer: Prof. Dr. Dr. Knut Stieger

Day of oral examination: 16.12.2024

From the University eye hospital Bonn

Director: Prof. Dr. Frank G. Holz

Table of Contents

List of abbreviations

3' UTR	3' untranslated region
5s rRNA	5S ribosomal rRNA
AAV	Adeno-associated virus
AC	Amacrine cells
ACTB	Actin-beta
AGO	Argonaute
AMASS	Agarose microwell array seeding and scraping
AMD	Age-related macular degeneration
ARR3	Retinal cone arrestin-3
ARR3+	Retinal cone arrestin-3 positive
BC	Bipolar cells
bp	Base pairs
BRN3A	Brain-specific homeobox/POU domain protein 3A
Carb	Carbenicillin
Casp2	Caspase-2
CC	Connecting cilium
cDNA	Complementary DNA
CEPT	Chroman 1, emricasan, polyamines, trans-ISRIB
cGMP	Cyclic guanosine monophosphate
CNG	Cyclic nucleotide-gated
cpfl9	Cone photoreceptor function loss 9
C_T	Threshold cycle
ddH_2O	Double-distilled water
DGCR8	DiGeorge critical region 8
DMEM	Dulbecco’s modified Eagle medium
DMSO	Dimethyl sulfoxide
DOX	Doxycycline
dpi	Days post induction
DPT	Days post-transduction
DR	Diabetic retinopathy

E. coli	Escherichia coli
eGFP	Enhanced green fluorescent protein
eGFP+	Enhanced green fluorescent protein positive
ER	Endoplasmic reticulum
FACS	Fluorescent-activated cell sorting
FBS	Fetal bovine serum
fps	Frames per second
G	Gauge
GA	Gibson assembly
GC	Guanylyl cyclase
GCL	Ganglion cell layer
GDP	Guanosine diphosphate
GMP	Guanosine monophosphate
GTP	Guanosine triphosphate
h	Hours
hBG	Human beta-globin
HC	Horizontal cells
hiPSC	Human induced pluripotent stem cell
hCAR	Human cone arrestin promoter
hRO	Human stem-cell derived retinal organoids
hsa	Homo sapiens
IDT	Integrated DNA Technologies
iNGN	Inducible neurogenin
INL	Inner nuclear layer
IP	Intraperitoneally
IPL	Inner plexiform layer
IRD	Inherited retinal diseases
IS	Inner segment
ITR	Inverted terminal repeats
kb	Kilobases
LB	Lysogeny Broth
LCA	Leber congenital amaurosis

lncRNA Rncr4	Long non-coding RNA retinal non-coding RNA 4
LV	Lentiviral
mCAR	Mouse cone arrestin
MCP-1	Monocyte chemotactic protein-1
MEA	Multi-electrode array
mESC	Mouse embryonic stem-cell
min	Minutes
miRNAs	microRNAs
miRNomes	miRNA transcriptomes
mRNA	Messenger RNA
NaCl	Sodium chloride
NDS	Normal donkey serum
nt	Nucleotides
OMR	Optomotor reflex
ONL	Outer nuclear layer
OPL	Outer plexiform layer
OS	Outer segments
pA	Polyadenylation
PAP	Peroxidase-antiperoxidase
PB	PiggyBac
PBS	Phosphate-buffered saline
PCR	Polymerase chain reaction
PDE	Phosphodiesterase
Pde6b	Phosphodiesterase 6B
Pen/Strep	Penicillin/Streptomycin
PET	Polyethylene terephthalate
PFA	Paraformaldehyde
PKCα	Protein Kinase C - alpha
PR	Photoreceptors
pre-miRNA	Precursor miRNA
pre-mRNA	Precursor messenger RNA
pri-miRNA	Primary miRNA

Puro	Puromycin
rd1	Retinal degeneration mouse 1
RE	Restriction enzyme
RGC	Retinal ganglion cells
RHO	Rhodopsin
RISC	RNA-induced silencing complex
RNAi	RNA interference
ROS	Reactive oxygen species
RP	Retinitis pigmentosa
RPE	Retinal pigment epithelial
RPPH1	Ribonuclease P RNA component H1
RT	Room temperature
rtTA	Reverse tetracycline-controlled transactivator
RT-qPCR	Real-Time-quantitative polymerase chain reaction
s	Seconds
SC	Subcutaneously
shNTC	Short hairpin non-targeting control, short hairpin non-targeting control
shRNA	Short-hairpin RNA
siRNAs	Small interfering RNAs
SLO	Scanning laser ophthalmoscopy
SNRPD3	Small nuclear ribonucleoprotein Sm D3
SOC	Super Optimal Broth with Catabolite Repression
TEM	Transmission electron microscopy
TEs	Transposable elements
TetON	Tetracycline ON
TRBP	Trans-activation response RNA-binding protein
WPT	Weeks post transduction
WT	Wild type
XPO5	Exportin-5

1 Introduction

1.1 The Retina

The retina is a multilayered sensory neural tissue located at the back of the eye and conserved in vertebrates (Hoon et al., 2014). The retinal structure is illustrated in Fig. 1.1. It is composed of five major neuronal classes: photoreceptors (PR), bipolar cells (BC), horizontal cells (HC), amacrine cells (AC), and retinal ganglion cells (RGC). The nuclei of retinal cells are organized into three distinct nuclear layers. The outer nuclear layer (ONL) contains the PRs, while the inner nuclear layer (INL) contains the BCs, HCs, and ACs (collectively referred to as interneurons). The ganglion cell layer (GCL) contains the RGCs. These three layers are separated by two plexiform layers that contain the synapses between the different cell types. The outer plexiform layer (OPL) consists of synaptic connections between PRs, BCs, and HCs. The inner plexiform layer (IPL) contains the synapses formed between BCs and ACs as well as RGCs (DeVries and Baylor, 1993). PRs are located in the outer part of the retina and capture light with their outer segments (OS) after the light has passed through the inner retinal layers. The light is then converted into electrochemical signals that are transmitted to cells in the INL (Bonezzi et al., 2020). There are two types of PRs that sense light under different light conditions. Cone photoreceptors are responsible for color vision (photopic vision) and resolve fine details during the day, while rod photoreceptors are responsible for vision in dim light conditions (scotopic vision) (Lamb, 2016; Pearring et al., 2013). Both photoreceptor types share a common structural organization that includes an outer segment (OS), connecting cilium (CC), inner segment (IS), cell body, and synaptic terminals (Perkins and Fadool, 2010). In rods, the OS consists of a plasma membrane enclosing over 1000 stacked discs, each of which is a closed structure. In contrast, cone OS are formed by invaginations of the plasma membrane (Molday and Moritz, 2015; Kennedy and Malicki, 2009; Ding et al., 2015; Veleri et al., 2015). The vertebrate retina has only one type of rods, which contains the photopigment rhodopsin (RHO) in its disc membranes, with an absorption peak at about 500 nm (Lin et al., 1998). Cones form synapses with ON and OFF cone BCs, resulting in an ON depolarizing response or an OFF hyperpolarizing response at the BC membranes (Popova, 2014). Finally, the BCs transmit the information to the RGCs. Rods,

in turn, transmit signals to rod BCs and form synapses with ACs. The ACs can then divide these signals via gap junctions to ON and OFF cone bipolar cells and finally transmit the signals to their ON or OFF RGCs (Whitaker et al., 2021; Bloomfield and Völgyi, 2009). RGC axons project along the inner retinal layer to the optic nerve head, where they exit the eye to form the optic nerve, which consists of more than one million axons and projects to the brain (Yu et al., 2013; Huang et al., 2023). In addition, glial cells known as Müller glial cells are present in the retina (Masland, 2012). These cells project throughout the retinal layers and interact with every neuron in the retina (Kobat and Turgut, 2020). They occupy the spaces not filled by neurons and perform important functions such as metabolic functions, homeostasis, and survival of retinal neurons by secreting neurotrophic factors (Bringmann et al., 2006). The retinal pigment epithelial (RPE) cells are the second type of non-neuronal cells in the retina. RPE cells are pigmented cells located in the outermost layer of the retina, with their inner side adjacent to the PRs and their outer side adjacent to Bruch's membrane, which separates the RPE from the choroid (Yang et al., 2021). The choroid is essential for nutrient and oxygen supply to the outer retina (Nickla and Wallman, 2010). The RPE forms the outer blood-retinal barrier, which contributes to the immune privilege of the retina (Simó et al., 2010). The RPE plays an important role in the reduction of reactive oxygen species (ROS), photoreceptor maintenance and function, including phagocytosis and rebuilding of the OS of PRs, transport of metabolites to PRs, maintenance of the visual cycle, and release of growth factors (B Domènech and Marfany, 2020; Strauss, 2005; Baehr et al., 2003).

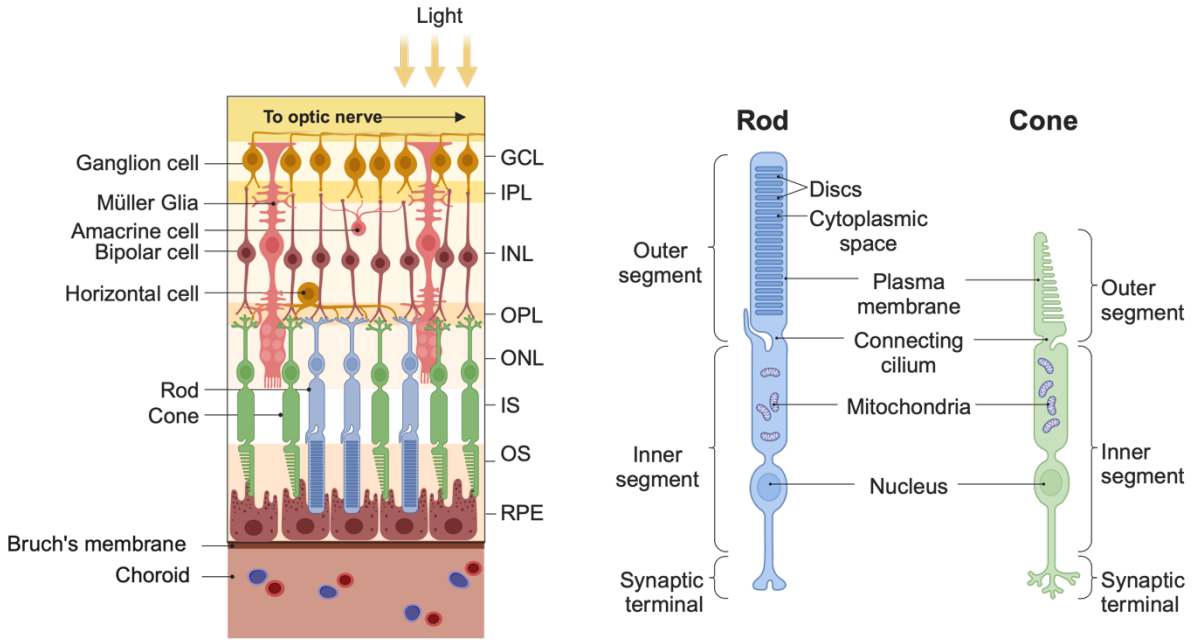

Fig. 1.1 Retina and photoreceptor structure. Light travels through the various retinal layers until it is detected by photopigments in the OS. It is converted into electrochemical signals that are transmitted to bipolar, horizontal and amacrine cells in the INL. Horizontal cells modulate signals between photoreceptors and bipolar cells, while amacrine cells modulate signals before they reach the retinal ganglion cells. RPE and Müller glial cells are essential for retinal homeostasis, function, and survival. Bruch's membrane separates RPE cells from the choroid. The choroid is essential for nutrient and oxygen delivery to the outer retina. The photoreceptors consist of OS, IS, and synaptic terminals with key components labeled. The OS contain the photopigments. (Adapted from “Structure of the Retina” and “Morphology of Photoreceptors”, by BioRender.com (2024). Retrieved from https://app.biorender.com/biorender-templates.apos)

1.2 Photoreceptor function

The human retina has three cone subtypes, each with a different opsin for detecting specific peak wavelengths: the long wavelength/red sensitive (L-opsin, 564 nm), the medium wavelength/green sensitive (M-opsin, 533 nm) and the short wavelength/blue sensitive (S-opsin, 437 nm). These subtypes enable trichromatic color vision (Jacobs, 2009). In contrast, the mouse retina contains only two subtypes: M-cones with a peak wavelength of 508 nm and S-cones, with a peak wavelength of 360 nm, resulting in dichromatic vision (Schwartz, 2021). S-cones are distributed differently across the mouse retina, with S-cones highly concentrated in the ventral regions, allowing color vision in the

upper visual field, and M-cones more concentrated in the dorsal regions (Privalov and Crane-Robinson, 2020; Applebury et al., 2000). The CC is the link between the OS and the IS and is involved in protein trafficking to the OS. The IS carries the mitochondria, the endoplasmic reticulum (ER), the Golgi complex, lysosomes, and other subcellular organelles. The cell body contains the nucleus. The synaptic regions harbor synaptic vesicles and ribbon synapses that facilitate the release of neurotransmitters, primarily glutamate, to bipolar cells or other neurons (Molday and Moritz, 2015). The human retina contains about 120 million rods and 6 million cones. Cones have a high density in the central region of the retina known as the macula, especially in its center, the fovea, the point of highest visual acuity (Molday and Moritz, 2015; Wells-Gray et al., 2016). Mice have a rod-dominated retina. 97.2 % of all photoreceptors are rods and only 2.8 % are cones (Jeon et al., 1998). A higher proportion of rods is an evolutionary adaptation to the nocturnal nature of mice and supports their activity in low light conditions (Verra et al., 2020). Consequently, mice do not have a macula or an area of high cone density (Fletcher et al., 2014). Although the composition of cones in mice differs from that in humans, the processes of the phototransduction cascade are similar (Invergo et al., 2013). The phototransduction cascade is illustrated in Fig. 1.2. Phototransduction occurs in the OS of PRs when photopigments in the disc membranes detect a photon, which changes the membrane potential and affects neurotransmitter release at the synapse (Purves and Williams, 2001). Photon detection triggers a conformational change in retinal, a chromophore attached to the photopigments, causing it to isomerize from 11-*cis* retinal to all-*trans* retinal. This isomerization activates the G-protein transducin, which exchanges guanosine diphosphate (GDP) for guanosine triphosphate (GTP) on its α-subunit. The activated transducin then stimulates phosphodiesterase (PDE), which hydrolyzes cyclic guanosine monophosphate (cGMP) to guanosine monophosphate (GMP). The resulting decrease in cGMP levels causes the closure of cGMP-gated channels, resulting in decreased intracellular Sodium (Na^+) and Calcium (Ca^{2+}) levels. This decrease hyperpolarizes the OS membrane and reduces neurotransmitter release at PR synapses. In darkness, PRs remain depolarized due to high levels of cGMP that keep the cGMP-gated channels open. Guanylyl cyclase (GC) restores cGMP levels by synthesizing cGMP from GTP, reopening the cGMP-gated channels and returning the PRs to the depolarized state typical of dark conditions (Butryn et al., 2020).

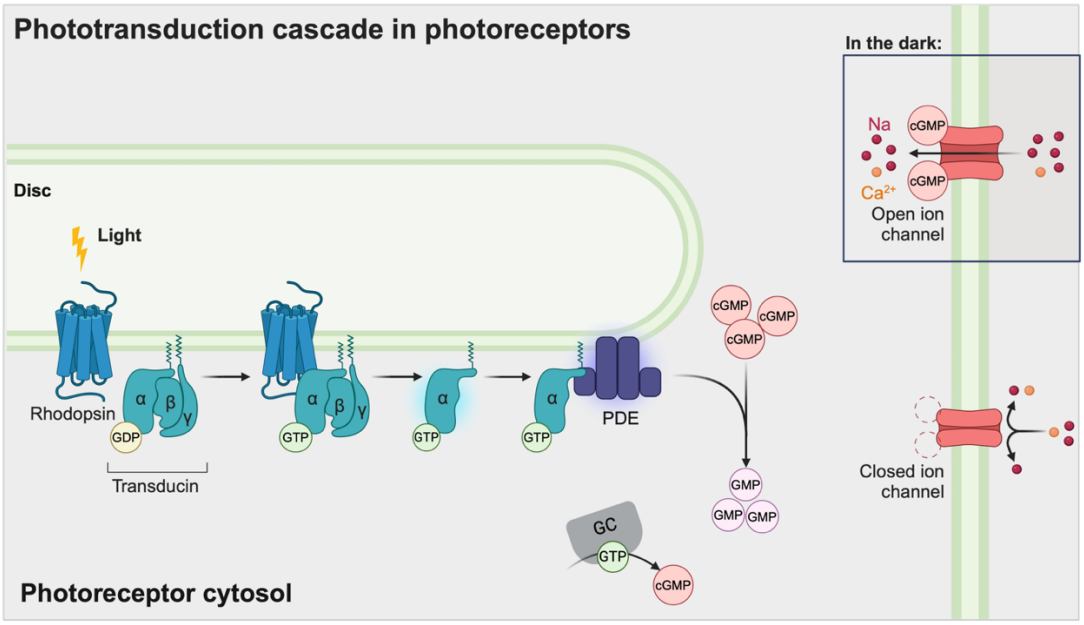

Fig. 1.2 Phototransduction cascade. A photon is detected by photopigments in the OS disc membranes. This initiates a conformational change in the retinal chromophore, converting 11-*cis* to all-*trans* retinal. This change activates the G-protein transducin by exchanging GDP for GTP on its α-subunit. Activated transducin stimulates PDE, which hydrolyzes cGMP to GMP, resulting in a decrease in intracellular cGMP. This reduction causes closure of cGMP-gated channels, resulting in hyperpolarization of the PR membrane and reduced neurotransmitter release at the synaptic terminals of the PRs. GC then restores cGMP levels from GTP, resulting in reopening of the channels and the return of the PRs to their depolarized state. (Adapted from "Phototransduction in Photoreceptors" by BioRender.com (2024). Retrieved from https://app.biorender.com/biorender-templates.apos)

1.3 Retinitis pigmentosa and other photoreceptor-related retinal disorders

The function of PRs is essential for providing visual input to the brain. They are the largest population of neurons in the eye, representing 80 % of the total population (Gasparini et al., 2019). Degeneration of these cells has deleterious effects that inevitably lead to vision loss. Age-related macular degeneration (AMD) is the most common form of acquired PR degeneration affecting primarily older individuals in the Western world, resulting in loss of central vision at later stages, especially due to the loss of cones in the foveal region, the central part of the macula (Gheorghe et al., 2015; Bakri et al., 2023). Both environmental and genetic factors are known risk factors for the development of AMD. It is characterized

by degeneration of cones in the macula. In addition to acquired forms of PR degeneration, there are also inherited retinal diseases (IRD). The most common form of IRD is retinitis pigmentosa (RP), in which more than 80 genes are mutated in non-syndromic forms of RP (Fahim et al., 1993). Non-syndromic forms of RP account for 70 % to 80 % of all RP cases, with a prevalence of 1 in 5,000 worldwide (Verbakel et al., 2018; O'Neal and Luther, 2024). The most common syndromic form of RP is Usher syndrome, which is characterized by hearing loss accompanied by vision loss (Mathur and Yang, 2015). Besides RP, Leber congenital amaurosis (LCA) and Stargardt disease are the most common forms of IRDs (Duncan et al., 2018). IRDs can be genetically very heterogeneous and are inherited as autosomal recessive, autosomal dominant, or X-linked (Ben-Yosef, 2022). In RP, specific gene mutations cause rod photoreceptor dysfunction by affecting critical processes such as the phototransduction pathway (Phelan and Bok, 2000). This results in the death of rods in the peripheral retina in the early stages of the disease, causing night blindness and visual field constriction (Fig. 1.3). Cone OS loss already arises in early stages of RP which reduces their light sensitivity (Lassoued et al., 2021). In the late stages, the density of cones continues to decrease, a process known as secondary loss, leading to loss of central vision (Wright et al., 2010). In addition, RPE, Müller Glia cells and the choroid are affected in later stages, leading to atrophy of RPE cells, activation of Müller Glia cells and choroidal thinning (Lin et al., 2020; Díaz-Lezama et al., 2023; Ayton et al., 2013). While mutations in RP primarily cause rod cell death, cone cell death is independent of these mutations. This is either because the mutated genes are expressed in both rods and cones but are not critical for cone function, or because the mutated gene, such as RHO, is specific to rods and not expressed in cones (Campochiaro and Mir, 2018). Several reasons have been proposed for this secondary loss, including a lack of neurotrophic factors released by rods, or a lack of nutrient supply due to an abnormal cone-RPE interface caused by dying rods (Wright et al., 2010). One of the major goals in vision research is to develop therapies to prevent this secondary loss, counteracting cone degeneration to preserve central high acuity vision and quality of life. To study potential therapeutic approaches retinal degeneration mouse models of RP are well described and have been extensively and successfully used for therapy studies (Nishiguchi et al., 2015). A widely accepted and well-established model system for studying RP is the retinal degeneration 1 mouse (rd1) (Dräger and Hubel, 1978; Zhang et

al., 2024). The *rd1* mutation is a spontaneous mutation and is inherited as an autosomal recessive trait. It is characterized by a nonsense mutation in exon 7 of the phosphodiesterase 6B (*Pde6b*) gene (Bowes et al., 1990). Mice homozygous for this mutation are characterized by a severe and early onset rapid retinal degeneration starting at P8 with no rod photoreceptors present 4 weeks after birth. This is caused by a defect in the beta-subunit of the rod cGMP-PDE, resulting in the accumulation of cGMP in rod photoreceptors. This prevents the closure of cyclic nucleotide-gated (CNG) channels on the rod outer segment plasma membrane, thereby impairing the function of the phototransduction cascade and ultimately leading to rod cell death (Farber and Lolley, 1974; Li et al., 2023). This mutation is also associated with one of the earliest onset and most aggressive forms of human RP, accounting for ~5 % of all cases (Cheng et al., 2016; Pang et al., 2011). The rd10 mouse model has the same genetic mutation, however, it harbors a spontaneous missense mutation in exon 13 of the *Pde6b* gene and is characterized by a later onset of retinal degeneration (Chang et al., 2007).

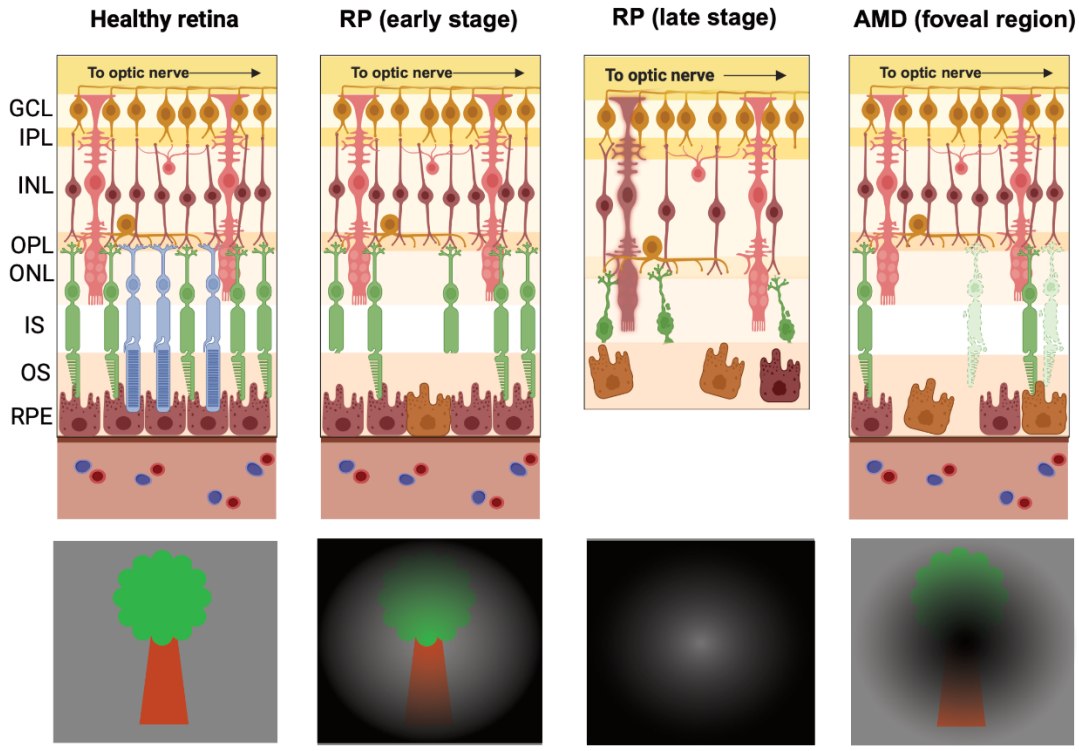

Fig. 1.3 Photoreceptor-related retinal disorders. Early stage RP results in loss of peripheral vision due to rod cell death. Cone OS loss occurs in earlier stages, while cone density loss, also known as secondary loss, occurs in later stages, leading to loss of central vision. In later stages, RPE atrophy, choroidal thinning, and Müller glial cell

activation occur. In AMD, progressive cone loss in the later stages of the disease leads to central vision loss due to cone degeneration in the foveal region, the central part of the macula. (Adapted from “Structure of the Retina” by BioRender.com (2024). Retrieved from https://app.biorender.com/biorender-templates.apos)

1.4 Gene therapy and gene-independent therapeutic approaches

When a specific gene is known to be the triggering factor for the disease, gene therapy approaches are a promising intervention. One of the most prominent gene therapies, that was approved by the U.S. Food and Drug Administration, is Voritigene Neparvovec (Luxturna®) (U.S. Food and Drug Administration, 2017). This drug was successfully used to treat patients with a biallelic mutation in the *RPE65* gene, which causes a severe form of LCA. The delivery of the functional gene copy of *RPE65* to retinal cells using an adeno-associated virus (AAV) as a gene delivery tool resulted in improved visual performance in treated patients (Russell et al., 2017). However, highly complex IRDs with many known causative genes, such as RP, and acquired retinal degenerative diseases, such as AMD, require the consideration of gene-independent therapies (Martin-Fumadó et al., 2022; Zuzic et al., 2022). In this context, antioxidants, monoclonal antibodies and neuroprotective agents such as injections of neurotrophic factors have also proven valuable in counteracting retinal degeneration (Evans and Lawrenson, 2017; Stanca et al., 2019; Pardue and Allen, 2018). Other approaches include optogenetic tools, stem cell-based therapies, or microRNAs (miRNA) (Sahel et al., 2021; Busskamp et al., 2010; Parnami and Bhattacharyya, 2023; Karali et al., 2020; Voisin et al., 2023). miRNAs are critical regulators of gene expression for retinal homeostasis and function and have been implicated in retinal disease pathogenesis (Chu-Tan and Natoli, 2020). Recent *in vivo* and *in vitro* studies highlighted the potential of miRNA-based therapies to counteract retinal degeneration that is independent from the disease-causing genetic mutation (Chu-Tan et al., 2018; Fernando et al., 2020; Wohl et al., 2017). Mouse models are a suitable model system for analyzing the therapeutic effects of miRNAs, as studies comparing mouse and human miRNA transcriptomes (miRNomes) have shown that approximately one-third of the retinal miRNAs expressed in humans are also expressed in mouse retinas (Karali et al., 2010; Pawlick et al., 2020).

1.5 Regulatory functions of miRNAs in photoreceptors

miRNAs are small, non-coding RNAs that serve as important regulators of gene expression and typically have an average size of 22 nucleotides (nt) (Ghildiyal and Zamore, 2009; Ha and Kim, 2014). They were first identified in the nematode *Caenorhabditis elegans* in 1993 (Lee et al., 1993). The biogenesis of miRNAs involves several steps (Fig. 1.4). miRNAs can be encoded by either intronic or exonic regions of genes. More than 80 % of miRNA genes are located in intronic regions of protein-coding genes (Kim and Kim, 2007). Transcription of miRNAs from exonic regions is carried out by RNA polymerases II/III, resulting in the production of primary miRNAs (pri-miRNA) (Lee et al., 2004; Borchert et al., 2006; Pawlick et al., 2020). The pri-miRNAs form stem-loop structures (hairpin) by self-annealing of complementary sequences. The pri-miRNA is then cut 11 base pairs (bp) from the stem-loop by the Drosha ribonuclease and the double-stranded RNA binding domain partner protein DiGeorge critical region 8 (DGCR8), also known as the miRNA processing complex. This action produces the precursor miRNA (pre-miRNA). The pre-miRNA sequence is 70 nt long with a 5' phosphate and a 2-nt overhang at the 3' end (Lee et al., 2002; Ha and Kim, 2014). For further maturation, the pre-miRNA is exported to the cytoplasm via the exportin-5 (XPO5)/RanGTP complex (Yi et al., 2003; Lund et al., 2004). The *trans*-activation response RNA-binding protein (TRBP) binds to the pre-miRNA in combination with the Dicer endoribonuclease and adds a 5' phosphate and a new 2-nt 3' overhang by trimming the pre-miRNA approximately 22-nt from the cleavage site of the miRNA processing complex. This creates the miRNA duplex (Lee et al., 2003). In the final step, the Argonaute (AGO) protein, a component of the RNA-induced silencing complex (RISC), removes the other strand from the miRNA duplex, resulting in a single-stranded miRNA molecule that remains bound to the AGO protein. The miRNA is now able to bind to the 3' untranslated region (3' UTR) of its messenger RNA (mRNA) target in a partially complementary manner via the miRNA seed sequences (Helwak et al., 2013). The AGO proteins are important for the localization of miRNAs to their mRNA targets, which ensures the correct function of miRNAs (Bartel, 2009). miRNAs located in intronic regions of genes are transcribed by RNA polymerases II, which recognize the promoter region of their encoding genes. The miRNA sequences are incorporated into the intronic regions of precursor mRNA (pre-mRNA) transcripts. After

transcription, the spliceosome removes the introns from the pre-mRNA, including the sequences containing the miRNAs, which are then further processed into mature miRNAs (Lin et al., 2006; Westholm and Lai, 2011). miRNAs primarily function as translation repressors or induce the deadenylation of mRNAs. However, they can also act as translation enhancers (Vasudevan et al., 2007). miRNA mimics facilitate the study of gene function and have been used to analyze the therapeutic effects of specific miRNAs (Chu-Tan et al., 2018; Wang, 2011). Short-hairpin RNAs (shRNA) serve as important controls for RNA interference (RNAi) studies, including non-targeting controls, to validate the specificity of RNAi effects (Moore et al., 2010). One miRNA can have thousands of *in silico*-annotated target mRNAs due to similarities in the 3' UTR of distinct mRNAs (Lewis et al., 2005). Different variants of a single miRNA, known as isomiRs, can also lead to altered target specificity due to nucleotide substitutions in the miRNA seed region (Karali et al., 2016). miRNAs perform important regulatory functions in numerous biological systems, thereby promoting overall system function (Ebert and Sharp, 2012). Their dysregulation often leads to pathological conditions, including developmental disorders, neurodegenerative diseases, and cancer (Ha, 2011; Dong et al., 2015; Chu-Tan et al., 2018; Krol et al., 2010b). In the eye, miRNAs play an important role in maintaining retinal homeostasis, function, and development (Sundermeier and Palczewski, 2016; Lumayag et al., 2013; Zhu et al., 2011). It has been shown that light-induced retinal damage results in the upregulation of miRNAs, which are known to influence the immune response, one of the key triggers of retinal degeneration in AMD (Saxena et al., 2015). The importance of correct miRNA function in photoreceptors was demonstrated by a conditional knockout of the DGCR8 protein in cones, which led to the complete loss of cone OS and therefore visual function (Busskamp et al., 2014a). Besides knockout studies, overexpression studies have proven valuable to analyze the importance of miRNA functions in biological systems (Krützfeldt et al., 2006). *In vivo*, the overexpression has been successfully demonstrated by introducing double-stranded miRNAs in the form of pre-miRNA sequences via AAV delivery systems into mouse tissues, allowing long-term expression of transgenes to dissect important biological functions (Poy et al., 2004; Rabinowitz and Samulski, 1998; Auricchio et al., 2001b). AAV vectors have also proven to be the dominant gene delivery system for ocular therapies, demonstrating improved safety, specificity, and efficacy (Rodrigues et al., 2018). In this context, the subretinal route is advantageous due

to the minimized immunogenicity of the AAV particles (Anand et al., 2002). Effective gene delivery also requires the use of specific AAV serotypes that are organ and tissue specific and play a key role in determining AAV tropism (Issa et al., 2023). The AAV2.NN serotype has demonstrated increased tropism of photoreceptor cells (Pavlou et al., 2021).

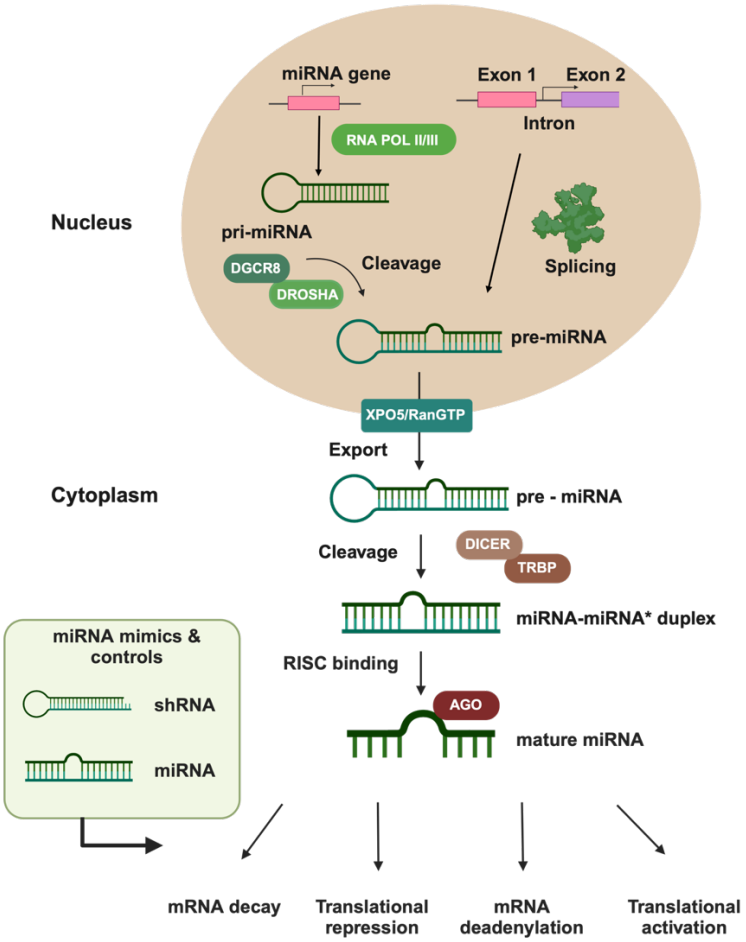

Fig. 1.4 miRNA Biogenesis. miRNAs are expressed from exonic or intronic regions of the genome. Pri-miRNAs are transcribed by RNA polymerases II/III when encoded by exonic DNA sequences. The Drosha ribonuclease, together with the DGCR8 protein (parts of the miRNA processing complex) cleaves pri-miRNAs to form pre-miRNAs. These pre-miRNAs are then exported to the cytoplasm by the XPO5/RanGTP complex. In the cytoplasm, the Dicer/TRBP nuclease complex processes pre-miRNA to produce double-stranded miRNA duplexes. The AGO protein, as part of the RISC, binds to the miRNA duplex and removes one of the strands, forming a mature miRNA-loaded RISC complex. The AGO/miRNA complex can then target and regulate mRNAs. miRNAs transcribed from intronic regions undergo splicing during processing. miRNA mimics are used in therapeutic strategies, while shRNA can serve as controls in RNAi studies to validate specificity. (Modified from (Pawlick et al., 2020). Original figure is licensed under the Creative Commons Attribution license, https://creativecommons.org/licenses/by/4.0/).

1.5.1 miR-182/96/183 cluster in photoreceptors

miRNA genes can be expressed as clusters, with two or more miRNAs simultaneously transcribed into a single primary transcript encoding multiple miRNAs (Ware et al., 2024; O'Brien et al., 2018). In this case, miRNA genes are arranged in close proximity on the chromosome, allowing transcription as a single pri-miRNA transcript (Altuvia et al., 2005; Zhang et al., 2009). In humans, approximately 40 % of miRNA genes are expressed as clusters (Altuvia et al., 2005). One of the most important clusters in the retina is the miR-182/96/183 cluster, where it regulates important functions in PRs (Pawlick et al., 2020). The three different miRNAs have high sequence homology with similar mRNA targets, but they also have differences in their seed sequences, which ultimately lead to different mRNA targets (Dambal et al., 2015). The high seed sequence homologies between cluster members may result in mutual compensation of regulatory functions. This was demonstrated by a targeted deletion of miR-182, which did not lead to phenotypic changes, suggesting that the other two members likely have compensatory effects (Jin et al., 2009). Based on miRTarBase entries for the miR-182/183 cluster the miRNAs share 25 validated common targets as well as 86 common predicted biological targets based on TargetScan (release 7.2) (Chou et al., 2018; Agarwal et al., 2015). Fig. 1.5 provides Venn diagrams to demonstrate the cluster interactions. The cluster has important functions in synaptogenesis, synaptic transmission, and photoreceptor function, and its dysregulation has been associated with syndromic retinal degeneration (Lumayag et al., 2013; Pawlick et al., 2020). miR-182 and miR-183 were shown to specifically prevent OS loss, highlighting their importance for cone OS maintenance and function *in vivo* (Busskamp et al., 2014a). This observation makes miR-182 and miR-183 promising candidates for therapeutic strategies aimed at preventing cone OS degeneration. The cluster member, miR-96 is essential for proper photoreceptor development but shows low levels of expression in retinal cone cells (Busskamp et al., 2014a; Xiang et al., 2022). More importantly, miR-96 plays a critical role in inner ear hair cell function. Mutations are associated with progressive hearing loss in both mouse models and humans (Gwilliam et al., 2024). During early phases of retinal development, mature cluster expression is low, but increases after birth with peak expression in the adult retina (Xu et al., 2007). For postnatal development of the retina, a coordinating function between a long non-coding

RNA retinal non-coding RNA 4 (lncRNA Rncr4) and the miRNA cluster was shown to be crucial. However, forced expression of the cluster had detrimental effects on retinal layer morphology, highlighting the importance of timed cluster expression during retinal development (Krol et al., 2015). It also regulates *PAX6* expression, a well-studied gene for neuroectoderm specification, which suggested its crucial role in the morphogenesis of the retinal tissue (Peskova et al., 2020; van Heyningen and Williamson, 2002; Kaspi et al., 2013). The cluster is also light-regulated and has a rapid turnover in mouse retinas (Krol et al., 2010a). This light-regulated expression is associated with the anti-apoptotic effect of the cluster by targeting *caspase-2* (*Casp2*), a gene involved in the apoptotic pathway. This was demonstrated by disrupting the three miRNAs using a sponge transgenic mouse model, which resulted in increased retinal degeneration following light exposure (Zhu et al., 2011).

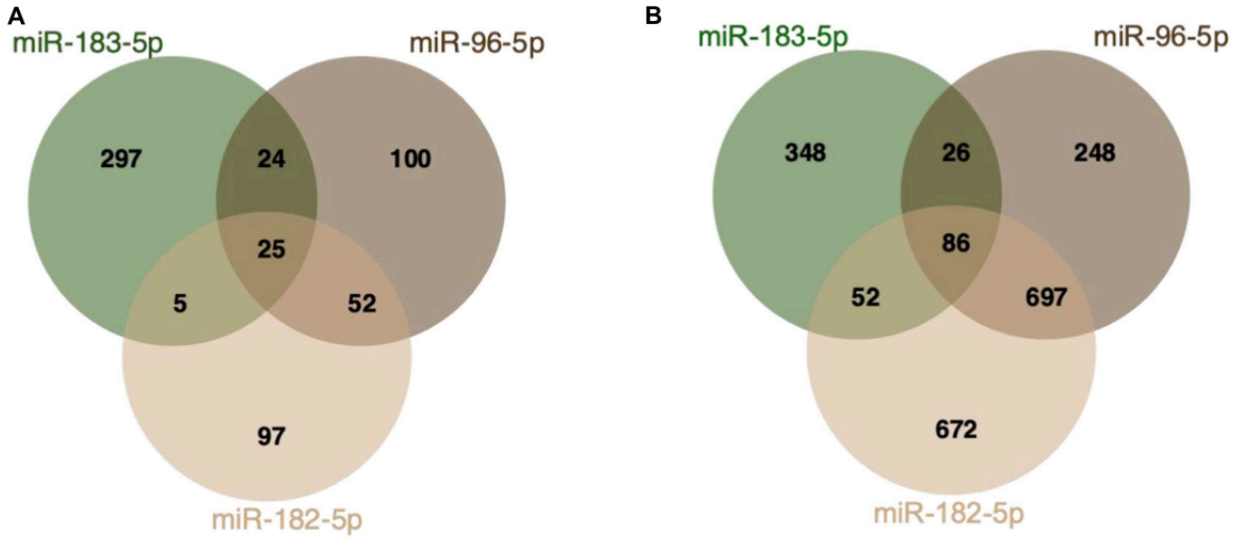

Fig. 1.5 Validated and predicted miR-182/96/183 cluster targets. (A) Venn Diagram showing miRTarBase entries of validated cluster targets, with 25 common targets (Chou et al., 2018). **(B)** Venn Diagram illustrating predicted targets derived from TargetScan (Release 7.2)**.** The analysis is derived from the presence of target sites that align with the seed region of the individual miRNAs. The three miRNAs have 86 predicted common biological targets (Agarwal et al., 2015) (Reproduced from (Pawlick et al., 2020). Original figure is licensed under the Creative Commons Attribution license, https://creativecommons.org/licenses/by/4.0/).

1.5.2 Neuron-specific miR-124

miR-124 has an important role in retinal development and function exhibiting high expression levels also in the brain (Sun et al., 2015; Wang et al., 2020; Lagos-Quintana et al., 2002). Dysregulation of miR-124 has been associated with pathological conditions and developmental defects in the retina (Pawlick et al., 2020; Sanuki et al., 2011; Karali et al., 2016). Partial loss of miR-124 during development leads to reduced opsin expression and cone death and altered physiological expression of miR-124 is associated with progressive retinal damage, inflammation, and cell death in AMD patients and mice with photo-oxidative induced retinal degeneration (Chu-Tan et al., 2018; Chu-Tan et al., 2021). Intravitreal delivery of miR-124 has been shown to reduce chemokine levels in degenerating retinas, diminish photoreceptor death and improve overall retinal function, highlighting its anti-inflammatory properties (Newman et al., 2012; Chu-Tan et al., 2018). In this context it is important to note, that the innate immune response plays an important role in many retinal degenerative diseases, such as AMD and diabetic retinopathy (DR). Ocular inflammation is also a contributing factor in the progression of retinal degeneration in rd1 mouse models and RP patients (Mohan et al., 2022). Binding of miR-124 to the 3' UTR of the mRNA encoding for the monocyte chemotactic protein 1 (MCP-1), one of its major targets, has been shown to be one of the mechanisms by which the anti-inflammatory effects are mediated, thereby reducing MCP-1 expression and inflammation. (Dong et al., 2015). The MCP-1 protein can be detected in both tears and vitreous fluid of DR patients (Wakabayashi et al., 2011; Chernykh et al., 2015). In embryonic stem cells and human fibroblasts miR-124 can also promote neuronal differentiation (Krichevsky et al., 2006; Yoo et al., 2011). In conclusion, the anti-inflammatory properties of miR-124 make it a promising therapeutic tool for counteracting retinal degeneration.

1.6 Human stem-cell derived retinal organoids

IRDs have been extensively studied in mouse models, which has contributed to a better understanding of the underlying molecular pathological mechanisms and led to the development of novel therapies (Moshiri, 2021). However, mice have limitations due to their different anatomy from the human eye as described in Section 1.2, making it difficult

to study cone-focused diseases such as AMD (Slijkerman et al., 2015). Growing ethical concerns and the 3Rs principles (Reduction, Replace and Refine) have also been one of the driving forces behind the development of alternative research models (Russell and Burch, 1992; Kiani et al., 2022). Human stem-cell derived retinal organoids (hRO) have emerged as valuable *in vitro* model systems that closely mimic the human retina. A major advance in this field is the agarose microwell array seeding and scraping (AMASS) protocol, which allows the growth of photosensitive hROs with functional synapses in large quantities (Cowan et al., 2020). Fig. 1.6 outlines the protocol. These hROs resemble the transcriptome of the adult peripheral retina, including the expression of disease-associated genes, making them suitable for disease modeling that could potentially replace animal models in the future. Despite this progress, major challenges remain. A main drawback is the formation of the necrotic core in hROs, which results in the loss of inner retinal cells such as RGCs before the photoreceptors are fully mature, limiting functional analysis. It takes more than 30 weeks for cone OS to develop and become photosensitive, and rods mature even later, around week 38. By this time, the number of RGCs is already severely reduced, making it difficult to study photoreceptor functionality at a stage when the inner retina is still intact (Cowan et al., 2020). In addition, hROs lack a vasculature and immune cells. Regarding miRNA studies, the miR-182/96/183 cluster was also shown to take over an important role as a regulator of *PAX6* in hROs as a critical factor for retinal tissue development, which was also demonstrated *in vivo* (Peskova et al., 2020; van Heyningen and Williamson, 2002). Furthermore, a light-regulated activity of miR-182/96/183 could be demonstrated in hROs (Celiker et al., 2023). This underscores the comparability of hROs and the retina, making it a good *in vitro* model system to study miRNA function. In mouse embryonic stem cell (mESC)-derived retinal organoids, the application of miR-182 and miR-183 has already been shown to support OS growth and light responsiveness, highlighting their potential to support photoreceptor maturation (Busskamp et al., 2014a).

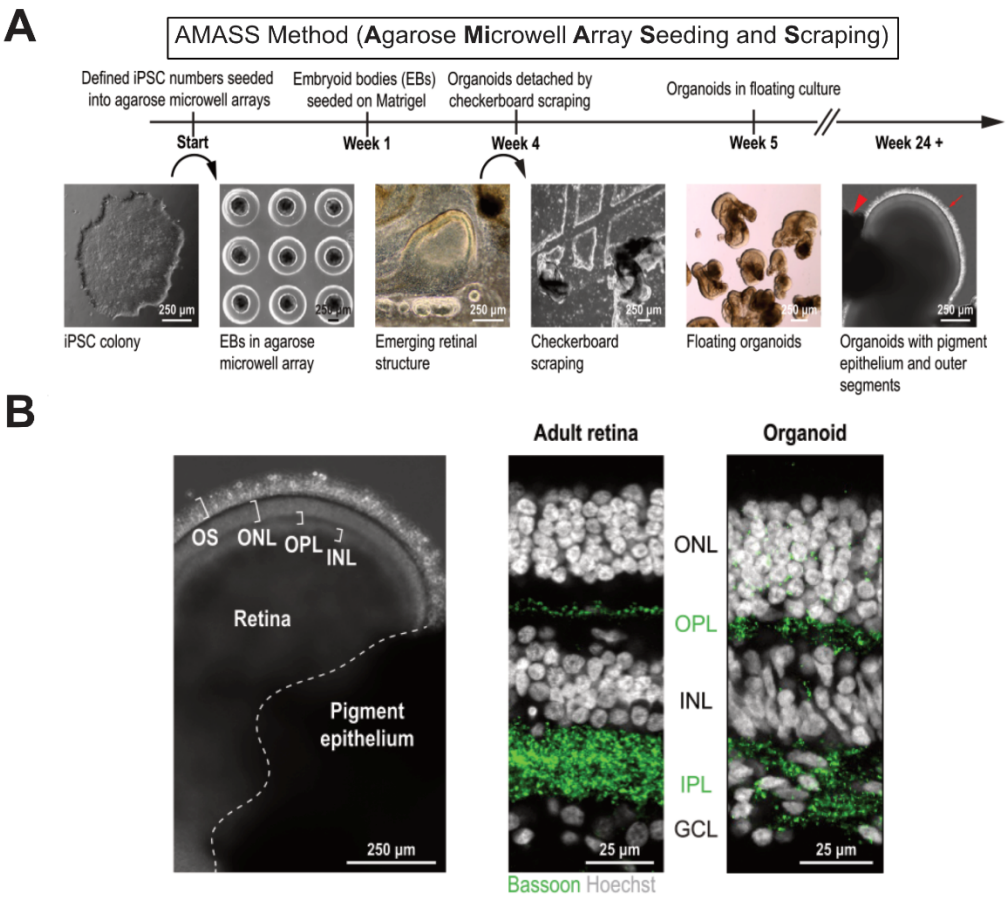

Fig. 1.6 AMASS protocol timeline and hRO morphology. (A) Overview of the AMASS protocol for growing hROs, including the key step of transitioning from a 2D to a 3D culture. **(B)** Layered morphology of an hRO resembling the layered morphology of the adult retina. Bassoon staining (synaptic marker) shows the synapses formed in the plexiform layers (OPL, IPL) and Hoechst staining (nuclear marker) visualizes the different layers. (Modified from (Cowan et al., 2020), Original figure is licensed under the Creative Commons Attribution license, https://creativecommons.org/licenses/by/4.0/).

1.7 Aims

The first aim of my thesis was to analyze the neuroprotective effects of miR-182, miR-183 and miR-124 on cones in retinal degenerative mouse models of RP. The goal was to investigate the potential of these miRNAs as a gene-independent therapeutic approach to counteract retinal degeneration, especially in IRDs with complex genetic backgrounds such as RP, which are difficult to treat with traditional gene therapies. This research should also be conducted with a view to potential broader applicability, including other retinal degenerative diseases, such as AMD, that are not exclusively genetic in origin. By

achieving this goal, the thesis will therefore expand the current knowledge of neuronal miRNAs and provide valuable insights into their effects on degenerating cone photoreceptors *in vivo.* The second aim was to apply miR-183 to stem cell-derived hROs *in vitro* to enhance cone photoreceptor maturation. Achieving this goal will expand the understanding of miR-183 and its role in enhancing cone photoreceptor maturation in hROs and provide a basis for accelerating cone photoreceptor development using miRNAs. This could help address one of the major bottlenecks in hROs by enabling cone photoreceptor functionality at an earlier time point in hRO development.

2 Material and Methods

2.1 Material

Tab. 2.1: Equipment

Device	Producer
Animals	
1 ml syringe without cannula	Becton Dickinson
30-gauge (G) needle	Becton Dickinson
30 G, Small Hub RN Needle, 2 in, point style	Hamilton
BD Microlance™ 30 G needles	Becton Dickinson
5 µl Microliter Syringe 75 RN, with small removable needle	Hamilton
Digital just for Mouse Stereotaxic Instrument	Stoelting
Cold-light source for surgery KL1500 electronic	Schott
(fluorescent live imaging retinal explants)	Leica Microsystems
Manual Micromanipulator (right-handed)	World Precision Instruments
M10 magnet stand	World Precision Instruments
Rodent Warmer Control Box X1 eGFP/cable	Stoelting
Stereomicroscope STEM SV8 (surgery)	Zeiss
Sterican® 25 G single-use needles	B. Braun
Sterican® 27 G single-use needles	B. Braun
Behavioral studies	
Light/dark Box	Self-made
OptoDrum Standard	Striatech GmbH
Scantainer Classic	Scanbur A/S
General equipment	
-150 Freezer	PHC Corporation
-80 Freezer CryoCube	Eppendorf
Analytic balance	VWR
Centrifuges	Eppendorf
Fridge	Liebherr
Cell culture	
4D-Nucleofector Core Unit and X Unit	Lonza Bioscience
Bead Bath	Thermo Fisher Scientific
BZ-X810 fluorescent microscope	Keyence
CO2-Incubator	PHC Corporation
Countess™ II cell counter	Invitrogen
EVOS FL Core microscope	Invitrogen
Revolve Echo	Echo
Sterile hood	PHC Corporation
ThawSTAR™ CFT2 Automated Thawing System	STEMCELL Technologies
Cloning	
Advanced digital shaker Orbit 3500 Digital	VWR
E-Gel™ Power Snap Electrophoresis System	Thermo Fisher Scientific
Heat block	Eppendorf
Nanodrop one Spectrophotometer	Thermo Fisher Scientific

ProFlex PCR System	Thermo Fisher Scientific
QIAcube Connect	Qiagen
QIAvac Vacuum system	Qiagen
Immunohistochemistry	
MNT Cryostat	SLEE medical GmbH
Microwave	Carl Roth GmbH + Co. KG
StainTray™ M918	VWR
Visitron VisiScope Spinning Disk Microscope	Carl Zeiss
Staining cuvette	Brand GmbH + Co. KG
Nucleofection	
Lonza 4D Nucleofector	Lonza Group
RT-qPCR	
QuantStudio™ 3 Real Time PCR	Thermo Fisher Scientific

Tab. 2.2: Consumables

Consumable	Supplier
5PRIME Phase Lock Gel	VWR
0.2 filter	Starlab
6 well plate	Corning/Falcon
12 well plates	Corning
Countess™ cell counting chamber slide	Thermo Fisher
Microcentrifuge tubes	Sarstedt
Falcon tubes	Eppendorf
Flasks	Corning

Tab. 2.3: Cell lines

Cell line		Supplier
hiPSC 01F49i-N-B7		Institute of Molecular and Clinical Ophthalmology Basel (IOB)
iNGN	Inducible expression of Neurogenin 1/2	(Busskamp et al., 2014b) https://eGFP.encodeproject.org; on the basis of The Personal Genome Project iPSC line 1 (PGP1; Lee et al., 2009; available at Coriell GM23338, primary dermal fibroblasts GM23248
OneShot™Stbl3™Chemically Competent E. coli		Thermo Fisher Scientific

Tab. 2.4: Reagents

Substance	Order No.	Supplier
Animals		
Bepanthen® eye and nose ointment	n/a	Bayer AG
Carprosol® 50 mg/ml	n/a	CP-Pharma GmbH
Dexa Gentamicin eye ointment	n/a	Ursapharm
Ketamine 10 %	n/a	Serumwerk Bernburg AG
Xylazine 20 mg/ml	n/a	Serumwerk Bernburg AG
Cell Culture		
Antibiotic-Antimycotic	15240062	Thermo Fisher Scientific
B-27 Supplement (50X), minus vitamin A	12587010	Thermo Fisher Scientific
Dimethyl sulfoxide (DMSO)	D2650-5X5ML	Sigma-Aldrich Merck
Doxycycline hyclate	14021705	Sigma-Aldrich Merck
Dulbecco's Modified Eagle Medium (DMEM) / F12, GlutaMAX™ Supplement	31331-028	Thermo Fisher Scientific
Dulbecco's phosphate-buffered saline without Calcium and Magnesium (DPBS -/-)	14190169	Thermo Fisher Scientific
DMEM with 4.5 g/L Glucose and Pyruvate	10569-010	Thermo Fisher
Gentamycine (10 mg/ml)	15710064	Thermo Fisher Scientific
Gibco™ Fetal bovine serum (FBS), qualified, heat inactivated	10500064	Thermo Fisher Scientific
Ham's F12 Nutrient mix, GlutaMAX™ supplement	31765-027	Thermo Fisher Scientific
Heparin (stock 2 mg/ml in H_2O, final concentration: 2 µg/ml)	H3149-50KU	Sigma-Aldrich Merck
MEM Non-essential Amino Acids (100X) without L-glutamine	M7145-100ML	Sigma-Aldrich Merck
Matrigel hESC-qualified matrix	7643022	Corning Life Sciences B.V.
mFresR	05855	STEMCELL Technologies
Mycoplasma PCR detection kit	11251258	Geyer Th. GmbH
mTeSR™1 complete kit	85850	STEMCELL Technologies
N2 Supplement (100X)	17502048	Thermo Fisher Scientific
Penicillin-Streptomycin (10,000 U/mL)	15140122	Thermo Fisher Scientific
Retinoic acid (≥ 98 % HPLC, powder)	R2625-50MG	Sigmla-Aldrich Merck
ROCK-inhibitor Y27632	14044188	STEMCELL Technologies
Taurine ≥ 99 %	TO625-25G	Sigma-Aldrich Merck
Trypan Blue Solution	16500500	Sigma-Aldrich Merck
TrypLE Express Enzyme (1X), no phenol red	12604013	Thermo Fisher Scientific
UltraPure Agarose	16500500	Thermo Fisher Scientific
Cloning		
Agar-Agar	14038844	Carl Roth GmbH + Co. KG
AgeI-HF	R3552S	New England Biolabs
AhdI	R0584L	New England Biolabs
BsrGI-HF	R3575S	New England Biolabs
Carbenicillin (stock: 50 mg/ml; working concentration: 100 µg/ml)	A1491,0010	ITW Reagents
CloneAmp HiFi PCR Premix	639298	Takara Bio Inc.
CutSmart® Buffer	B6004S	New England Biolabs
DNA Ligation Kit, Mighty Mix	6023	Takara Bio Inc.
E-gel™ 1 Kb Plus DNA Ladder	10488090	Thermo Fisher Scientific
E-Gel™EX Agarose Gels 1 %	G402021	Thermo Fisher Scientific
E-Gel™EX Agarose Gels 2 %	G402022	Thermo Fisher Scientific

HindIII	R0104S	New England Biolabs
MinElute PCR Purification Kit	28706	Qiagen
NheI-HF	R3131S	New England Biolabs
Plasmid Plus Midi Kit	217004	Qiagen
QIAquick Gel Extraction Kit	14035180	Qiagen
QIAprep Spin Miniprep Kit	YP00206030	Qiagen
S.O.C Medium	15544034	Thermo Fisher Scientific
Sodium chloride	S3014-1KG	Sigma-Aldrich Merck
SmaI	R0141S	New England Biolabs
SpeI-HF	R3133S	New England Biolabs
Tryptone/Peptone ex casein	8952.3	Carl Roth GmbH + Co. KG
Yeast extract	14038897	Carl Roth GmbH + Co. KG
Nucleofection		
P3 Primary Cell 4D-Nucleofector X Kit L	V4XP-3024	Lonza Bioscience
Puromycin Dihydrochloride	A1113803	Thermo Fisher Scientific
Trypan Blue solution	14044188	Sigma-Aldrich Merck
RT-qPCR		
5Prime Phase Lock Gel Heavy (2 ml)	733-2478	VWR
hsa-5S-rRNA miRCURY LNA miRNA PCR Assay	YP00203906	Qiagen
Chloroform	288306-100ML	Sigma-Aldrich Merck
High-capacity cDNA Reverse Transcription kit	4368814	Thermo Fisher Scientific
hsa-miRNA-124-3p miRCURY LNA miRNA PCR Assay	G402021 G402022	Qiagen
hsa-miRNA-182-5p miRCURY LNA miRNA PCR Assay	339346	Qiagen
hsa-miRNA-183-5p miRCURY LNA miRNA PCR Assay	339340	Qiagen
MinElute Reaction Cleanup kit	YP00206026	Qiagen
miRCURY LNA SYBR Green PCR kit	339306	Qiagen
miRCURY LNA RT kit	10488090	Qiagen
*Power*SYBR™Green Cells-to-Ct™Kit	4402954	Thermo Fisher Scientific
PowerUp SYBR Green PCR Master Mix	4367659	Thermo Fisher Scientific
QIAzol Lysis Reagent	79306	Qiagen
MicroAmp® EnduraPlate™ Optical 96-Well Clear Reaction Plate with Barcode	4483354	Thermo Fisher Scientific
RNAse free DNAse set	14035254	Qiagen
RNEasy MinElute Cleanup Kit	28204	Qiagen
RNEasy Mini Kit	74106	Qiagen
TE buffer pH 8.0 sterile by filtration	BBA-D0123-450	BIOZOL Diagnostica Vertrieb GmbH
Immunohistochemistry		
4 % Paraformaldehyde in PBS	J19943-K2	Thermo Fisher Scientific
Bovine Albumin Fraction V (7.5 % solution)	15260037	Thermo Fisher Scientific
Normal donkey serum (NDS)	S30-100ML	Sigma-Aldrich Merck
PAP-Pen	Z672548-1EA	Sigma-Aldrich Merck
ProLong Gold Antifade Mountant	27106	Thermo Fisher Scientific
Sucrose, BioXtra >99.5 % (GC)	S7903-1KG	Carl Roth GmbH + Co. KG
Super Frost Plus slides	7672831	Geyer Th. GmbH
Tissue-Tek® Cryomold® (15 mm x 15 mm x 5 mm)	4565	Sakura Finetek GmbH
Tissue-Tek® O.C.T. ™ Compound	4583	Sakura Finetek GmbH
Tri-sodium citrate Dihydrate	106466	Merck Millipore

Triton X-100	T8787-50ML	Sigma-Aldrich Merck
Tween-20™	J20605.AP	Thermo Fisher Scientific
Electrophysiology		
60MEA200/30iR-Ti-gr	890103	Multi-Channel Systems
Calcium chloride ($CaCl_2$)	CN93.1	Carl Roth GmbH + Co. KG
D-Glucose	1083371000	Merck
Laminin from murine Engelbreth-Holm-Swarm sarcoma (working concentration: 0.05 mg/ml)	14044788	Sigma-Aldrich Merck
Magnesium chloride 6-hydrate ($MgCl_2.6H_2O$)	131396.1210	ITW Reagents
Poly-D-Lysine (working conc: 0.1 mg/ml; stock solution: 1.0 mg/ml, 20 ml)	A-003-E	Sigma-Aldrich Merck
Potassium chloride (KCl)	T138.1	Carl Roth GmbH + Co. KG
Sodium hydrogen carbonate ($NaHCO_3$)	1063291000	Merck Millipore
Sodium Phosphate Monohydrate ($NaH_2PO_4.H_2O$)	71504-250G-M	

Tab. 2.5: Supplement and buffer compositions

Supplement / Buffer	
Blocking solution	0.3 % Triton – 100X + 2 % Bovine Serum Albumine (BSA) + 5 % Normal donkey serum (NDS) in PBS
CEPT cocktail	1 x CET Stock 1000 x + 1 x Polyamin supplement 1000x in culture medium
Permeabilization buffer	1 % Triton-100X in PBS
Sodium citrate buffer	0.3 % Tri sodium citrate (dihydrate) + 0.05 % Tween-20; pH = 0.6

Tab. 2.6: Plasmids

Construct name	**Supplier**
Cloning backbones for Piggy Bac vectors	
MISSION pLKO. 1-Puro Non target shRNA control	Sigma-Aldrich
pMA-RQ-sh-ctrl-Puro	Thermo Fisher Scientific
pPB-eGFP-XhoI-V5-rep-Puro	Busskamp Lab
pSMPUW-miRNA-124-GFP-Puro	Addgene
pSMPUW-miRNA-182-GFP-Puro	Addgene
pSMPUW-miRNA-183-GFP-Puro	Addgene
pSMPUW-miRNA -GFP-Puro	Cell Biolabs, Inc.
Cloning backbone for AAV vectors	
AAV-mCAR-Halo57mutant-GFP	Busskamp Lab
Nucleofection	
pPB-TetON-miR-182-eGFP-Puro	
pPB-TetON-miR-182-eGFP-Puro	
pPB-TetON-miR-124-eGFP-Puro	
pPB-TetON-shNTC-eGFP-Puro	
pPB-mCAR-miRNA-183-eGFP-Puro	
pCMV-Transposase	System Biosciences
AAV vectors for subretinal injections/hROs	
pAAV-mCAR-miR-182-eGFP-Puro	
pAAV-mCAR-miR-183-eGFP-Puro	
pAAV-mCAR-miR-124-eGFP-Puro	

Tab. 2.7: Antibodies and dyes

Antigen	Host	Dilution	Order #	Supplier
Primary Antibodies				
Anti-Arrestin C Antibody	rabbit	1:10.000	AB15282	Chemicon
Anti-Arrestin 3	Rabbit	1:100	NBP2-41249	Novus Biologicals
Anti-Green fluorescent Protein (GFP) Polyclonal	chicken	1:200	A10262	ThermoFisher Scientific
Anti-Opsin red/green	rabbit	1:200	Ab5407	Abcam
Secondary Antibodies				
Anti-chicken-Alexa™ Fluor 488	donkey	1:500	703-545-155	Jackson ImmunoResearch
Anti-Goat-Alexa™ Fluor 568	donkey	1:500	A11057	Thermo Fisher Scientific
Hoechst 33342, Trihydrochlorid, Trihydrat – 10 mg/ml		1:1000	H3570	Thermo Fisher Scientific
Anti-Mouse-Alexa™ Fluor 647	donkey	1:500	A-31571	Thermo Fisher Scientific
Anti-Rabbit-Alexa™ Fluor 568	donkey	1:500	A10042	Thermo Fisher Scientific

Tab. 2.8: Primers

Primer	Sequence
Cloning PB constructs	
FWD-miR-GFP-BsrGI	ACTAGTACTAGTGGTAATTTTGCATTTGTAATT
REV- miR-GFP-SpeI	TGTACACTTGTACAGCTCGTCCATGCC
Gibson Assembly AAVs	
FWD-miR-182/183/124	AGGAGATCCGCCACCGGTAATTTTGCATTTGTAATT
REV-miRNA-182/183/124	GATTGGATCCAAGCTTTCATTACTACGTAGAATCGA
FWD-AAV-mCAR	TCGCCCTTAAGCTAGCGGTTCTTCCCATTTTG
REV-AAV-mCAR	AAATGCAAAATTACCGGTGGCGGATCTCCTCCAGCT
Genotyping	
REV-miRNA-inserts	GTCAGCTTGCCGTAGGTGGCA
FWD-eGFP	CACAGCTCCTGGGCAACGTGC
REV-mCAR	GTATCATTATTGCCCTGAAAG
FWD-intron (AAV)	TGGGAGGCCAGCTTAGCAACC
FWD-Tre3G	ACGGCCACTAGTCTTTCGTCT
REV-miR-124-insert (AAV)	TCGGTCGGTCGCTCCTTCCTT
REV-miR-182	CTGGGGACACACTGGACGAGG
RT-qPCR	
ACTB forward	CCTCGCCTTTGCCGATCC
ACTB reverse	CGCGGCGATATCATCATCC
Actb forward	GATTACTGCTCTGGCTCCTAG
Actb reverse	GACTCATCGTACTCCTGCTTG
eGFP forward	CAACAGCCACAACGTCTATATCATG
eGFP reverse	ATGTTGTGGCGGATCTTGAAG

Tab. 2.9: Software

Software	Producer	Purpose
Benchling	Benchling	*In silico* design primers, vector maps and alignment of genetic sequences
BioRender	BioRender	Designing figures/Illustrations
BZ-X800 Viewer	Keyence	Processing of images acquired with Keyence BZ-800 microscope
DeepL	DeepL GmbH	Accurate translation
Echo Revolve	Echo	Live fluorescent imaging
Fiji/Image J	(Schindelin et al., 2012)	Image analysis
Prism 9	GraphPad	Statistical data analysis/graphs
Mendeley 2024	Elsevier	Reference management
Microsoft Excel	Microsoft Corporation	qPCR data analysis
Microsoft Word	Microsoft Corporation	Thesis writing
OptoDrum software V. 1.5.0 /	Striatech	Automated analysis of visual acuity in mice
QuantStudio ™ Design & Analysis Software v1.5.1	Thermo Fisher Scientific	Operation of the QuantStudio 3 Real time PCR machine to run plates & experiments
VisiView® Software	Visitron Systems GmbH	Confocal microscope software

2.2 Methods

2.2.1 Common methods

2.2.1.1 Cloning of PB inducible miRNA vectors

Restriction enzyme (RE) cloning was used to generate the miRNA overexpression vectors. The miRNA overexpression cassette consisting of the human (hsa) pre-miRNA sequences of miR-182, miR-183 and miR-124 located within the intronic region of human beta-globin (hBG) and the enhanced green fluorescent protein (eGFP) reporter gene were subcloned from the lentiviral (LV) source plasmids into PiggyBac (PB) vector backbones. The PB transposon system allows stable gene integration into TTAA sites within the host cell chromosome upon nucleofection (Woodward and Wilson, 2015). The PB vector backbones carry the genetic information of the inducible Tetracycline ON (TetON) promoter and a Puromycin (Puro) resistance gene driven by the ubiquitously expressed EF1 alpha (α) promoter. RE primers for DNA amplification of miRNA expression cassettes contained restriction sites for SpeI or BsrGI endonucleases at the 5' end followed by the target sequence at the 3' end. All primers were purchased from Eurofins Genomics (Tab. 2.8). Polymerase chain reaction (PCR) amplification of the DNA inserts was performed

using CloneAmp™ High-Fidelity PCR Premix (Takara Bio Inc.) Reaction mixes were prepared according to the manufacturer's instructions (Tab. 2.10) and then loaded into a ProFlex PCR System for the thermal cycling (Tab. 2.11).

Tab. 2.10: CloneAmp™ PCR reaction mix

Reagent	Volume	Final Concentration
CloneAmp™ HiFi PCR Premix	12.5 µl	1X
Forward Primer	5 – 7.5 pmol	0.2 – 0.3
Reverse Primer	5 – 7.5 pmol	0.2 – 0.3
Template	< 100 ng	
Sterilized distilled water	Up to 25 µl	
Total volume per reaction	25 µl	

Tab. 2.11: PCR cycling conditions

Cycle step	Temperature	Time	Cycles
Initial Denaturation	98°C	10 sec	30
Annealing	55°C – 62°C	15 sec	
Extension	72°C	5 sec/kb	
	4°C	Hold	1

PCR reaction samples were transferred to a precast E-Gel EX 1 %. DNA bands (miRNA overexpression cassettes: ~2 kb; backbone: ~8 kb) were excised from the gel and purified using the QIAquick Gel Extraction Kit. The PCR inserts were digested with SpeI and BsrGI REs, while the PB backbone was linearized with NheI and BsrGI. For a 10 µl reaction mixture, 1 µg of DNA was combined with 1 µl of each RE and 2 µl of 10X CutSmart® Buffer. The mixture was incubated at 37°C for 1-2 hours (h) to generate compatible ends for subsequent ligation of the inserts and backbone. After digestion, the backbones were loaded onto a precast E-Gel EX 1 % gel prior to ligation, and DNA bands were extracted and purified. PCR products were purified immediately after digestion using the PCR Purification Kit. For subcloning the miRNA inserts into the final PB backbone, 100 ng of the digested vector backbone was mixed with the PCR inserts at a 1:3 molar ratio in a total volume of 10 µl. The mixture was combined with the DNA Ligation Mix from the DNA Ligation Kit (Takara Bio Inc.) and incubated for 30 minutes (min) at 16°C. The short hairpin non-targeting control (shNTC) sequence (MISSION control library, Sigma-Aldrich Merck, Catalog No. SHC016-1EA) was generated as a control vector and selected as a control

for the miRNA studies. The shNTC sequence was integrated into the hBG intronic region, followed by the genetic sequence of the eGFP reporter gene, similar to the expression strategy for pre-miRNA sequences by an external company (Thermo Fisher), and integrated into a default vector. RE sites were introduced to facilitate the placement of the shNTC overexpression cassette followed by the eGFP reporter gene sequence into a LV intermediate vector. This LV later served as a template for subcloning the sequence into the PB backbone. The LV backbone and the default vector were digested with the REs, AclI and EcoRI under the same conditions described earlier in this section. The digested fragments were run on a precast E-Gel EX 1 % gel, and the appropriate DNA bands were isolated and purified. The purified fragments were then ligated to form the LV intermediate vector. Subsequently, the shNTC overexpression cassette and the eGFP reporter gene were subcloned into the PB vector backbone via RE cloning, following the same procedure used for the miRNA overexpression cassettes and eGFP.

Bacterial transformation of One Shot™ Stbl3™ chemically competent *Escherichia coli* (*E. coli*) was performed according to the manufacturer's protocol. The bacterial suspension was then inoculated onto prewarmed Lysogeny Broth (LB) - Carbenicillin (Carb) agar plates and incubated overnight at 37°C. For each vector, eight bacterial colonies were transferred with a pipette tip to 5 ml of LB medium supplemented with Carb and incubated overnight at 37°C in a shaking incubator. DNA was isolated using the QIAprep Spin Miniprep Kit and the QIAcube pipetting robot. A concentration of 80-100 ng/µl plasmid DNA was prepared for Sanger sequencing by adding 10 µM sequencing primer (Tab. 2.8). The samples were then sent to Eurofins or Microsynth. Sequence lengths greater than 700 kilobases (kb) were sequenced using a combination of primers to analyze the entire inserted sequence and associated overlapping sequences. The Benchling software was used to align the sequencing results with the *in silico* designed vectors to confirm the absence of mutations. Once the mutation-free bacterial clones were identified, they were transferred from the plates to a 50 ml beaker of LB media with Carb for overnight incubation at 37°C. DNA was extracted from the midi preparations using the Qiagen Plasmid Plus Midi Kit and the QiaVac 24 Plus vacuum manifold. The final plasmids were stored at -20°C for subsequent nucleofections.

2.2.1.2 Cloning of AAV vectors

AAV vectors for injections in mice and transduction in hROs were generated using Gibson assembly (GA) cloning, to assemble multiple overlapping DNA fragments into one AAV vector backbone in a single tube (Gibson et al., 2009). The cone-specific mouse cone arrestin (mCAR) promoter replaced the TetON promoter and was cloned into an AAV vector backbone along with the miRNA overexpression cassettes and the eGFP reporter gene. All GA primers were designed using the Benchling software and purchased from Eurofins Genomics (Tab. 2.8). The mCAR promoter and the miRNA overexpression cassettes were amplified by PCR using the previously described conditions (Tab. 2.10 and Tab. 2.11). The AAV vector backbone was digested with NheI and BsrGI RE enzymes as described in Section 2.2.1.1. The PCR reactions and the digested AAV vector backbone were loaded onto a E-Gel EX 1 % gel to confirm the size of the fragments and the vector backbone (AAV vector backbone: ~2.6 kb; mCAR: ~ 0.56 kb, miRNAs: ~2 kb). After confirming the band sizes, the PCR products were purified prior to the GA reaction. The vector backbone was extracted from the gel and purified. The purified inserts were mixed with 100 ng of digested AAV vector backbone at a 1:2 molar ratio in a maximum volume of 5 µl. The GA assembly mix was purchased from NEB and prepared according to the manufacturer's protocol (Tab. 2.12). The mix was incubated at 50°C for 15 min.

Tab. 2.12: Gibson assembly mix

	2-3 Fragment assembly
Total amount of fragments	0.02 – 0.05 pmols 5 µl
Gibson Assembly Master Mix (2X)	10 µl
Total volume per reaction	20 µl

The chemical transformation procedure was similar to that described in Section 2.2.1.1, but only 2 µl of the chilled assembly mix was added to the bacterial suspension. After the 5 min recovery period on ice, an additional recovery period was added by mixing the bacteria with 1 ml of Super Optimal Broth with Catabolite Repression (SOC) media. This was incubated for 1h at 37°C with 200 rpm rotation to enhance bacterial recovery. After incubation, 100 µl of the DNA/bacteria mix was added to prewarmed LB Carb plates and incubated overnight at 37°C. In addition to the chemical transformation of the assembly

products, the cut backbone was transformed as a control to detect the amount of uncut backbone (background) based on the number of colonies present on the LB plates. If colonies were present, a larger number of colonies was selected from the assembly plates. The next day, 8 to 10 colonies from each vector were again picked for minipreps as described above and prepared for Sanger sequencing. Mutation-free clones were picked for midi preps as described above and stored at -20°C until sent for AAV particle production. All AAV vectors are listed in Tab. 2.6.

2.2.1.3 AAV production

All recombinant AAVs were produced in collaboration with the laboratory of Prof. Dr. Stylianos Michalakis at the Ludwig-Maximilians-University of Munich and were prepared according to previously described methods (Michalakis et al., 2010; Auricchio et al., 2001a; Grieger et al., 2006). The viral serotype AAV2.NN was used because it has been shown to have a favorable tropism for photoreceptor cells *in vivo* and *in vitro* (Völkner et al., 2021; Pavlou et al., 2021). The viral titers and volumes used for each application are summarized in Tab. 2.13. Two different viral batches were used for the postnatal day 21 (P21) and P1 injections in the animal studies. The viral batch used for the hROs was identical to that used for the P1 injections in mice.

Tab. 2.13: AAV vectors and applications

AAV vector	Application	Viral titer (vg/µl)	Volume used (µl)
AAV-mCAR:miR-182-eGFP	Subretinal injections P1	3.5×10^9	0.5
	Subretinal injections P21	2.8×10^{10}	1
	Transduction W19 hROs	3.5×10^9	1
AAV-mCAR:miR-183-eGFP	Subretinal injections P1	3.3×10^9	0.5
	Subretinal injections P21	1.0×10^{11}	1
	Transduction W19 hROs	3.3×10^9	1
AAV-mCAR:miR-124-eGFP	Subretinal injections P1	1.5×10^9	0.5
	Subretinal injections P21	6.6×10^{10}	2

2.2.1.4 Cloning of PB vectors for miRNA expression in hROs

The miR-183 expression cassette from the AAV vectors, with miR-183 expression driven by the mCAR promoter, was subcloned into a PB vector backbone to allow specific

expression of miR-183 in cone PRs of hROs throughout development. To amplify the PCR inserts, the previously described RE cloning method was repeated using RE primers carrying a SpeI or BsrGI RE site (Tab. 2.8). After DNA amplification, the inserts were loaded onto a pre-cast E-Gel EX 1 %, DNA bands of the correct size were excised and purified. The vector backbone and PCR inserts were digested with SpeI and BsrGI restriction endonucleases under the same conditions as described in Section 2.2.1.1. The digested vector backbone was transferred to a pre-cast E-Gel EX 1 % and the correct size backbone was excised from the gel and purified. The PCR insert was purified using the PCR Cleanup Kit. Ligation was performed using the same mixture at a 1:3 molecular ratio and a backbone concentration of 100 ng as previously described. The ligated mixture was again chemically transformed, and sequences were confirmed by Sanger sequencing. The mutation-free bacterial clones were identified, and midi preparations were made to obtain the final plasmids, which were stored at -20°C.

2.2.1.5 Cell culture

A 6-well cell culture plate was coated with Matrigel, prepared by the manufacturer's instructions including the batch dependent dilution factor. The coating solution was incubated for 1h at room temperature (RT) for Matrigel polymerization. Cryopreserved inducible neurogenin (iNGN) cells were thawed using the ThawSTAR™ cell thawing system, then pelleted at 1400 rpm for 4 min after resuspension in PBS. The cell pellet was subsequently resuspended and cultured in mTESR1 medium (mTeSR1 Basal Medium + mTeSR1 5x Supplement + 1 % Pen/Strep) at 37°C and 5 % CO_2 in an incubator. At 80 % confluency, cells were passaged by adding TrpLE to the wells for five min at 37°C. Subsequently, cells were resuspended in PBS, centrifuged, and resuspended in mTESR1 supplemented with CEPT (Chroman 1, emricasan, polyamines, trans-ISRIB, (Chen et al., 2021)). CEPT enhanced cell survival of the human induced pluripotent stem cells (hiPSC) after passaging. The cells were counted using a Countess™ II FL Automated Cell Counter using trypan blue cell stain. For maintenance, the cells were seeded at a density of 18,000 to 20,000 cells/cm². The cell number was adjusted for specific experiments. The seeded cells were initially cultured in mTESR1 with CEPT, which was switched to plain mTESR1 after two days, with daily medium changes. Mycoplasma testing was performed using a

PCR based test kit. For freezing, a total of 500,000 to 1,000,000 cells were resuspended in 500 µl mFreSR medium and cryopreserved at -150°C for long-term storage.

2.2.1.6 PiggyBac nucleofection

The PB vectors carrying the genetic information of the different miRNAs and eGFP under the TetON inducible or mCAR promoter and a Puro resistance gene were nucleofected into hiPSCs using the Amaxa 4D nucleofector protocol. The iNGN cell line as well as the B7 hiPSC cell line were nucleofected (Tab. 2.3). A total of 10 µg PB vector DNA and 2.5 µg transposase DNA were combined in a total volume of 10 µl. The P3 solution/supplement mix was prepared by adding 82 µl of P3 Primary Cell 4D Nucleofector™ X solution to 18 µl of supplement provided in the P3 Primary Cell 4D-Nucleofector™ X Kit. Cells were detached with TrypLE™, centrifuged and resuspended in mTESR1 + CEPT cocktail. The cells were counted using the Countess™ II FL Automated Cell Counter. A total number of 800,000 cells was pelleted at 1400 rpm for 4 min. The cells were resuspended in 100 µl of the P3 solution/supplemented mix and the PB vector DNA/Transposase mix was added to the cell suspension. Subsequently the cells were transferred to a 1 ml Nucleocuvette™ Cartridge and transferred to the Lonza 4D nucleofector applying the CB-150 electric pulse. The nucleofected cells were seeded into a Matrigel-coated 6-well plate. Puro (3 µg/ml) was added to the cell culture medium to select the successful nucleofected cells. A killing control group of cells that had not been nucleofected was used to assess the efficacy of the antibiotic treatment. The selection process was continued until all cells in the antibiotic killing control group had been eliminated. After selection, the cells were propagated and subsequently utilized for the validation of the miRNA overexpression strategy in iNGN cells or growth of hROs using the unmodified B7 (WT) or miR-183 modified cell lines. A stock of cells was frozen in accordance with the procedures outlined in Section 2.2.1.5.

2.2.1.7 Immunohistochemistry

Fixation: The eyes of sacrificed rd1 mice were enucleated after performing the behavioral tests. The retinas were isolated and first analyzed via live fluorescent imaging to obtain

the live eGFP signals. Subsequently, the retinas were fixed for a maximum of 30 min in 4 % paraformaldehyde (PFA) in PBS. The mouse retinas of B6C3F1 mice and the stem-cell derived human retinal organoids (hROs) were fixed for 4 h in 4 % PFA in PBS at 4°C. Following fixation, all samples were washed three times for 30 min. The samples were stored at 4°C in PBS until use. **Vibratome sections:** Fixed rd1 mouse retinas injected at P1 and B6C3F1 mouse retinas were embedded in 3 % agarose (Ultra-Pure Agarose, Thermo Fisher Scientific) in PBS. Vertical 150 µm sections were prepared using a Leica VT1200S vibratome and transferred to a 12-well plate. The sections were permeabilized in 1 % Triton-100X in PBS for 1 h at RT and then blocked in blocking solution overnight at 4°C (Tab. 2.5). Primary antibodies were incubated in the blocking solution for 48 h at 4°C with agitation, followed by five 30 min washes in PBS. Secondary antibodies and Hoechst nuclear stain were then incubated in the blocking solution for 2 h, at RT in the dark with gentle shaking. The antibodies, dilutions, stains, and suppliers are listed in Tab. 2.7 for reference. The sections were then washed three times with 0.1 % Triton X-100 in PBS for 30 min at RT, followed by a final wash in PBS three times for 30 min each. Finally, the sections were mounted on glass slides using ProLong™ Gold antifade reagent. **Cryosections:** Retinas from rd1 mice injected at P21 were cryoprotected using a sucrose gradient (10 %, 20 %, and 30 % for 1-2 h at 4°C). The next day, retinas were placed in a 1:2 mixture of 30 % sucrose and Tissue Tek® O.C.T.™ compound for 1 h and then transferred to cryomolds filled with freezing medium for 30 min before freezing. The sections were stored at -20°C. For immunostaining, slides were dried, marked with a peroxidase-antiperoxidase (PAP) pen, and rehydrated. The slides were heated to 86° to 90°C in sodium citrate buffer. Sections were washed three times for 10 min in PBS, permeabilized in PBS with 0.5 % Tween 20 for 1 h, and incubated with primary antibodies overnight at 4°C. The next day, slides were washed three times for 10 min in PBS, incubated with secondary antibodies and Hoechst for 1 h, washed again three times for 10 min in PBS, and mounted with ProLong™ Gold antifade reagent for confocal microscopy. Antibody dilutions are listed in Tab. 2.7. See Tab. 2.5 for buffer compositions. **Whole-mount stainings:** For staining hROs, whole-mount preparations were used. Permeabilization was performed overnight at 4°C in the same solution used for vibratome sections. Blocking was done for 12 h at 4°C. Primary and secondary antibody incubation followed the same protocol as for the vibratome sections.

2.2.1.8 Live fluorescent microscopy

Live fluorescence microscopy was performed using a 10x objective of the Keyence BZ-X810 fluorescence microscope to visualize eGFP signals in 2D in the iNGN miRNA cell lines after DOX induction. The 4x objective was used for eGFP live fluorescence imaging of *ex vivo* retinal explants of rd1 mice injected at P21. Fluorescence excitation was achieved using a 470 nm LED light source. Emission was collected through a 495-540 nm bandpass filter. The Echo Revolve fluorescence microscope was used to visualize eGFP signals in hROs using a 4x or 10x air objective. Fluorescence excitation was achieved with a 470 nm LED light source. Emission was collected with a 500-550 nm bandpass filter. P1-injected retinas were imaged using a Leica MZ10F modular stereomicroscope equipped with a GFP-specific filter set. The filter set included an excitation filter set (480 nm), a dichroic mirror, and emission filters (510 nm). Images were captured with the integrated camera. All images were post-processed using Fiji.

2.2.1.9 Confocal microscopy

Confocal imaging of stained retinas and hROs was performed using a Visitron VisiScope spinning disk microscope provided by the Microscopy Core Facility of the Medical Faculty of the University of Bonn. C-Apochromat 40x/1.2 water immersion objectives were used. Confocal images were post-processed using Fiji.

2.2.1.10 Real-time quantitative polymerase chain reaction

Real-Time-quantitative polymerase chain reaction (RT-qPCR) allowed the quantification of mRNA from 3D tissues or 2D cell culture samples (Bustin, 2000). Tissue samples from injected animals and their left non-injected sides were snap frozen on dry ice and stored at -80°C for RNA isolation. Cells were detached from the cell culture plates using TrpLE as described in Section 2.2.1.6. and pelleted at 1400 rpm for 4 min. The cell pellets were either snap frozen at -80°C or directly used for RNA isolation. Total RNA, including miRNAs, was extracted using the Qiagen miRNeasy Mini Kit according to the manufacturer's protocol using the Qiacube pipetting robot. The miRNA fraction was

purified using the RNeasy Cleanup Kit, and RNA concentrations were measured using a nanophotometer. For non-miRNA genes, RNA was converted to complementary cDNA (cDNA) using the AB High-Capacity cDNA RT Kit in a 20 µl reaction (Tab. 2.14). 1 µg of RNA was employed for cDNA synthesis, required for the RT-qPCR reaction. The cDNA was diluted in a 1:250 ratio and combined with 500 nM of forward and reverse primers, and 10 µl of Power Up SYBR Green Master Mix (Tab. 2.15).

Tab. 2.14: AB High-capacity RT Kit cDNA synthesis reaction mix

Reagent	**Volume in µl**
10 x RT Buffer	2
25 x dNTPs	0.8
10 x Random Primers	2
Multiscribe Reverse Transcriptase	1
H_2O	4.2
Total RNA (1µg)	10
Total volume	**20**

Tab. 2.15: RT-qPCR reaction mix using the Power Up SYBR Green Mix

Component	**Volume in µl**
PowerUp™ SYBR™ Green Master Mix (2X)	10
Forward Primer (500 nM)	1
Reverse Primer (500 nM)	1
cDNA template + water	2
Total volume/well	**20**

The miRCURY LNA RT Kit (Qiagen) was used to convert the miRNA fraction into cDNA using the recommended mix of components mentioned in Tab. 2.16. A final concentration of 10 ng RNA was used. For the RT-qPCR the miRCURY LNA miRNA PCR Assays (PCR Primer Mixes) for miR-183, miR-183, miR-124 and the 5S-rRNA were used and mixed with a 1:60 dilution of the cDNA sample, 2x miRCURY SYBR® Green Master Mix, RNAse-free water and ROX Reference Dye (Tab. 2.17).

Tab. 2.16: miRCURY LNA Reverse transcription kit for cDNA synthesis

Component	**Volume in µl**
5x miRCURY SYBR® Green RT Reaction Buffer	2
RNAse-free water	4.5
10x miRCURY RT Enzyme Mix	1
Template RNA (5ng/µl)	2
Total reaction volume	**10**

Tab. 2.17: RT-qPCR reaction mix using the miRCURY LNA miRNA PCR assays

Component	Volume in µl
2x miRCURY SYBR® Green Master Mix	5
ROX Reference Dye	0.05
Resuspended PCR Primer Mix	1
cDNA template	3 (1:60 dilution)
RNAse-free water	1.45
Total reaction volume	**10**

All reactions were performed on the QuantStudio™ 3 Real Time PCR System machine using the QuantStudio™ 3 Design & Analysis software. Samples with no cDNA added were included as no template controls for each of the primer pairs to exclude reagent contamination. Primers for testing non-miRNA genes were designed using the Integrated DNA Technologies (IDT) Primer Blast tool or ordered as pre-designed assays from IDT. The data was normalized to the housekeeping genes, *actin-beta* (*ACTB*) when using human samples and to *Actb* when using mouse samples. Relative expression was calculated using the $\Delta\Delta C_T$ method (Livak and Schmittgen, 2001). For the miRNA studies, the 5S ribosomal rRNA (5S rRNA) gene was used as a housekeeping gene (Szymanski et al., 2002).

Human retinal organoids: The retinal parts of the hROs from different time points (W24, W30, W35) were dissected under a microscope using needle tips and immediately snap frozen on dry ice before proceeding with the RNA isolation. Three to four organoids were pooled in one microcentrifuge tube to obtain sufficient RNA for the subsequent cDNA synthesis. All other procedures were conducted in accordance with the previously described procedures for the mouse retinas.

2.2.2 Animal studies

2.2.2.1 Animals

In this study rd1 mice (C3H/J (*Pde6b*^{rd1}) and B6C3F1/Crl mice were used for subretinal injections of AAVs listed in Tab. 2.13. Pregnant rd1 mice were ordered and pups were born in-house for the P1 injection time point. For the P21 injection time point, rd1 mice were ordered at approximately P16 – P18, which also applied to the blind control group

(untreated rd1 mice) and the healthy controls (B6C3F1/Crl). All mice were purchased from Charles River Laboratories (Sulzfeld, Germany) and housed under standard conditions with a 12-h light/dark cycle and access to food and water. Experiments were performed in accordance with institutional and German guidelines for animal care and use approved by the Regional Office for Nature, Environment and Consumer Protection of North Rhine-Westphalia. The use of animals was in strict accordance with the German Law of Animal Protection and the tenets of the Declaration of Helsinki. Mice were euthanized by ketamine/xylazine overdose (300 mg/kg ketamine, 30 mg/kg xylazine IP), and death was confirmed by absence of heartbeat and respiration followed by cervical dislocation as an additional measure to confirm death.

2.2.2.2 Subretinal AAV administration

P21 injections: The subretinal injection procedure was performed as described by (Busskamp et al., 2010). Mice older than P20 were anesthetized with a ketamine/xylazine cocktail (100 mg/ml and 20 mg/ml, respectively), injected intraperitoneally (IP) at 0.1 ml per 10 g body weight. Mice were placed at 37°C during surgery to avoid hypothermia. The depth of anesthesia was assessed via the pedal withdrawal reflex, with surgical tolerance achieved when the reflex was absent. If tolerance was not reached within 30 minutes, additional doses (½ and ¼ of the initial dose) were given. Non-tolerant animals were excluded. The right eye was treated, while the left remained untreated and was protected with ophthalmic ointment. Post-surgery, gentamicin ointment was applied to prevent infection. To reduce animal use in accordance with the 3R principle (Russel and Burch, 1992), miR-182 and miR-183 were co-administered, while miR-124 was injected separately. Mice received carprofen analgesia (5 mg/kg, subcutaneously (SC) for three days after surgery. Animals were monitored using a score sheet. **P1 injections:** Neonatal mice (P1) were anesthetized using hypothermia by placing them on ice (4°C) until they were immobile and unresponsive to toe pinching. Once reflexes were absent, they were transferred to a sterile platform under a dissecting microscope. The eyelid was cleaned with 70 % ethanol, and a small scleral incision was made with a 30-gauge needle. A blunt-tipped Hamilton syringe was used to inject 0.5 µl of viral serum or PBS into the subretinal space. The pups were then warmed on a 37°C heating pad until they regained movement

and were returned to their dam. Neonatal mice were monitored daily for distress using a score sheet. All medications and anesthetics were obtained from the in-house veterinary pharmacy.

2.2.2.3 Visually guided behavioral tests

The light/dark box served as the behavioral test to assess post-treatment visual performance and is based on the natural aversion of rodents against brightly illuminated (Bourin and Hascoët, 2003). The light/dark box test was performed as described by Busskamp et al. (2010), including their method for calculating the time spent in the lit compartment but with minor modifications. Mice (treated rd1; blind controls; healthy controls) were tested between 10 a.m. and 6 p.m. Movement of the mice in the light/dark box was recorded with a webcam (Hama Germany) at a frame rate of 30 frames per second (fps). Visual performance was evaluated at two defined endpoints: P42 to assess short-term effects and initial responses, and P60, to evaluate long-term effects and determine if initial responses were sustained. The AAV-miR-124 cohort injected at P21 was analyzed at P42 only, while the AAV-miR-182/183 cohort injected at P21 was evaluated at both P42 and P60. For the P1 cohort, only the P60 endpoint was analyzed for both treatments. Behavioral analysis was performed without prior knowledge of whether the injections were successful for an objective analysis. The *ex vivo* analysis of the retinal explants allowed later exclusion of animals that were not successfully injected from the data set for final analysis. Mice that spent the entire time in the lit compartment or developed cataracts after surgery were excluded from the analysis. The light/dark box was custom-made of polyethylene terephthalate (PET) with dimensions measuring 26 (width) x 35 (depth) x 15 (height) cm and contained two equally sized compartments: one brightly lit (300 lux) by LED strips mounted on top of the box and one dark (<2 lux). The mice were habituated to the room for 30 min before starting the behavioral test.

Following the light/dark box test, the visual acuity was assessed using the OptoDrum system (Striatech GmbH). The automated system evaluates the optomotor reflex (OMR) by placing mice on an elevated platform surrounded by four monitors. A rotating stripe pattern, presented at full contrast and alternating direction, serves as the visual stimulus.

Stimuli moving in two different directions (clockwise or counterclockwise) allowed for the assessment of the monocular treatment. Visual acuity was measured in cyc/° (total number of stripes/ 360°). Spatial frequency of the stripes and the rotation speed were fixed at 12 °/cycle and controlled by the OptoDrum software. In healthy mice, the rotating stripe pattern elicits a head movement, which is recorded by a top-mounted camera and analyzed by the software. The software tracks the positions of the mouse's nose, midsection, and tail, adjusting for the animal's dimensions before recording.

2.2.3 Human stem-cell derived retinal organoids

2.2.3.1 Human retinal organoid culture

To grow hROs in large quantities, I used the AMASS method as described by (Cowan et al., 2020), using both the B7 cell line and the miR-183 modified B7 cell line. Detailed information on culturing conditions and media compositions are available in the Methods section of the paper. The hROs were collected at W24, W30 and W35 for immunohistochemistry and RT-qPCR, as described in sections 2.2.1.7 and 2.2.1.10.

2.2.3.2 AAV transduction of human retinal organoids

AAV-miR-182 and AAV-miR-182 (Tab. 2.13) were used to transduce W19 hROs. Three organoids per vector were transduced in a 24-well plate coated with an anti-adhesion solution to prevent attachment. The viral titers used were 3.5×10^9 vg/hRO for AAV-miR-182 and 3.3×10^9 vg/hRO for AAV-miR-183: After three days of transduction, the hROs were washed by two medium changes to remove residual viral particles, transferred to a 6-well plate, and then maintained until W22. Transduction success was initially confirmed by live fluorescence signals of eGFP. At W22, hROs were fixed in 4 % PFA, washed, and stained for immunofluorescence using antibodies against retinal cone arrestin-3 (ARR3) and eGFP. A Hoechst stain was used to mark the nuclei of cone cells. For the exact staining procedure refer to section 2.2.1.7.

2.2.3.3 Quantification of AAV transduction in human retinal organoids

To quantify the AAV transduction of cones in hROs, immunohistochemical staining using antibodies against eGFP and ARR3 were performed. Subsequently, the entire depth of four distinct retinal regions of hRO whole-mount preparations were imaged using a confocal microscope (N=4). The total number of cone cells was determined by counting ARR3-positive (ARR3+) cells. Subsequently, the number of cones was determined by counting cones in which the eGFP signal colocalized with ARR3, thereby identifying those that had been successfully transduced. The proportion of successfully transduced cones among the total number of cones present in the hROs was calculated by first determining the number of eGFP positive (eGFP+) cones and then dividing this number by the total cone number. The resulting quotient was then multiplied by 100 %. This procedure yielded the percentage of successfully transduced cones in the various regions.

2.2.3.4 Quantification of cone protrusion length in hROs

To quantify the difference in the protrusion length of cone photoreceptors between WT organoids and miR-183 modified hROs, the protrusion length was measured using Fiji. In WT organoids, the length of the protrusions was quantified on W30 whole-mount preparations that had been stained with ARR3 antibodies. The ARR3 counterstaining facilitated the visualization of cone protrusions, which in turn enabled the subsequent measurement process. In the modified miR-183 organoids, only the protrusions exhibiting colocalization between ARR3 and eGFP were measured, thereby enabling the analysis of only those cones that expressed the miR-183 expression cassette. In each group, four distinct ROIs were subjected to measurement and subsequent quantification (N=4 per group).

3 Results

3.1 Part I*: In vitro* validation of the miRNA expression strategy

3.1.1 Validation of miRNA overexpression using iNGN WT cells as a reference

To confirm whether the overexpression of pre-miRNA sequences results in increased transcriptomic levels of mature miR-182, miR-183 and miR-124, I modified the iNGN hiPSC cell line by nucleofection with the PB vectors, each carrying one of the pre-miRNAs. The iNGN cells, characterized by their ability to differentiate into bipolar neurons upon Doxycycline (DOX) induction, were used for validation. The confirmation of the overexpression was crucial prior to *in vivo* applications since this approach had not been validated previously. Each vector also included an eGFP reporter gene for visual monitoring of expression and a TetON system to control miRNA and eGFP expression in response to DOX. The vector design is shown in Fig. 3.1A.

First live fluorescence imaging was performed four days post DOX induction (dpi) to analyze the live eGFP signals. The unmodified iNGN cells (iNGN WT) were used as experimental reference and subjected to the same treatment. Live fluorescence microscopy showed an increase in eGFP signals over time in the modified miRNA iNGN cell lines, confirming the integration of the PB expression cassettes into the iNGN genome (Fig. 3.1B). All images were acquired with the same exposure time (1.5 s). The iNGN miR-124 showed the weakest eGFP signal of all miRNA cell lines. Differences in PB vector integration were likely responsible for the varying eGFP signals. The copy number was not analyzed, as it was not essential for validating the strategy. Furthermore, morphological differences between the different miRNA cell lines and the iNGN WT cells were observed upon expression of the different miRNAs. At 4 dpi, the miR-124 cell line exhibited more cell clustering compared to the iNGN miR-182 and miR-183 cell lines. Nevertheless, these two cell lines also showed a slight increase in clustering compared to the iNGN WT cell line (Fig. 3.1B). The iNGN WT cells were more dispersed throughout the culture plate and did not show cell clusters. These results suggested a potential influence of the miRNAs on the neuronal cell identity of the iNGN cell line.

In addition to live fluorescence imaging, transcriptomic levels of *eGFP* were examined. To evaluate the relative expression changes between the iNGN miRNA cell lines and the iNGN WT reference cell line, I performed RT-qPCR analysis. The relative change in gene expression levels was calculated as log_2-fold expression using a total of six biological replicates for each cell line (n=6). The *ACTB* gene was used as an endogenous normalization control gene. The total RNA fraction was isolated at 4 dpi. The analysis revealed that the expression level of *eGFP* was upregulated in all iNGN miRNA cell lines compared to the iNGN WT cell line with an average log_2 fold change of 9.34 ± 0.07 (SEM) for the iNGN miR-182 cell line, 8.4 ± 0.10 (SEM) for the iNGN miR-183 cell line, and 7.7 ± 0.16 (SEM) for the iNGN miR-124 cell line. A Mann-Whitney statistical test showed that the differences in *eGFP* expression between the iNGN WT cells and the iNGN miRNA cell lines were statistically significant (**p = 0.002) (Fig. 3.1C).

To confirm the overexpression of the different miRNAs in the distinct iNGN miRNA cell lines, the expression changes of miR-182, miR-183 and miR-124 relative to the iNGN WT reference cell line were analyzed. For this purpose, the miRNA fraction was purified from the total fraction. This was a critical step to increase the sensitivity of miRNA detection among other RNAs present in the total RNA sample (O'Neil et al., 2013; Pritchard et al., 2012). For the miRNA studies, the 5S ribosomal RNA (5S rRNA) gene was used as an endogenous normalization control. The analysis confirmed the upregulation of mature miR-182 in the iNGN miR-182 cell line with a mean log_2 fold change of 13.03 ± 0.41 (SEM), miR-183 in the INGN miR-183 cell line with a mean log_2 fold change of 10 ± 0.28 (SEM) and miR-124 in the iNGN miR-124 cell line with an average log_2 fold change of 6.68 ± 0.31 (SEM) relative to the iNGN WT cell line. A Mann-Whitney test showed that these results were also statistically significant (**p = 0.002, n=6) (Fig. 3.1D). These results indicated that the expected strategy resulted in increased levels of the respective mature miRNAs, confirming the efficacy of the miRNA overexpression strategy.

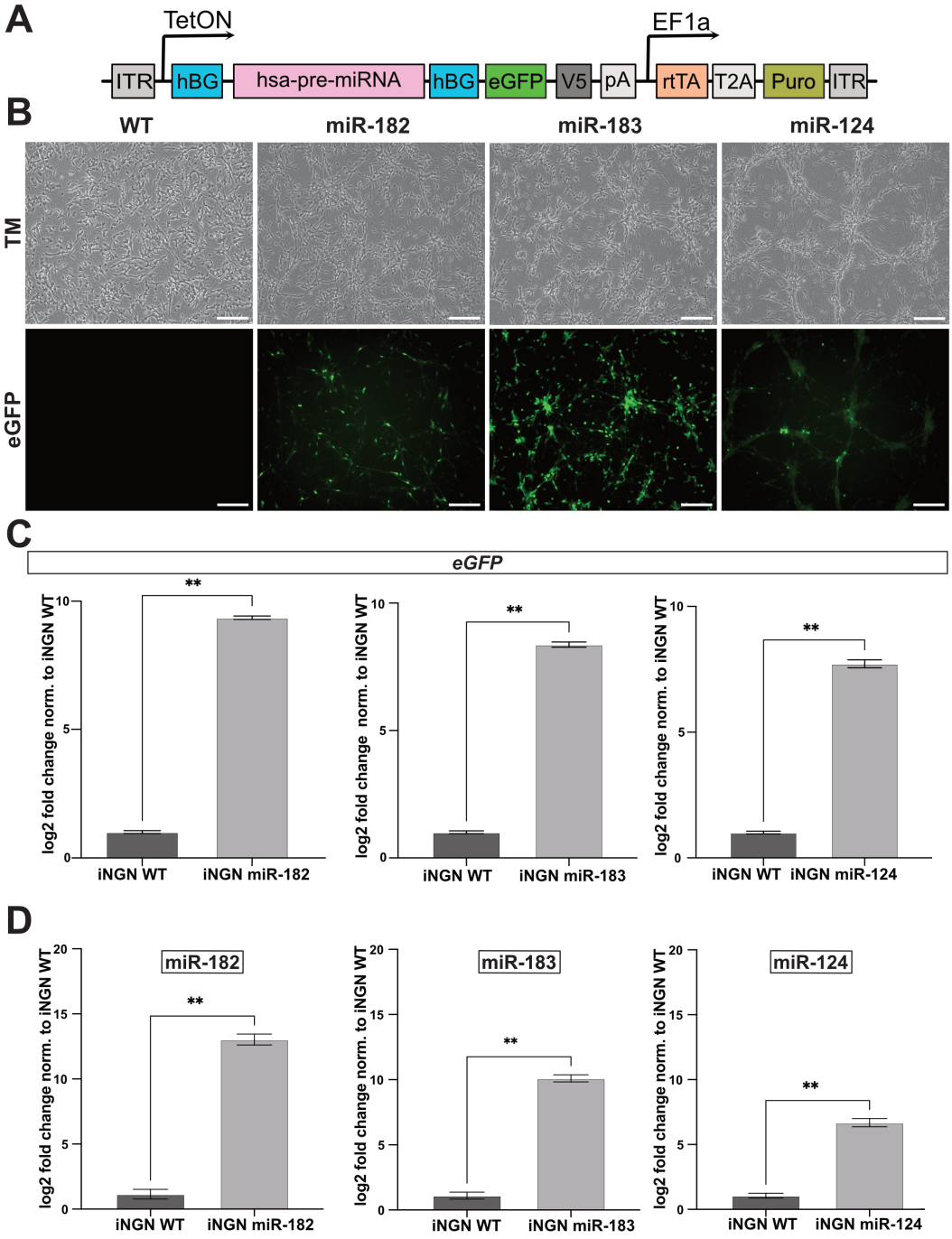

Fig. 3.1 Live fluorescent imaging and RT-qPCR on iNGN WT (reference) and iNGN miRNA cell lines. (A) PB vector showing miRNA overexpression strategy with the human pre-miRNA sequence placed in the intronic region of the hBG and the eGFP reporter gene under control of the TetON inducible promoter. The reverse tetracycline-controlled transactivator (rtTA) allows activation of gene expression in the presence of DOX. The Puro antibiotic resistance gene allows selection prior to DOX induction. ITR, inverted terminal repeat; pA, polyadenylation. **(B)** Fluorescent signals in the iNGN miRNA cell lines after 4 dpi DOX induction in contrast to the iNGN WT cell line with typical bipolar neuronal morphology but no eGFP signal. The distinct morphology of iNGN miRNA cell lines compared to the iNGN WT cell line suggests a potential effect on neuronal cell identity

upon miRNA expression. TM: Transmitted light. Scale bar, 200 µm. **(C)** Significant upregulation of *eGFP* was observed at 4 dpi in all iNGN miRNA cell lines (**p = 0.002, n=6). The data are presented as log_2 fold change, expression relative to the iNGN WT cell lines and normalized to the *ACTB* endogenous control gene. **(D)** The efficacy of miRNA overexpression was confirmed in all iNGN miRNA cell lines, with all miRNAs significantly upregulated relative to the iNGN WT cells. (**p = 0.002, n=6). Data are presented as log_2 fold change expression relative to the iNGN WT cell line, normalized to the 5S rRNA endogenous control gene. Data are presented as mean ± SEM. Statistical significance was determined by a Mann-Whitney test for all analyses.

3.1.2 Validation of miRNA overexpression using iNGN shNTC cells as a reference

I generated a PB vector carrying the shNTC sequence, similar in design to the miRNA overexpression vectors, to incorporate an appropriate control vector for the miRNA studies (Fig. 3.2A). This shNTC sequence, derived from the MISSION® shRNA library (Sigma-Aldrich Merck), was essential to provide a baseline and confirm that the observed effects were due to miRNA overexpression rather than non-specific cellular responses (Moore et al., 2010). The shNTC forms a hairpin structure that interacts with the miRNA processing machinery but, according to the manufacturer, has no mRNA targets. The iNGN shNTC cell line was generated and used as a new reference for RT-qPCR data normalization and subjected to live fluorescence imaging after 4 dpi of DOX treatment.

Live fluorescence microscopy showed that the iNGN shNTC cells were emitting eGFP signals after DOX induction (Fig. 3.2B). The camera sensor exposure time was adjusted to 0.3 s to prevent overexposure when imaging the iNGN shNTC cells, as their eGFP signal was considerably stronger than that observed in the iNGN miRNA cell lines. Note that the microscopic images of the miRNA cell lines shown in Fig. 3.2B are the same as previously shown in Fig. 3.1B. The morphology of iNGN shNTC cells differed from the miRNA cell lines and the typical morphology of iNGN WT cells. Specifically, the axons appeared more retracted, and the somas were smaller.

The transcriptomic analysis of *eGFP* showed that the expression was not always significantly higher in the iNGN shNTC cell line (Fig. 3.2C). In contrast, the *eGFP* expression was still higher in the iNGN miR-182 cell line with an average log_2 fold change expression of 1.3 ± 0.08 (SEM). A Mann-Whitney test showed that these results were

statistically significant (**p = 0.004, n=6). In the iNGN miR-183 cell line, *eGFP* expression did not significantly differ from that in the iNGN shNTC cell line, with an average log_2 fold change of 0.8 ± 0.04 (SEM). The iNGN miR-124 cell line was the only cell line that showed decreased *eGFP* expression compared to the iNGN shNTC cell line with an average log_2 fold change of 0.5 ± 0.05 (SEM). The Mann-Whitney test confirmed that the differences between the iNGN shNTC and the iNGN miR-124 cell line were statistically significant (**p = 0.004, n=6). Note that the iNGN miR-124 generally showed weaker eGFP signals compared to the other cell lines. The differences between the proteomic and transcriptomic levels suggest, that the high proteomic levels of eGFP may have led to downregulation of its expression at the transcriptomic level.

Analysis of the transcriptomic miRNA levels revealed that using the iNGN shNTC cell line as a reference for data normalization resulted in significant changes in the miRNA expression profiles of the iNGN miRNA cell lines (Fig. 3.2D). miR-182 expression was no longer upregulated in the iNGN miR-182 cell line, with an average log_2 fold change of 1.14 ± 0.29 (SEM). Similarly, the miR-183 expression was not upregulated in the iNGN miR-183 cell line. The miR-124 was significantly downregulated in the iNGN miR-124 cell line, with an average log_2 fold change of 0.2 ± 0.05 (SEM). The Mann-Whitney test confirmed that the differences between the iNGN shNTC and the iNGN miR-124 cell line were statistically significant (**p = 0.002, n=6). These results indicate that miRNA expression profiles were altered by using the shNTC sequence as a control sequence.

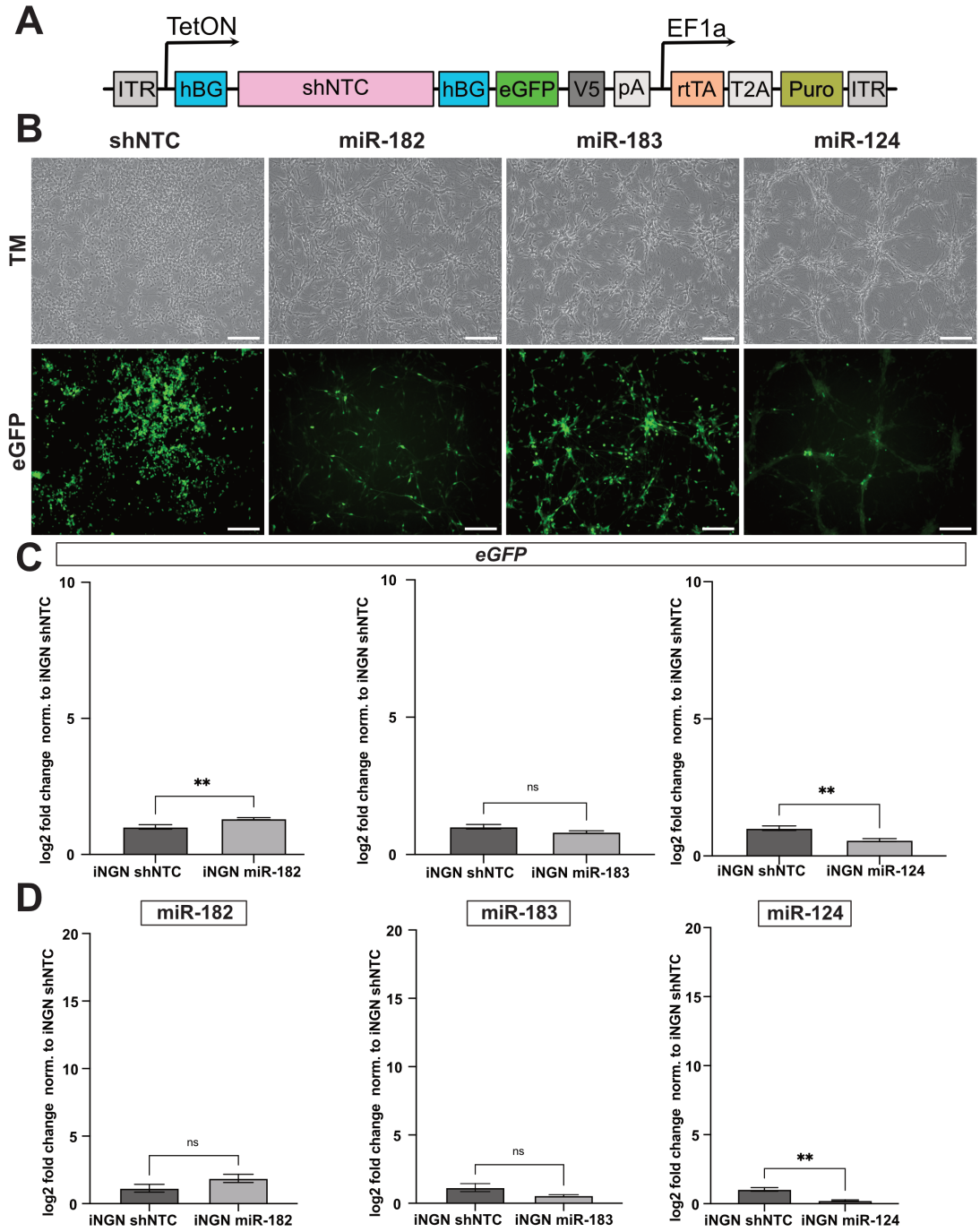

Fig. 3.2 Live fluorescent imaging and RT-qPCR on iNGN shNTC (reference) cells and iNGN miRNA cell lines. (A) PB vector showing shNTC overexpression strategy following the same strategy as the previously described PB miRNA vectors. **(B)** Live fluorescence imaging of iNGN miRNA cell lines and iNGN shNTC expressing eGFP after DOX treatment 4 dpi. The cell morphology of iNGN cells was altered after shNTC expression. Microscopic images of miRNA cell lines are the same as presented in Fig. 3.1B. TM: transmitted light. Scale bar, 200 µm). **(C)** The transcriptomic levels of *eGFP* differed from the proteomic levels in the iNGN shNTC cells. The *eGFP* expression was still significantly increased in the iNGN miR-182 cell line compared to the iNGN shNTC

cells, whereas the *eGFP* expression levels were comparably high between the iNGN shNTC and iNGN miR-183 cell lines. Significantly lower expression levels of *eGFP* were observed in the iNGN miR-124 cell line compared to the iNGN shNTC cell line (**p = 0.004, n=6). Data are presented as log_2 fold change expression relative to the iNGN shNTC reference cell line, normalized to the *ACTB* endogenous control gene. **(D)** The transcriptomic levels of miR-182 and miR-183 in the iNGN miR-182 and iNGN miR-183 cell lines were no longer upregulated relative to the iNGN shNTC cell line. (ns = not significant). The miR-124 expression was strongly downregulated in the iNGN miR-124 cell line (**p = 0.002, n=6). The data are presented as log_2 fold change expression relative to the iNGN shNTC reference cell line, normalized to the 5S rRNA endogenous control gene. Data are presented as mean ± SEM. Statistical significance was determined by a Mann-Whitney test for all analyses.

3.1.3 Comparison of 5S rRNA expression between iNGN shNTC and iNGN WT cells

Altered miRNA expression profiles were accompanied by differences in the C_T values of the 5S rRNA gene between the iNGN WT and the iNGN shNTC cell lines. C_T values indicate the number of PCR cycles required for the fluorescence signal to exceed the threshold, reflecting the presence of the target gene. To gain a deeper understanding of the changes in miRNA expression profiles, I analyzed the ΔC_T values. The ΔC_T value represents the difference between the C_T of the target gene and that of the endogenous control gene; a positive ΔC_T indicates lower expression of the target gene relative to the control, while a negative ΔC_T indicates higher expression (Livak and Schmittgen, 2001). I compared the ΔC_T values of miR-124 and miR-183, relative to the endogenous 5S rRNA control, between the iNGN WT and iNGN shNTC cell lines, as increased levels of miR-124 and miR-183 were detected in iNGN WT cells at 4 dpi (Busskamp et al., 2014b).

The results showed that miR-124 had a lower expression compared to the 5S rRNA gene in the iNGN WT cell line, as indicated by a positive average ΔC_T value of 6.99 ± 0.37 (SEM) (Fig. 3.3). In contrast, miR-124 expression was higher than that of the 5S rRNA gene in the iNGN shNTC cell line, as indicated by a negative average ΔC_T value of -2.35 ± 0.28 (SEM). Similarly, the miR-183 target gene was less expressed relative to the 5S rRNA in the iNGN WT cells, as indicated by a positive average ΔC_T value of 11.08 ± 0.5 (SEM). The miR-183 was also more highly expressed than the 5S rRNA in the iNGN shNTC cell, as indicated by a negative average ΔC_T value of -0.19 ± 0.6 (SEM). A Mann-

Whitney statistical test showed that the differences in ΔC_T values between the two different cell lines were statistically significant for both target genes compared to the 5S rRNA (**p = 0.002, n=6). These results showed that the expression of the 5S rRNA was highly downregulated in the iNGN shNTC cells. As a result, the shNTC sequence was excluded from future *in vivo* and *in vitro* studies to avoid any unwanted effects caused by potential off-target effects.

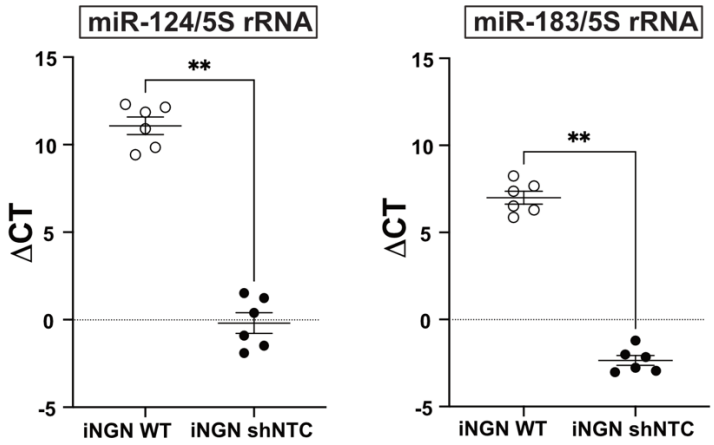

Fig. 3.3 Comparison of ΔC_T values between miR-183 and 5S rRNA, and between miR-124 and the 5S rRNA. The ΔC_T value represents the differences in cycle thresholds (Ct) between the miR-124 target gene and the 5S rRNA reference. The ΔC_T was significantly lower in the iNGN shNTC cell line compared iNGN WT cells (**p = 0.002, n=6). The ΔC_T value was also significantly lower in the iNGN shNTC cell line compared to the iNGN WT cell line when analyzing the differences between the miR-183 target gene and the 5S rRNA (**p = 0.002, n=6). Statistical significance was determined using a Mann-Whitney test.

3.2 Part II: Animal studies

3.2.1 Light/dark box test of rd1 mice treated at P21

To evaluate the potential neuroprotective effect of the different miRNAs on cone OS and cone photoreceptor degeneration at later stages of disease progression, rd1 mice were treated by subretinal injection of AAVs at P21, a time point when rods are completely degenerated and only cones remain (Carter-Dawson et al., 1978). Visual performance was assessed using the light/dark box test (Fig. 3.4B), with untreated rd1 mice (blind

controls) and B6C3F1 mice (healthy controls) serving as references for impaired and normal vision (Bourin and Hascoët, 2003). Analyses were conducted at P42 and P60 to assess both short-term initial responses and the long-term effects. AAV vectors carrying individual pre-miRNAs and eGFP, driven by the cone specific mCAR promoter, facilitated restricted expression in cone photoreceptors. Cone photoreceptor tropism was enabled by the AAV2.NN capsid serotype. The right eye was treated, while the left eye remained non-treated and served as an internal control. Despite a high injection success rate of 93 %, only 53 % of mice were included in the final analysis due to complications such as cataract formation or lack of eGFP signals later observed on *ex vivo* retinal explants. The selection ensured the focus on animals that were successfully treated. Tab. 3.1 summarizes the treatments, analysis time points, and sample sizes used for the final analysis. However, the increased cataract formation notably impacted the statistical power.

Tab. 3.1: Summary of P21 injections

Treatment/control Group	Final analysis TP and total number of injected animals (N)	Successful injections	TPs of analysis	Sample size considered for analysis (n)
AAV-miR-124	P42, 5 animals	4 animals	P42	3 animals
AAV-miR-182/183	P42, 7 animals	7 animals	P42	3 animals
	P60, 3 animals	3 animals	P42 + P60	2 animals
Blind controls (rd1)	P60, 6 animals		P42 + P60	6 animals
B6C3F1 mice	P60, 12 animals		P42 + P60	9 animals

The AAV-miR-124-treated group was analyzed at P42 only. The AAV-miR-124-treated animals spent an average of 42.7 % ± 3.9 % (SEM, n=3) of their time in the lit area, compared to blind controls who spent an average of 53.7 % ± 12.0 % (SEM, n=n) of their time in the lit area and healthy controls who spent an average of 45.3 % ± 4.8 % (SEM, n=9) of their time in the lit area (Fig. 3.4C). Note that three animals in the healthy control group spent 100 % of their time in the lit area and were therefore excluded from the final analysis. Statistical analysis using the Kruskal-Wallis statistical test revealed no significant differences between groups, although AAV-miR-124-treated animals showed a trend toward improved light aversion behavior compared to blind controls.

For the two different AAV-miR-182/183-treated groups (P42 and P60 endpoints), the data from the P42 analysis time point were pooled, increasing the sample size to five animals (n=5) (Fig. 3.4D). The AAV-miR-182/183 treated animals spent an average of 29.4 % ± 6.0 (SEM) of their time in the lit area at P42. For long term effects only two of the animals were analyzed at P60. By P60, these animals spent an average of 36 % ± 1.0 % (SEM, n=2) of their time in the lit area, compared to blind controls, which spent 46.8 % ± 11.9 % (SEM, n=2) and healthy controls, which spent 31.4 % ± 4.8 % (SEM, n=9) on average in the lit area. Again, no statistically significant differences were found, but there was a trend toward increased light aversion in all treated animals. In conclusion, cataract formation reduced the statistical power in all groups, and only trends toward improved light aversion were observed in both miRNA treatment groups.

3.2.2 Visual acuity analysis of rd1 mice treated at P21

Visual acuity was determined using the OptoDrum system (Fig. 3.4E), where the OMR was assessed based on the animals' head movements in response to a rotating stripe pattern (Abdeljalil et al., 2005) (Fig. 3.4E). The stripe pattern was rotated either clockwise or counterclockwise to assess the monocular treatment effects, with visual acuity measured in cyc/°. Healthy controls and visually impaired animals were again used as references. For the control groups, eyes were analyzed separately but the data was pooled later from both eyes for analysis, as only minimal differences were observed between the left and right eyes (healthy controls: N=9 animals, n=18 (eyes); blind controls: N=6, n=12 (eyes)).

In the AAV-miR-124-treated group, the non-treated side showed superior performance compared to the treated side at P42 (Fig. 3.4F). The non-treated sides showed a mean visual acuity of 0.1 cyc/° ± 0.05 cyc/° (SEM, n=3), while the machine was unable to detect a head movement that should have been elicited by the treated side.

In animals treated with the AAV-miR-182/183 group, the non-treated side outperformed the treated side at P42 and P60 in most cases (Fig. 3.4G). At P42, the mean visual acuity for the non-treated side was 0.17 cyc/° ± 0.01 cyc/° (SEM) (Fig. 3.4G). One animal showed

superior performance on the treated side with a visual acuity of 0.22 cyc/° compared to 0.16 cyc/° on the non-treated side (Fig. 3.4G, data point marked in magenta). Since this animal did not undergo behavioral testing at P60, it was not possible to draw conclusion about whether the observed effect was sustained. On all other treated sides, the machine could not detect any head movements during the measurement. At P60, the two animals that were tested exhibited decreased visual acuity in the treated eyes compared to the non-treated eyes. The mean visual acuity of the non-treated side was 0.2 cyc/° ± 0.06 cyc/° (SEM), while no head movement was detected for the treated side.

The results of the OptoDrum measurements of healthy and blind animals are shown in Fig. 3.4H. The mean visual acuity for healthy animals was 0.5 cyc/° ± 0.01 cyc/° (SEM, N=9, n=18) at P42 and 0.46 cyc/° ± 0.02 cyc/° (SEM) at P60. For the blind control group, the mean visual acuity was 0.11 cyc/° ± 0.04 cyc/° (SEM, N=6, n=12) at P42 and 0.07 cyc/° ± 0.04 cyc/° (SEM) at P60. A Kruskal-Wallis statistical test followed by a post hoc Dunn's multiple comparison test showed that the differences between the blind and healthy controls were statistically significant at P42 and P60 (P42: ****$p < 0.0001$; P60: ***$p = 0.0003$). Although the mean visual acuity of the blind animals was greatly reduced compared to the healthy controls, some results from the blind control group were unexpected. For one animal, the algorithm measured a visual acuity close to that of the healthy controls, with values of 0.28 cyc/° at P42 and 0.39 cyc/° at P60 (data point marked in cyan). This may present a false positive measurement, as this level of visual acuity is unlikely at this stage of disease progression. Overall, the data were also more variable in the blind control group. In light of these observations, the results of the OptoDrum studies in visually impaired animals were treated with greater caution, highlighting potential limitations of the system in analyzing visually impaired animals. In contrast, the mean visual acuity of the healthy controls was highly reliable and consistent with values reported in the literature (Da Silva Souza et al., 2011). It can be concluded that the treatment at P21 did not result in an improvement in spatial vision. Visual acuity in the treated animals was highly reduced compared to the healthy animals. Furthermore, the observations suggested that the AAV treatment at P21 may have had possible adverse effects, as indicated by the reduced visual acuity on the treated sides.

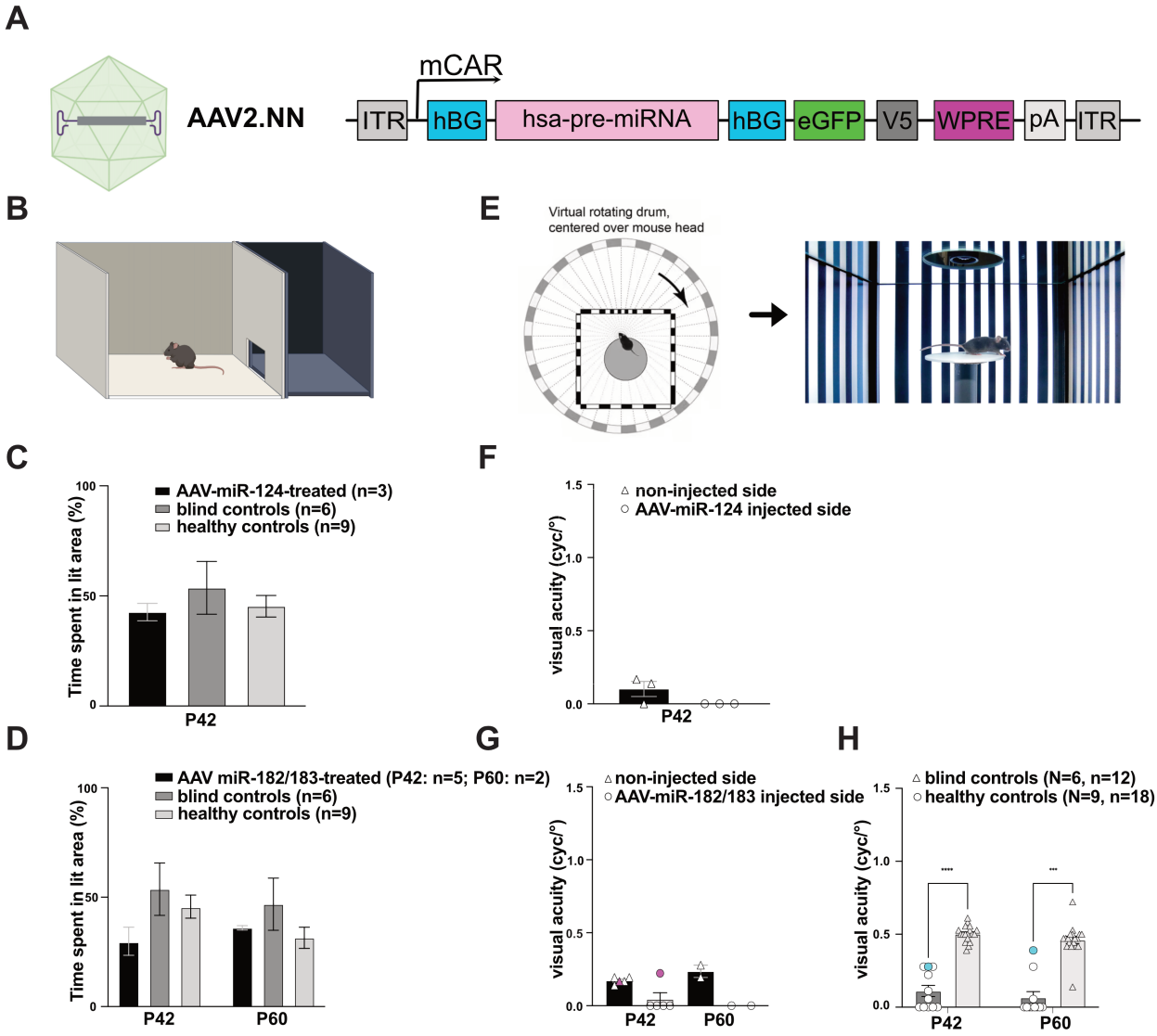

Fig. 3.4 Vision-guided behavioral testing of rd1 mice treated at P21 and controls. **(A)** AAV vector design and capsid variant (AAV2.NN) used**.** miRNA expression is driven by the cone specific mouse cone arrestin (mCAR) promoter. The Woodchuck Hepatitis Virus Posttranscriptional Regulatory element (WPRE) enhances gene expression. AAV illustration adapted from BioRender.com. **(B)** Light/dark box setup. Illustration adapted from BioRender.com. **(C)** OptoDrum setup, presenting a rotating striped pattern to an animal on an elevated platform. Images adapted from Striatech GmbH website. Source: https://stria.tech **(D)** AAV-miR-124-treated animals (n=3) showed better light avoidance at P42 than blind controls (n=6), comparable to healthy controls (n=9). Light aversion behavior was analyzed by determining the time spent in the lit area (%). **(E)** AAV-miR-182/183 treatment resulted in trends toward improved light aversive behavior at P42 (n=5) and P60 (n=2). **(F)** OptoDrum results demonstrated that non-injected sides outperformed the injected sides at P42 after AAV-miR-124 treatment (n=3). Visual performance was measured as visual acuity (cycles per degree, cyc/°). **(G)** Non-injected sides also outperformed injected sides at P42 and P60 after AAV-miR-182/183 treatment, suggesting potential negative effects on visual acuity post treatment. **(H)** OptoDrum visual acuity measurements in blind and healthy animals indicated potential limitations in analyzing

visually impaired animals, with some animals showing unexpectedly high visual acuities (labeled in cyan). Measurements were taken separately for both eyes put pooled for the analysis (blind controls: N=6, n=12; healthy controls: N=9, n=18). Visual acuity in healthy animals was consistent with literature values. Differences between blind and healthy controls were statistically significant at P42 (****p < 0.0001) and P60 (***p = 0.0003). Data presented as mean ± SEM. Statistical significance was determined using the Kruskal-Wallis test followed by a Dunn's multiple comparison test.

3.2.3 Comparison of live eGFP signals on *ex vivo* retinal explants of rd1 mice treated at P21

To examine viral spread in the retinas of animals treated at P21, live fluorescence imaging was performed on *ex vivo* retinal explants injected with the different AAVs. Although live imaging data were collected for the non-injected sides, they are not included in this section for direct comparison due to the lack of eGFP signals. Instead, a comparative analysis of retinal sections from two animals is provided in Section 3.2.7, which includes cone-specific and nuclear markers for immunohistochemical analysis, providing more detailed information. The eGFP signals from the retinal explants of the different treatment groups are shown in Fig. 3.5. Note that some retinas appear folded due to flotation in the dish, and in some cases, only fragments are shown due to ruptures that occurred during dissection. To capture all eGFP signals throughout the retina, some areas appear overexposed due to varying signal intensities in different regions. The AAV-miR-124 group showed widespread eGFP signals throughout the retina at P42, with some areas of high intensity and single foci of eGFP visible throughout the retina. Similar observations were made in the AAV-miR-182/183-treated group at P42 and P60, suggesting that subretinal injections resulted in viral spread beyond the injection side and that AAV2.NN facilitated an effective tropism.

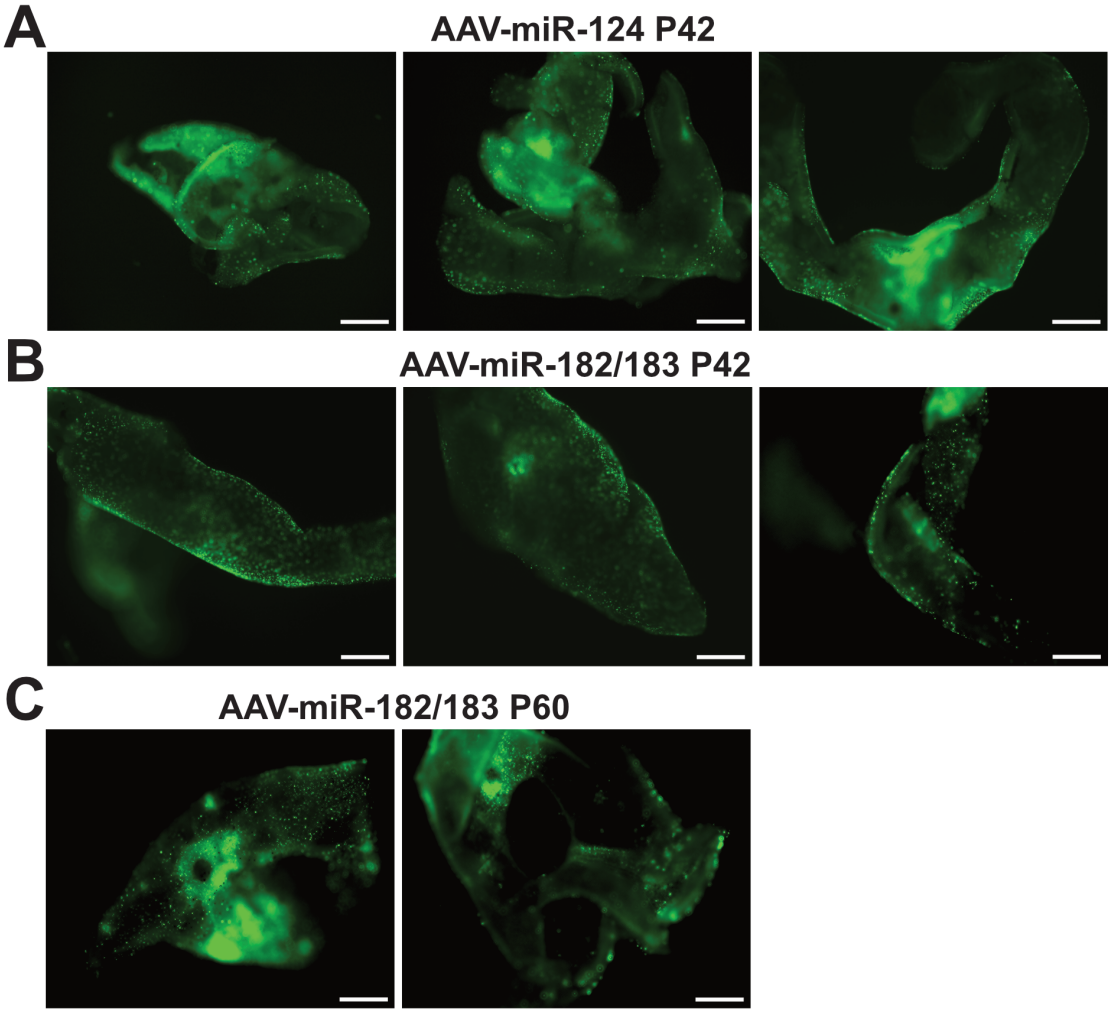

Fig. 3.5 Live fluorescent imaging on *ex vivo* retinal explants of rd1 mice treated at P21. (A) Retinal explant of the three different AAV-miR-124 treated animals that were analyzed behaviorally. All retinas exhibited widespread eGFP signals across the retina at P42. Signals were stronger in certain areas, leading to overexposure in those regions to adequately resolve weaker signals in other areas. Foci display individual eGFP+ cones **(B)** Widespread live eGFP signals of retinal explants at P42 from animals treated with AAV-miR-182/183 at P21. Fragments of retinal tissue were caused by ruptures during the dissection process. **(C)** Live eGFP signals of retinal explants at P60 from animals treated with AAV-miR-182/183 at P21. The two retinas displayed a widespread eGFP signals across the retinas. Scale bars, 500 µm

3.2.4 Light/Dark box test of rd1 mice treated at P1

AAV injections at P1 were performed to express miRNAs before the onset of retinal degeneration in rd1 mice (Pennesi et al., 2012), aiming to assess neuroprotective effects on cone photoreceptors The injections were also conducted before the completion of

retinal development (Mu et al., 2001). Due to the observed superior performance of the non-injected side compared to the injected side at P21, a PBS injection control group was included to evaluate potential side effects of the injection procedure or the treatment itself. For the P1 injections, all animals were analyzed until P60 to assess long-term effects with behavioral assessments performed at P42 and P60, consistent with the methodology used for the P21 group. Animals were excluded from the final analysis if they spent 100 % of their time in the lit compartment, developed cataracts after surgery or were lacking an eGFP signal *ex vivo*, following the same criteria as the P21 cohort. In the PBS injection group, two animals were excluded due to cataracts, leaving four animals for analysis. Tab. 3.2 summarizes the treatments, time points of analysis, number of animals injected, and group size considered for the final efficacy assessment. The success rate for P1 injections was 38 %, with 30 % of animals included in the final analysis. This indicated that the P1 subretinal injection procedure was particularly challenging.

Tab. 3.2: Summary of P1 injections

Treatment/control Group	Final analysis TP and number of injected animals (N)	Successful injections	TPs of analysis	Sample size considered for analysis (n)
AAV-miR-124	P60, 8 animals	4 animals	P42 + P60	3 animals
AAV-miR-182/183	P60, 5 animals	1 animal	P42 + P60	1 animal
PBS	P60, 6 animals	6 animals	P42 + P60	4 animals

The AAV-miR-124-treated group showed a trend towards improved light avoidance behavior compared to the blind control group at P42 and P60 (Fig. 3.6A). Animals spent an average of 44.7 % ± 12.2 % (SEM) of their time in the lit compartment at P42 (n=3) and an average of 40.3 % ± 21.8 % (SEM) of their time in the lit compartment at P60 (n=3). For the blind and healthy animals, the average times spent in the lit compartment were identical to those previously reported in Section 3.2.1 of the results. Once again, the results were not statistically significant, but trends could be observed. The animal that was successfully treated with AAV-miR-182/183 showed a behavioral profile comparable to the blind controls and the PBS injection group, spending 80 % of its time in the lit

compartment at P42 and 64 % at P60 (Fig. 3.6B). This demonstrated that the treatment did not result in improved light aversion.

The PBS injection group spent an average of 64 % ± 4.7 % (SEM) of their time in the lit compartment at P42 (n=4) and an average of 71 % ± 10.0 % (SEM) in the lit compartment at P60 (Fig. 3.6C). The differences between the PBS injection group and the control groups were also not significant. Nevertheless, the PBS injection group showed behavioral profiles comparable to the blind control group. In conclusion, the AAV-miR-124 treatment during the neonatal period resulted in a trend toward improved light aversion behavior, which could not be observed for the animal that was treated with AAV-miR-182/183. The inclusion of a PBS-injection control group demonstrated that improved light aversive behavior observed following AAV-miR-124 injections was likely a positive effect of the treatment.

3.2.5 Assessment of visual acuity of treated animals at P1

The animals treated at P1 also underwent behavioral testing using the OptoDrum to determine the efficacy of the treatment using spatial frequency. In the AAV-miR-124-treated animals, the non-injected side again showed superior visual acuity to the injected side, with an average visual acuity of 0.17 cyc/° ± 0.12 cyc/° (SEM) on the non-injected side at P42 (n=3) and no measurement of a head movement on the injected side (Fig. 3.6D). It is important to note that one animal showed a visual acuity of 0.42 cyc/° on the non-injected side at P42, in contrast to the absence of head movement on the injected side at P42 (Fig. 3.6D, marked in cyan). The same was observed for the P60 time point in this animal exhibiting a visual acuity of 1.0 cyc/° on the non-injected side, leading to an average visual acuity of 0.37 cyc/°± 0.31 cyc/° (SEM) on the non-injected sides. No head movement could be detected on the injected side in this animal again at P60. The data points were retained in the analysis due to the small cohort size, but their interpretation was approached with caution, as visual acuities of 0.42 cyc/° and 1.0 cyc/° on the non-treated sides are again unlikely at this stage of disease progression in rd1 mice.

One animal showed a superior visual acuity of 0.31 cyc/° on the injected side at P60, whereas the non-injected of this animal showed severely reduced visual acuity. However, at P42 this animal showed a visual acuity of 0.08 cyc/° on the non-injected side with no head movement measured on the injected side of this animal at P42. The data points for this animal are highlighted in magenta in Fig. 3.6D. It is noteworthy that this animal also spent only 17 % of the time in the illuminated chamber during the light/dark box test, which was the lowest amount of time of all three animals being tested in this group.

The PBS injection controls were of particular importance for this test, as the injection or treatment at P21 had previously been suggested to have a detrimental effect on visual acuity. The non-injected side did not outperform the injected side in this group. The injected side showed superior performance with a mean visual acuity of 0.2 cyc/° ± 0.09 cyc/° (SEM), while the non-injected side showed a mean visual acuity of 0.05 cyc/° ± 0.02 cyc/° (SEM) (Fig. 3.6F). It should be noted that the visual acuities observed in some PBS-injected animals had high data variability due to unexpectedly high visual acuity measurements on the injected side, particularly at P42, with individual animals exhibiting visual acuities around 0.42 cyc/° (Fig. 3.6F, data points marked in cyan). However, by P60, the visual acuity was severely reduced, with the non-injected side showing an average visual acuity of 0.02 cyc/° ± 0.02 cyc/° (SEM) and the injected side showing an average visual acuity of 0.05 cyc/° ± 0.03 cyc/° (SEM).

In general, the PBS injection group did not show superior performance of the non-injected side compared to the injected sides, as was observed for the P21 injection group. The differences between the non-injected and injected sides were also less pronounced in the P1-treated animals than in the P21-treated animals, especially when excluding the animal that showed unusually high visual acuities on the non-injected sides at P42 and P60. However, drawing definitive conclusions is challenging due to the absence of a PBS injection control group at the P21 time point and the limited size of the P1 injection cohort. The high variability in visual acuities within the PBS injection group, along with the unexpectedly high visual acuities, was consistent with the observations in the blind controls.

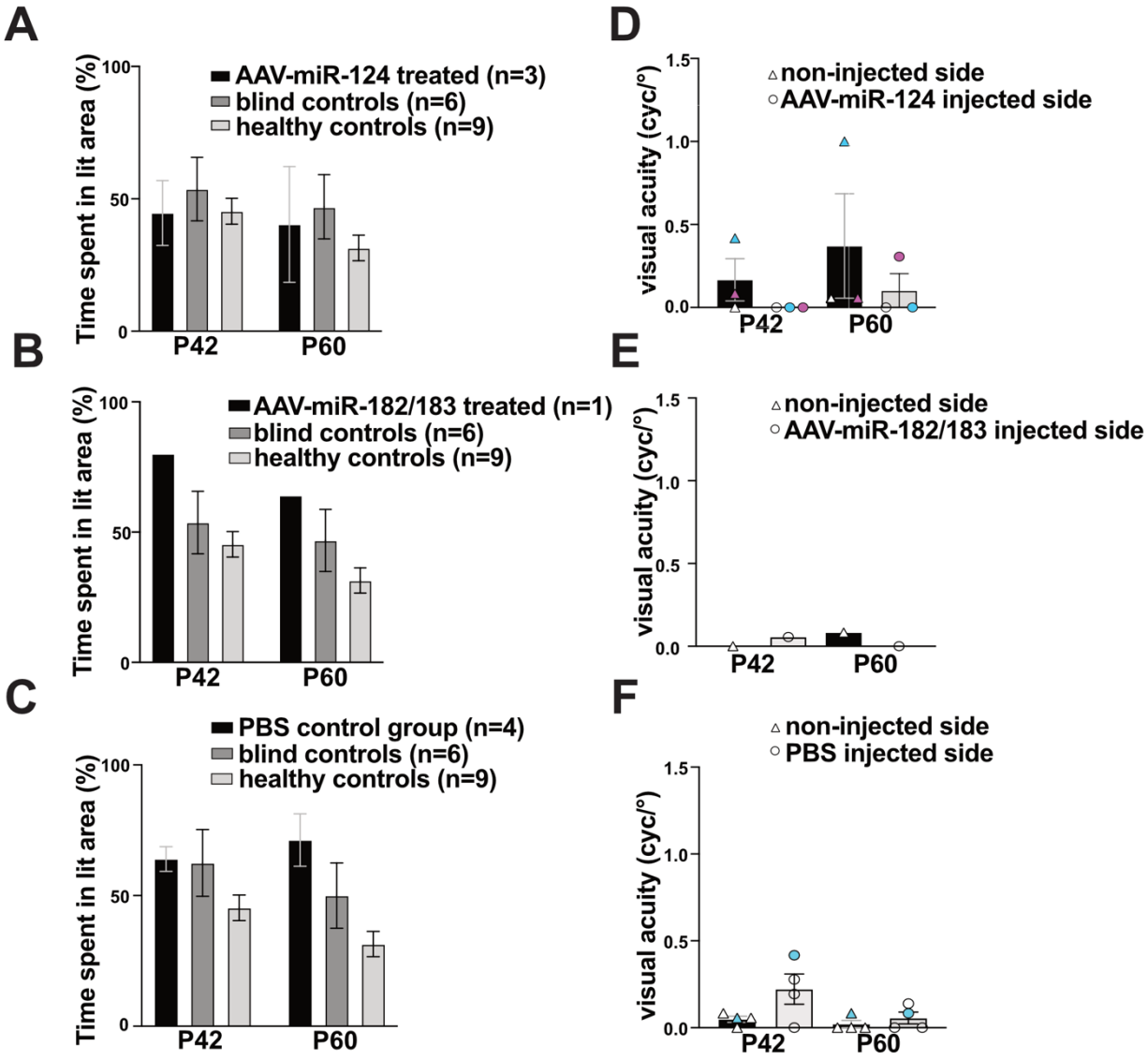

Fig. 3.6 Vision-guided behavioral testing of rd1 mice treated at P1 and PBS injection controls. (A) Light/dark box test of AAV-miR-124-treated animals shows a trend towards improved light aversive behavior at P42 and P60 (n=3). **(B)** AAV-miR-182/183 treatment did not improve light aversion behavior in the one animal treated at P1 **(C)** One animal showed improved visual acuity on the AAV-miR-124 injected side at P60 (shown in magenta) compared to the non-injected side. The same animal is shown in magenta in the P42 data set. One animal showed unexpectedly high visual acuity on the non-injected side (marked in cyan). **(D)** Both the non-injected and injected sides showed severely reduced visual acuities, suggesting no improvement in spatial vision at P42 and P60 in the AAV-miR-182/183-treated animal. **(E)** The light/dark box test of the PBS-injected control animals (n=4) showed behavioral profiles similar to the blind control group, suggesting that the improved light aversion behavior of the AAV-miR-124-treated animals may have been caused by the treatment. **(F)** The PBS-injected group showed that the injected side did not outperform the non-injected side. However, high data variability could be observed on the injected sides at P42. The data are presented as mean ± SEM.

3.2.6 Comparison of viral spread across the retina and transcriptomic data of AAV-miR-124 treated animals at P1

To determine the viral spread across the retina after AAV-miR-124 treatment at P1, *ex vivo* eGFP signals of P60 retinal explants were compared between the three different animals. First live fluorescence microscopy of floating *ex vivo* retinal explants was performed. This revealed that the animal with improved overall visual performance had an extensive eGFP signal with widespread expression throughout the retina (Fig. 3.7A). One animal also showed a stronger eGFP signal throughout the retina (Fig. 3.7B), but some regions appeared to be less transduced compared to the previously mentioned retinal explant, with signals more restricted to specific areas. The third animal showed localized eGFP signals, indicating that the viral spread beyond the injection site was less extensive than in the other two animals (Fig. 3.7C).

Besides live fluorescence imaging, RT-qPCR analysis was performed to assess the transcriptomic levels of *eGFP* and miR-124 in the retinal explants from the three different animals. eGFP positive retinal pieces from the injected side were selected for total RNA and miRNA isolation. Pieces from the non-injected side were selected as an internal experimental reference for the miRNA expression analysis. The *Actb* gene was used as an endogenous control gene for the normalization of the *eGFP* RT-qPCR data, while the 5S rRNA was used as the endogenous normalization control of the miRNA expression analysis. The miR-124 data were normalized to the non-injected side of each animal, as miR-124 is expressed in the retina (Karali et al., 2016). The *eGFP* data was normalized to the injected side of the animal that exhibited increased eGFP signals for comparison. Previously, data was presented using $\log_2$ fold change to present relative changes in gene expression. However, in this section, data are presented as fold change expression to better represent relative changes in gene expression. This method allows for easier interpretation of both decreased and increased expression levels, especially since only subtle changes in gene expression were observed.

The animal with the strongest eGFP signal during live fluorescence imaging also showed the highest transcriptomic levels of miR-124 relative to the non-injected side, with a fold

change of 3.33 (Fig. 3.7A). The animal with the second highest eGFP signal exhibited miR-124 transcriptomic levels comparable to the non-injected side with a fold change expression of 0.86. (Fig. 3.7B). The animal with localized eGFP signals in the retinal explant had a small increase in miR-124 transcriptomic levels on the injected side compared to the non-injected side, with a fold change of 1.48 (Fig. 3.7C). The retina with the strong eGFP signal also had the highest eGFP transcriptomic levels. The other two retinas showed fold change expressions of 0.86 and 0.5 relative to the retina of this animal (Fig. 3.7D). These results were consistent with the live eGFP signal results, suggesting an increased AAV transduction rate in the retina of the animal with improved overall visual performance.

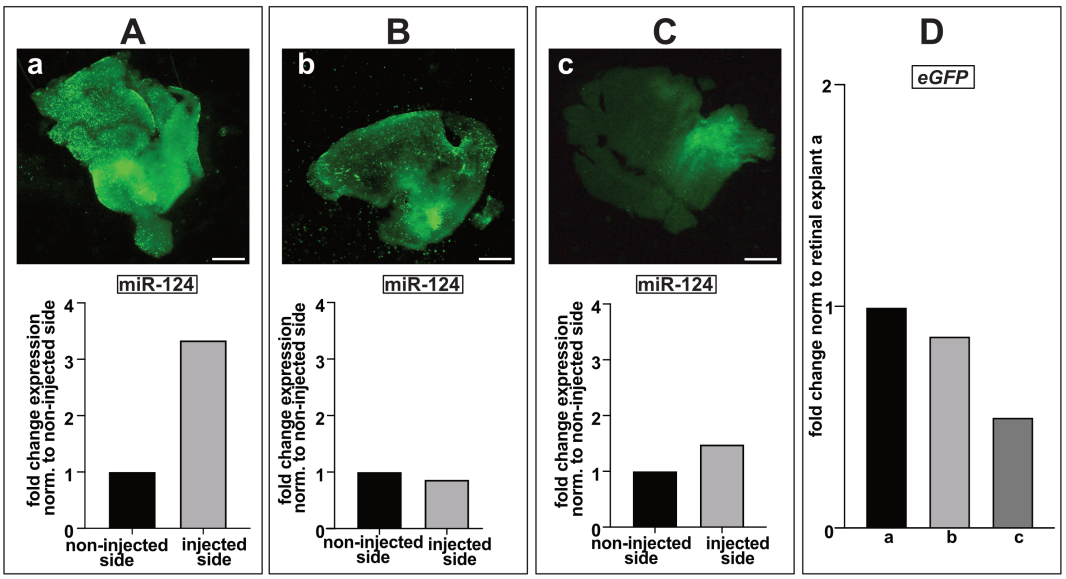

Fig. 3.7 Live fluorescence imaging and RT-qPCR of rd1 mice treated at P1 with AAV-miR-124. (A) Live fluorescent image of *ex vivo* retinal explant (a) and RT-qPCR data showing an extensive eGFP signal across the retina, along with upregulation of miR-124 transcript levels. **(B)** Retinal explant with widespread eGFP signals across the retina (b), though less extensive than in explant (a). The miR-124 expression levels were similar between the non-injected and the injected side. **(C)** Retinal explant showing localized eGFP signals (c) indicating minimal viral spread beyond the injection side. Increased levels of miR-124 were detected on the injected side compared to the non-injected side. RT-qPCR data for miR-124 analysis are presented as fold change expression relative to the non-injected sides, normalized to the 5S rRNA endogenous control gene. **(D)** Transcriptomic analysis of *eGFP* expression across different retinal explants. The data is presented as fold change expression relative to the retinal explant with the highest eGFP signals (A, a). Retinal explants (b, c) showed decreased *eGFP* expression, indicating that the animal with improved overall visual performance exhibited the highest AAV

transduction rate. Data is presented as fold change expression relative to explant a normalized to the *Actb* endogenous control gene Scale bars a-c, 500 µm.

3.2.7 Analysis of retinal structure after AAV treatment of rd1 mice treated at P1 and P21

After *ex vivo* live fluorescence imaging of the retinal explants, the retinas were analyzed by confocal microscopy after preparation of retinal cross sections to analyze structural differences that would indicate preservation of retinal structure after treatment. The injected side was compared to the non-injected side. Antibodies against ARR3 were used to visualize the cones, and antibodies against eGFP. Antibodies against eGFP were used to optimize eGFP fluorescence signals, as signals can be compromised after PFA fixation (Campbell et al., 2022). The Hoechst stain marked the nuclei of the cone cell bodies and cells in the INL and the GCL.

The injected retinas of the P21 animals were embedded in O.C.T.™ compound for cryostat sectioning and examination of P42 and P60 retinas. Unfortunately, the three samples from the P60 group treated with AAV-miR-182/183 could not be preserved during the embedding process in O.C.T.™ compound. As a result, only the P42 time point of both AAV treatments could be analyzed. A single Z-stack from a retinal section of one animal per treatment group is shown in Fig. 3.8, as the retinas appeared structurally similar between animals within each group. The injected sides are shown in direct comparison to the non-injected sides. Fig. 3.8C shows a single Z-Stack of a vibratome section from a healthy retina for reference. The ONL thickness was greatly reduced in P21-treated retinas at P42 for the AAV-miR-124 as well as for the AAV-miR-182/183 treatment groups, compared to healthy control retinas. The retina that was treated with AAV-miR-124 demonstrated colocalization between eGFP and ARR3 of a cone in the ONL (Fig. 3.8A, marked with white arrowhead). The retinal section of the animal that was treated with AAV-miR-182/183 showed cones that exhibited eGFP signals without colocalization with ARR3 signals (Fig. 3.8B, marked with white asterisk (*)). In all treatment groups, the OS were collapsed with only small processes remaining (Fig. 3.8A and Fig. 3.8B marked with white arrows). The non-injected sides did not show any eGFP signals and only demonstrated

ARR3 signals with synapses being still present projecting into the OPL. Note that the eGFP signals on the injected side were sparse in some areas, as only a portion of the retina was sectioned, and not the entire area of transduction could be captured. Since there were no structural differences between the injected and non-injected sides in either treatment group, both of which exhibited highly degenerated retinal morphologies, the treatment did likely not preserve the retinal structure in rd1 mice after treatment at P21. The cones in healthy retinas exhibited the typical morphology of cone photoreceptors, with their OS being present. Note that the section of the healthy retina appears curved, likely because it was not completely flat during the embedding process due to its natural curvature.

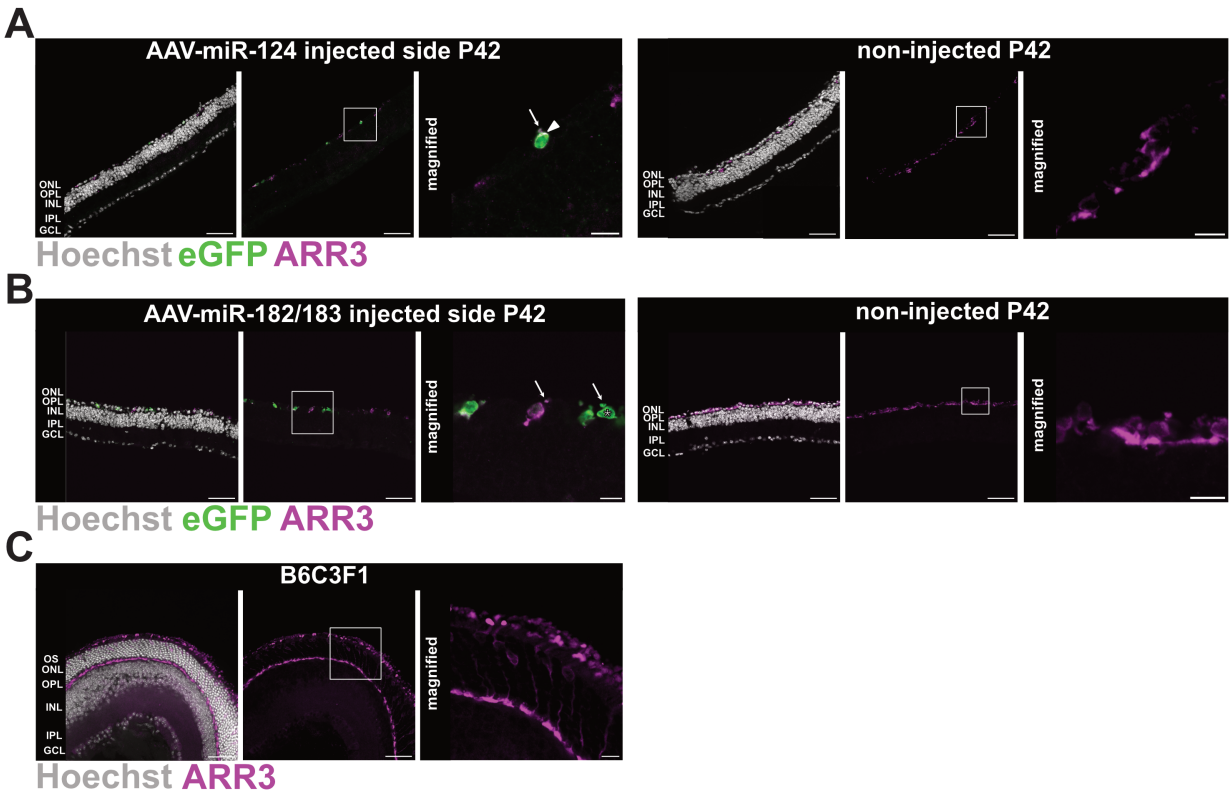

Fig. 3.8 Confocal images of cryosections from two rd1 mice treated at P21, comparing injected and non-injected sides, along with a healthy control retinal cross section. **(A)** Retinal section from an animal injected with AAV-miR-124 at P21, analyzed at P42. eGFP signals were observed in the ONL. Colocalization of ARR3 (cone marker) and eGFP is shown (white arrowhead, magnified). The OS was highly degenerated with only a small tip remaining (white arrow, magnified), and cones were visible as a single cell layer. Hoechst staining (nuclei marker) revealed that the ONL was highly thinned. The non-injected side showed only ARR3 signals and had a similar morphology. **(B)** Retinal section from an animal injected with AAV-miR-182/183 at P21, analyzed at P42. eGFP signals were observed across the ONL. One cone displayed a

strong eGFP signal without ARR3 colocalization (asterisk *, magnified). The ONL was also highly thinned, and the OS were collapsed (white arrow, magnified). The non-injected side had a similar morphology. **(C)** Retinal vibratome section from a healthy control animal. Cones exhibited typical morphology with normal ONL thickness, clearly visible cone OS, and synaptic connections in the OPL, all positively stained with ARR3. Confocal images from two animals are presented, as the morphologies were consistent within each treatment group. Pictures represent a single Z-stack of a retinal section. Scale bars, 200 µm (main images), magnified, 10 µm.

Vibratome sections were prepared from animals injected at P1 to avoid the previously reported loss of tissue observed in P21 retinas after O.C.T.™ embedding. It also facilitated the analysis of a larger vertical region of the retina in a single run by increasing the section thickness to 150 µm. The retinas were stained with the same antibodies as the P21-injected retinas. Fig. 3.9 shows single Z-stacks from retinal sections from the four different animals that were successfully injected with the different AAVs and behaviorally analyzed. All retinas were obtained from animals at P60.

The animal that showed improved visual performance after treatment with AAV-miR-124 had an increased ONL thickness with cone cell bodies present in multiple layers (Fig. 3.9A, marked with arrowheads) compared to the non-injected side at P60, where only a single layer of cone cells was visible in the ONL. Furthermore, the OPL was clearly visible on the injected side but not on the non-injected side at this time point. One cone on the injected side demonstrated a neurite extending into the INL (Fig. 3.9A, labelled with a white asterisk (*)). This level of preservation of the ONL thickness on the injected side was not observed in the retinal sections of the other two animals that were injected with AAV-miR-124 (Fig. 3.9 B and C). This finding suggested that the AAV-miR-124 treatment may have slowed the process of cone degeneration in this animal. The retinas of the other two animals exhibited a decreased ONL thickness, along with a disruption of its morphological organization. In some areas, the ONL was barely distinguishable from the INL. Notably, the retinas of the two other animals showed a high number of eGFP+ cells in the INL and GCL without a colocalization of the ARR3 signal, a feature that was absent in the animal with the preserved ONL structure (Fig. 3.9 B and C, marked with a cross (x)). In these two animals the ARR3 signals were also highly reduced on the injected sides not only compared to the animal that showed improved ONL preservation but also compared to

the non-injected sides. Nevertheless, the OS appeared to be collapsed in the retinal sections of all animals (Fig. 3.9 A-C), suggesting that the OS could also not be preserved when the treatment was applied before the onset of retinal degeneration. In some cases, the eGFP signals were not fully colocalized with the ARR3 signal with sometimes only the synapses showing colocalization (Fig. 3.9A, labelled with a white star). Note that again the eGFP signals were likely sparse because only a part of the retina was analyzed.

The animal treated with AAV-miR-182/183 at P1 showed a highly disorganized ONL that was indistinguishable from the INL (Fig. 3.9D). The OPL was also visible within the tissue and no eGFP or ARR3 signals were observed on the injected side. In contrast, the non-injected sides showed ARR3 signals and a thinned ONL with cone photoreceptor synapses extending into the OPL. This suggests that the subretinal injection of AAV-miR-182/183 at P1 may have had an adverse effect on the development of the structural morphology of the retina.

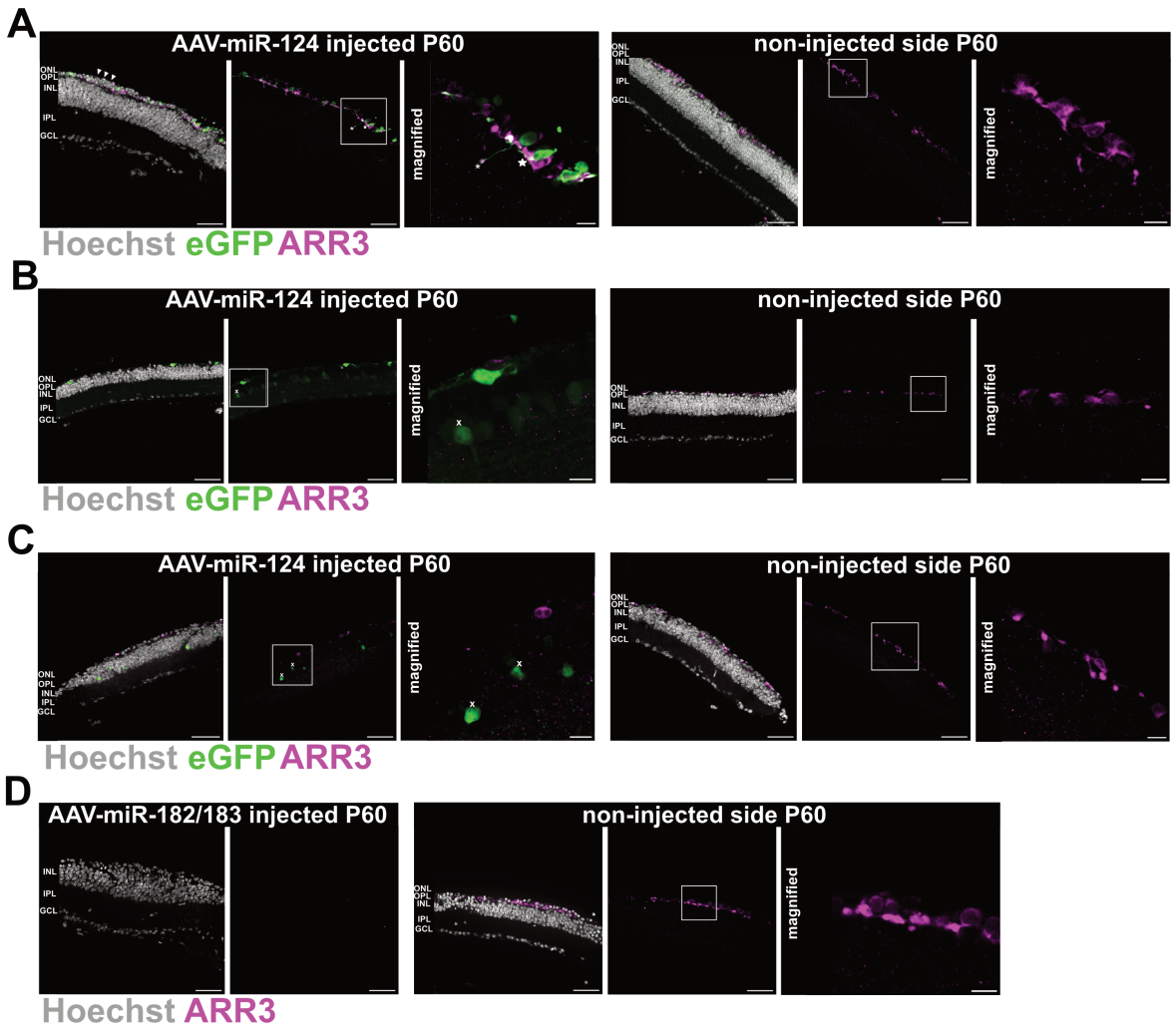

Fig. 3.9 Confocal images of vibratome sections from animals injected at P1 with different AAVs. (A) Confocal image of a retinal section from the animal that showed improved visual performance, with increased ONL thickness after AAV-miR-124 treatment at P60 (white arrowheads). Cone cell bodies were visualized by the Hoechst stain (nuclei marker). eGFP signals were observed in cones and mostly colocalized with ARR3 (cone marker) in the synaptic areas across the retina. The OS displayed a collapsed morphology, without signs of preservation. The non-injected side showed decreased ONL thickness compared to the injected side. **(B)** Retinal section from the second animal, which exhibited the second highest eGFP signal during *ex vivo* live imaging. This animal showed a notable amount of eGFP+ cells in the INL and in the GCL, without colocalization with ARR3 (marked with x). The ONL thickness was highly reduced on both injected and non-injected sides. **(C)** Retinal section from the animal with localized eGFP signals in *ex vivo* explants. eGFP signals were present in the INL and GCL (marked with x) but absent in the ONL. ONL thickness was significantly reduced on both injected and non-injected sides. **(D)** AAV-miR-182/183 treatment at P1 likely resulted in developmental defects in retinal structure, with a missing ONL and no ARR3 and eGFP signals on the injected side. Images represent a single Z-stack of retinal sections. Scale bars, 200 µm (main images), magnified, 10 µm.

3.3 Part III: *In vitro* studies on hROs

3.3.1 AAV transduction rates in hROs

To determine whether the AAVs encoding for miR-182 and miR-183 used in the *in vivo* studies could be applied to hROs, the hROs were transduced with the two different AAVs. These miRNAs were chosen due to their previously reported supportive effects on OS outgrowth in mESC-derived retinal organoids (Busskamp et al., 2014a). Note that a detailed analysis of cone OS development after transduction was not performed, as this experiment focused on proving the concept and optimizing AAV transduction of hROs using the AAV2.NN capsid serotype. The hROs were generated using the AMASS method and maintained in culture for 19 weeks (W19) before AAV transduction. Different titers were applied for each AAV vector: AAV-miR-182 at 3.5 x 10^9 vector genomes (vg)/hRO, and AAV-miR-183 at 3.3 x 10^9 vg/hRO. Three organoids were used for each vector (n=3). Efficiency was assessed by detecting a live eGFP signal by live fluorescence microscopy on the retinal lobes of hROs. Ten days post transduction (DPT), eGFP signals were visible in the outer parts of the retinal lobes (Fig. 3.10). While eGFP signals were faintly visible in deeper layers for both vectors, suggesting the transduction of cones, they were not fully resolvable with live fluorescence imaging.

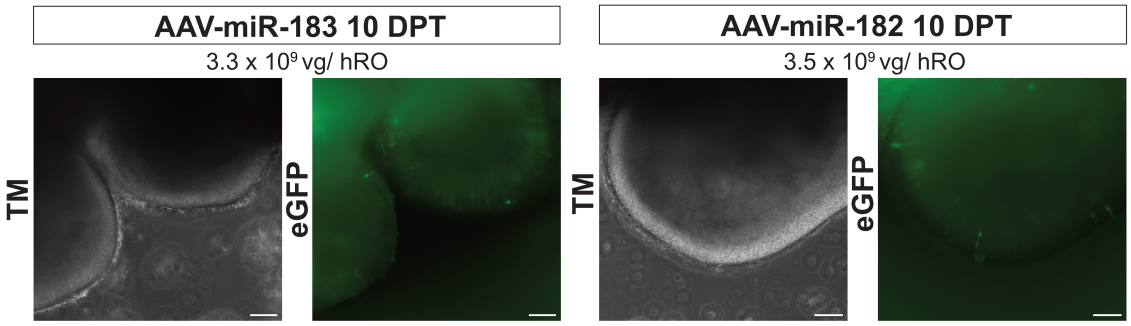

Fig. 3.10 Live fluorescence imaging of AAV transduced hROs at 10 days post transduction (10 DPT). Live fluorescence images of hROs transduced with different viral titers (AAV-miR-183: 3.3 x 10^9; AAV-miR-182: 3.5 x 10^9) 10 days post transduction (DPT). The fluorescence was faintly visible during fluorescence microscopy. TM: transmitted light. Scale bars, 200 µm.

Due to the low resolution of the eGFP signals in the deeper layers of the hROs, confocal microscopy was employed to enhance the visibility of the signals and facilitate the

quantification of AAV transduction efficiency. Consequently, the hROs were fixed at 21 DPT (W22) for immunostaining and confocal microscopy on whole-mount preparations. The organoids were stained with antibodies against ARR3 and eGFP to visualize cones and Hoechst was used to stain nuclei for layer and cell body visualization. Confocal microscopy revealed a higher number of eGFP+ cones in the AAV-miR-183 transduced hROs, indicating that more cones got transduced compared to the AAV-miR-182 transduced hROs (Fig. 3.11A). The quantification of AAV transduction was determined in four distinct ROIs of the retinal lobes of the hROs that had been transduced with both AAVs. The total number of cones was quantified based on ARR3+ stained cells. The number of ARR3+ cells that colocalized with eGFP was counted to identify successfully transduced cones. The transduction rate was calculated as percentage of eGFP+/ARR3+ colocalized cones relative to the total number for ARR3+ cones. The transduction rates are presented in Fig. 3.11B. In the four ROIs of hROs transduced with AAV-miR-183, 144 ARR+ cones were counted, with 109 cones also colocalized with eGFP, resulting in a transduction efficiency of 76,3 %. In contrast, AAV-miR-182 transduced hROs had 106 ARR3+ cones, of which 22 cones were eGFP+, yielding a transduction rate of 21,6 %. A Mann-Whitney test showed that the transduction rate with AAV-miR-183 was significantly higher than with AAV-miR-182 (*p = 0.029). Despite using a higher viral titer for AAV-miR-182, AAV-miR-183 demonstrated a better transduction rate. It should be noted that the subretinal injections in mice at P1 utilized a mixture of these two AAVs, which may have contributed to variability in transduction rates among the animals. Despite the variability, the use of the AAV2.NN capsid serotype was successful in achieving transduction of hROs.

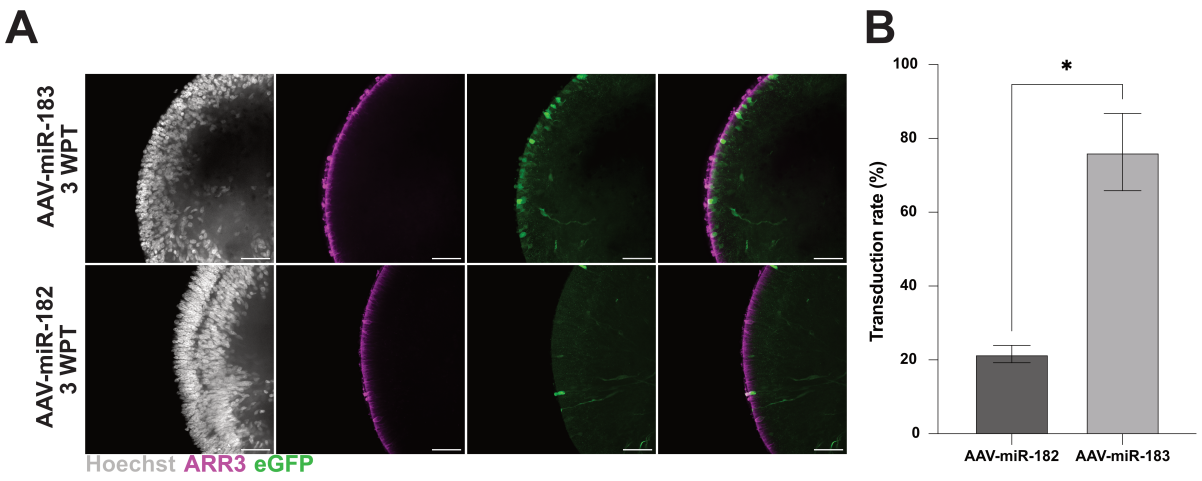

Fig. 3.11 Confocal imaging of AAV transduced hROs and transduction rates of different AAVs. (A) Confocal images of hROs transduced with the two different AAVs at 3 weeks post transduction (WPT) showing eGFP signals. Only one z-plane is shown for demonstration. For quantification, multiple z-planes were acquired and analyzed. Magenta, ARR3 (cone marker); green, eGFP; white, Hoechst (nucleus marker). Colocalization of ARR3 and eGFP appear white due to the overlap of the two emission spectra. **(B)** Bar graph showing transduction rate of hROs using the two different AAV vectors. The y-axis represents the transduction rate (%), calculated as the percentage of eGFP+/ARR3+ colocalized cones among the total number of ARR3+ cones in 4 organoids per group (N=4). Statistical significance was determined using a Mann-Whitney test. Data is presented as mean ± SEM.

3.3.2 Quantification of protrusion length in WT and modified miR-183 organoids

To evaluate the effects of miR-183 on cone maturation in hROs, I introduced a genetic construct encoding miR-183 into the standard hiPSC line (B7) for growing hROs, using the PB transposon system. The purpose of this modification was to generate hROs from the miR-183 transgenic cell line to investigate its potential to accelerate cone development in growing hROs. The choice of miR-183 was based on its critical role in cone maturation, retinal function and photoreceptor survival (Zhang et al., 2020). The expression cassette from AAV vectors was subcloned into the PB vector to drive miR-183 expression specifically in cones, activated by the mCAR promoter during cone development in hROs (Fig. 3.12A). Two independent batches of hROs were generated from the miR-183-modified B7 line and compared with two batches from the unmodified B7 line (WT). Cone protrusion lengths were quantified in both groups, as a key indicator of cone maturation. Live fluorescence imaging was used to monitor the activity of the mCAR promoter based

on the eGFP signals. The live fluorescence imaging demonstrated, that the eGFP signals were weakly visible in the retinal parts of the hRO throughout the entire time course. Consequently, hROs were selected for immunohistochemical staining of whole-mount preparations to enhance the eGFP signals through counterstaining. This approach allowed a more detailed morphological analysis of the modified hROs. The W30 time point was chosen to examine differences in cone protrusion length between WT and miR-183-modified hROs because transcriptomic analysis of cone-specific genes showed that the percentage of cones present in the hROs peaks at W30 (Cowan et al., 2020). To measure cone length in miR-183-modified hROs and WT organoids, four different retinal regions were imaged in both groups (N=4). Cones expressing the PB expression cassette were visualized using antibodies against ARR3 and eGFP. An antibody against L/M opsin was used to specifically visualize the growing protrusions, as the ARR3 antibody stains the entire cone cell. The same antibodies were used for the WT organoids. At W30, cones in the WT hROs appeared less elongated with shorter protrusions (Fig. 3.12B), compared to the miR-183-modified hROs, which had more elongated protrusions, suggesting a more mature morphology (Fig. 3.12C). The eGFP signal was strongly visible at W30 in the miR-183-modified hROs and colocalized with ARR3 staining, suggesting that the expression was specific to cone photoreceptors (Fig. 3.12D). The L/M opsin antibody showed cytoplasmic staining of migrating cones in the central regions of the hROs (Fig. 3.12D, marked with white arrows). These cones also showed eGFP signals in the nucleus. In addition, the protrusions and cytoplasmic region of a single cone photoreceptor in the outer parts of the retinal lobes of hROs were labeled with the L/M opsin antibody (Fig. 3.12C and D, marked with white arrowhead). This cone showed colocalization of eGFP with ARR3 and with L/M opsin, especially in the cone protrusion (Fig. 3.12D, magnified). This cone resembled a highly mature cone morphology, yet it was the only cone in the outer parts of the retinal lobes of the hROs that counterstained with the L/M opsin antibody. No cones were stained with the L/M opsin antibody in the WT organoids (data not shown). To analyze differences in the length of cone protrusions between miR-183-modified and WT hROs, the exact lengths were measured in both groups. In the miR-183 organoids, the length of cone protrusions was measured where eGFP and ARR3 signals colocalized. In the WT organoids, ARR3 staining helped to visualize the cone protrusions for measurement. The arrows in Fig. 3.12E show how the protrusion lengths were

measured as well as the results from the protrusion length quantification. A total of 104 protrusions were measured in the miR-183-modified hROs (N=4, n=104), while 376 protrusions were measured in four ROIs of the WT organoids (N=4, n=376). The discrepancy in the number of protrusions measured is due to the fact that all ARR3+ protrusions were quantified for the WT organoids, whereas only ARR3+/eGFP+ colocalized protrusions were measured for the miR-183-modified hROs. The mean length of protrusions in the WT organoids was 6.1 µm ± 0.12 µm (SEM), whereas the mean length of protrusions observed in the miR-183-modified hROs was 10.53 µm ± 0.31 µm (SEM). A Mann-Whitney test showed that this difference was statistically significant (****$p < 0.0001$). Thus, miR-183-modified hROs exhibited a greater cone protrusion length at W30 compared to the WT organoids, which may indicate higher levels of maturation in the miR-183-modified hROs. Note that it was not possible to observe eGFP signals in hROs harvested for immunostaining at W35. This likely indicates a heterogeneous population of hROs, with some lacking expression of the transgene.

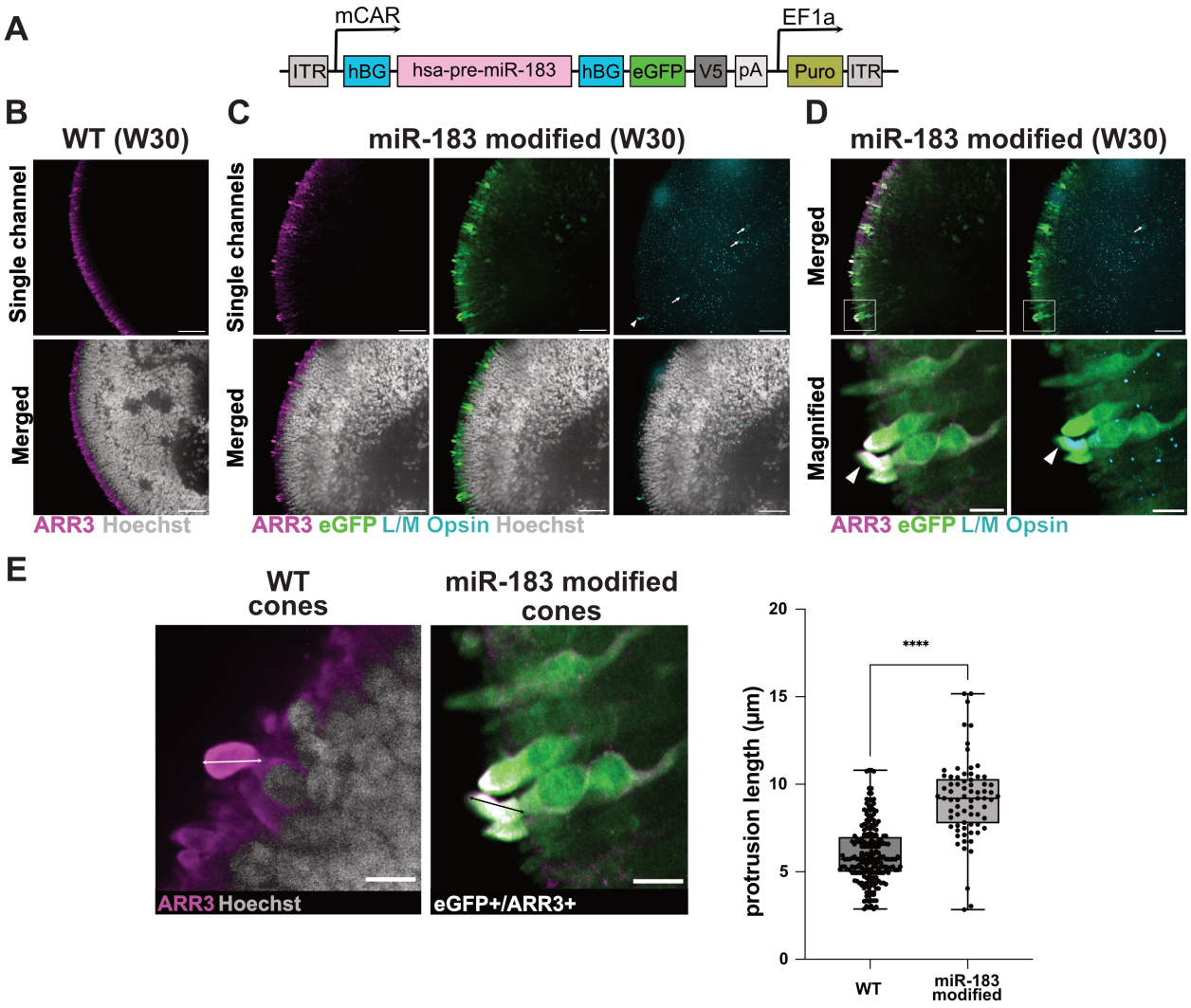

Fig. 3.12 Whole-mount staining of miR-183-modified vs. WT hROs and protrusion length quantification at W30. (A) PiggyBac vector design nucleofected into the B7 hiPSC cell line to generate hROs, with miR-183 and eGFP under the cone-specific mCAR promoter. **(B)** ARR3 staining in WT hROs revealed less elongated shapes of cones in the outer retinal lobes. Hoechst staining visualized the cell nuclei. **(C)** miR-183-modified hROs showed more mature cone morphology with more elongated shapes. Staining with ARR3 and L/M opsin indicated colocalization with eGFP. Cytoplasmatic staining of L/M opsin staining was observed in the central parts of the hROs (white arrows) as well as in a protrusion of a cone in the retinal lobe (white arrowhead). **(D)** Overlay of ARR3+/eGFP+ and L/M-opsin+/eGFP+ highlighting colocalization, especially in the protrusion (white arrowhead, magnified). **(E)** Protrusion length (µm) was measured and quantified in four different retinal lobes. For measurement, ARR3 staining was used in WT organoids, while eGFP/ARR3 colocalization was used in miR-183-modified organoids. The miR-183-modified hROs had significantly longer protrusions compared to WT hROs (****$p < 0.0001$, WT hROs: N=4, n=104; miR-183-modified hROs: N=4, n=376). Statistical significance was determined by a Mann-Whitney test. Data is presented as mean ± SEM.

3.3.3 Temporal analysis of miR-183 and *eGFP* expression levels

For the transcriptomic analysis of *eGFP* in miR-183-modified hROs and miR-183 levels in both hRO groups, total RNA and miRNA fractions were isolated from dissected retinal regions at different stages of hRO development. Dissection ensured the exclusion of organoids that failed to form hROs and the exclusion of non-retinal parts. The W24 time point was chosen as the baseline for data normalization because the number of cones begins to increase at this time (Cowan et al., 2020). Subsequent time points (W30 and W35) were normalized to W24 within their respective groups for temporal analysis. For each time point, 16 retinal regions were analyzed, with four regions pooled per sample (N=4, n=16). RT-qPCR analysis revealed a gradual increase in *eGFP* expression, with a mean $\log_2$ fold change of 1.22 ± 0.08 (SEM) at W30 and 1.64 ± 0.23 (SEM) at W35 in miR-183-modified hROs (Fig. 3.13A). However, a Kruskal-Wallis statistical test showed no significant differences in *eGFP* expression between time points.

The expression levels of miR-183 were compared between WT hROs and miR-183 modified hROs at the same developmental time points as previously described for the *eGFP* expression analysis. Previous studies have shown that miR-183 is generally expressed in hROs organoids, which allowed normalization to the W24 time point within each group (Celiker et al., 2023). The miR-183 expression increased from W24 to W30 in the WT organoids, with a mean $\log_2$ fold change of 3.44 ± 0.03 (SEM) (Fig. 3.13B). However, the Kruskal-Wallis statistical test showed that the increase was not statistically significant. By W35, the miR-183 expression levels decreased in WT organoids to a mean $\log_2$ fold change of 2.34 ± 0.61 (SEM), which also showed no significant difference from the other time points. In miR-183-modified hROs, miR-183 expression significantly increased from W24 to W30 with a mean $\log_2$ fold change of 5.28 ± 0.32 (SEM) (Fig. 3.13C). The Kruskal-Wallis-test confirmed a significant difference in miR-183 expression between the time points (**p = 0.0048). The post-hoc Dunn's test further revealed that miR-183 was significantly higher at W30 compared to W24 (*p = 0.018). Although the increase in WT organoids was not statistically significant, the trend suggests a potential role for miR-183 in cone photoreceptor development in the hROs.

Given the different experimental reference conditions between the two organoid groups, with W24 serving as the baseline within each group, direct comparison of miR-183 expression between WT and miR-183-modified hROs was challenging. To enable a valid comparison at W30 – where significant miR-183 upregulation was observed in the modified organoids – both data sets were normalized to a common reference, the W24 time point of WT hROs. Comparative analysis revealed that miR-183 expression at W30 was significantly higher in the miR-183 modified hROs, with a mean log_2 fold change of 4.44 ± 0.21 (SEM) compared to 3.44 ± 0.08 (SEM) in WT organoids (Fig. 3.13D, Mann-Whitney test, *p = 0.02). This two-fold increase in the miR-183-modified group may have contributed to enhanced cone photoreceptor maturation and protrusion length.

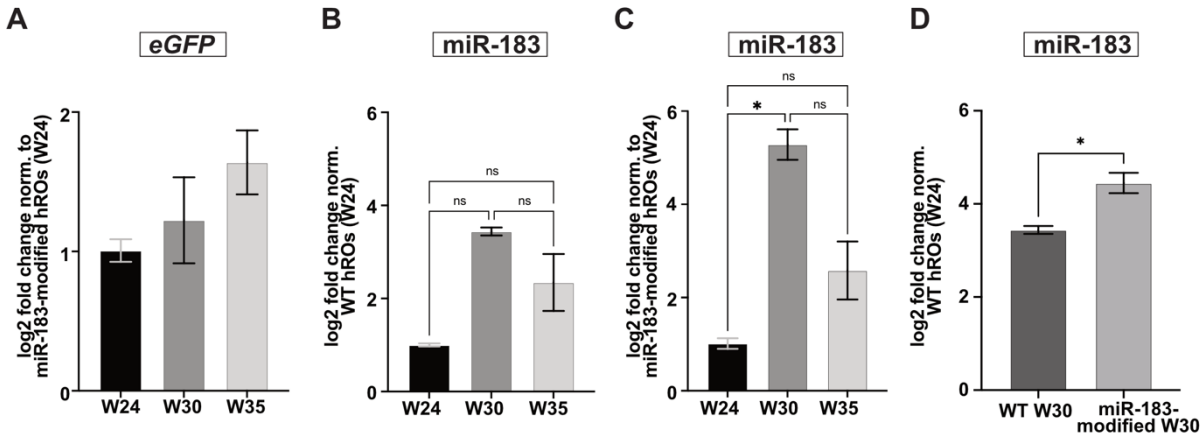

Fig. 3.13 Transcriptomic analysis of *eGFP* and miR-183 in WT and miR-183-modified hROs. (A) *eGFP* expression in miR-183-modified hROs increased from W24 to W35, presented as log_2 fold change relative to W24 and normalized to the *ACTB* control gene **(B)** miR-183 expression in WT hROs showed an increase from W24 to W30, followed by a decrease from W30 to W35, presented as log_2 fold change relative to W24 and normalized to 5S rRNA endogenous control gene (N=4, n=16). **(C)** miR-183 levels in miR-183-modified hROs significantly increased from W24 to W30 (*p = 0.018), then decreased from W30 to W35, similar to the WT hROs. Expression is calculated relative to W24 miR-183-modified hROs. **(D)** Normalization to a common reference (W24 WT hROs) showed significantly higher miR-183 expression in the miR-183-modified group at W30 (*p = 0.02). Data are presented as mean ± SEM. Statistical significance was determined using a Kruskal-Wallis test followed by a post-hoc Dunn's multiple comparison (B,C) as well as a Mann-Whitney test (D). A total of 16 retinal lobes were dissected, with four retinal lobes pooled per sample for both groups (N=4, n=16).

4 Discussion

4.1 Inducible expression of shNTC sequence alters gene expression in iNGN cells

RNAi is a powerful tool for studying gene function by exploiting the natural post-transcriptional gene silencing mechanism of eukaryotic cells (Fire et al., 1991). miRNAs regulate gene expression by sequence-specific binding to mRNA targets (Lee et al., 1993; Sontheimer and Carthew, 2005; Bartel, 2004; Shi, 2003). To determine the functions of specific miRNAs, overexpression studies in cultured cells and animals are commonly used (Vidigal and Ventura, 2015). This study focused on analyzing the effects of miR-182, miR-183 and miR-124 on cone photoreceptors, which required an effective overexpression strategy. The strategy was validated using RT-qPCR and live fluorescent imaging of iNGN WT and iNGN miRNA cell lines and revealed morphological differences between the miRNA cell lines and the WT cells. It was proposed that the miRNAs had an impact on the neuronal cell fate of iNGN cells, given their important role as central regulators of neuronal cell fate (Sun et al., 2013). Therefore, future research could investigate how miRNA expression influences the neuronal cell fate of iNGN cells. In conclusion, the successful validation of the miRNA overexpression strategy provided a basis for the *in vivo* studies to investigate the impact of these miRNAs on degenerating photoreceptors.

RNAi studies involving miRNAs typically require appropriate controls (Czarnek et al., 2021; Moore et al., 2010). shNTCs are used because their structural similarity to the pre-miRNA allows them to interact with the miRNA processing machinery without targeting any mRNA targets. This helps to ensure that observed effects are due to the gene-targeting miRNAs rather than unrelated factors. In this study, the commercially available shNTC from the MISSION® shRNA library (Sigma-Aldrich Merck) was introduced into the iNGN WT cell line (Busskamp et al., 2014b). The resulting iNGN shNTC cell line, used as the new normalization control, resulted in altered miRNA expression profiles in the iNGN miRNA cell lines, suggesting potential off-target effects. Recent reports also indicated that inducible expression of this shNTC in murine and human tumor cell lines silenced the core component of the spliceosome, the small nuclear ribonucleoprotein Sm D3 (SNRPD3).

This led to unexpected effects, including cell death or permanent growth arrest (Czarnek et al., 2021). Such off-target effects are not unusual and have been observed with other shRNAs used in RNAi studies (Hasegawa et al., 2017; Goel and Ploski, 2022). Although my results did not report increased cell death or growth arrest, likely due to using a different cell type, significant downregulation of the endogenous control gene 5S rRNA was observed in the iNGN shNTC line compared to iNGN WT cells. This downregulation affected the miRNA expression levels when normalizing RT-qPCR data to the iNGN shNTC cell line. Additionally, iNGN cell morphology was altered, with shNTC likely causing axon retraction and cell soma shrinkage. Given that miRNAs bind in a partially complementary manner to the 3' UTR of their mRNA and can target multiple mRNAs with similar sequences (Felekkis et al., 2010; Lewis et al., 2005), it is likely that the shNTC has several off targets beyond SNRPD3. The downregulation of the 5S rRNA transcript levels might be due to translational inhibition of mRNAs encoding for the RNA polymerase III subunits, which are crucial for 5S rRNA transcription (Ciganda and Williams, 2011). However, this hypothesis needs further investigation. Off-target effects of small interfering RNAs (siRNAs) can also increase in a dose-dependent manner (Wang et al., 2009). This suggests that the inducible expression of shNTC may have contributed to the observed effects. The original commercially available plasmid vector uses the U6 promoter, which is effective for shRNA expression due to its direct recognition by RNA polymerase III (Paule and White, 2000; Miyagishi and Taira, 2002). This supports the notion that the replacement with the TetON inducible promoter may have contributed to unusual shNTC expression levels, leading to unintended off-target effects. In addition, the stronger eGFP signal in the iNGN shNTC cell line might have induced oxidative stress, which can alter gene expression (Ganini et al., 2017). Despite this, RT-qPCR did not show increased transcriptomic levels of *eGFP*, possibly because of high protein levels that led to the downregulation of *eGFP* transcripts. Further investigations are needed to clarify these discrepancies.

In conclusion my results highlighted the limitations of using the shNTC as a control sequence and highlighted the difficulty in adapting the expression strategy to the experimental design. These observations also emphasize the challenge of selecting an

appropriate control vector for RNAi studies. Ultimately, the shNTC was unsuitable as a control vector for the miRNA studies *in vivo*.

4.2 miRNA overexpression at P21 enhances light aversion behavior

The light/dark box test is an effective tool to analyze visually guided behavior (Bourin and Hascoët, 2003). It is based on the aversion of mice against brightly lit areas and demonstrated improvement of light aversion behavior after treatment of visually impaired mice in previous studies (Busskamp et al., 2010). The light/dark box test also demonstrated in the present study, that rd1 mice that were treated at P21 exhibited a trend towards increased light aversion at P42 and P60 following treatment with AAV-miR-124 and AAV-miR-182/183 compared to the blind control group. This reinforced the effectiveness of the light/dark box as a useful initial assessment tool for improved visual performance post-treatment. These results highlighted the potential of miR-124, miR-182 and miR-183 of improving light avoidance behavior when administered at a progressed disease stage. This effect may be linked to the beneficial effects of miRNAs in modulating inflammatory immune responses in the degenerating rat retina (Saxena et al., 2015). The dysregulation of miR-124 has been associated with increased retinal inflammation and photoreceptor loss, which are typical characteristics of retinal degeneration (Chu-Tan et al., 2018). The same study demonstrated that the subsequent intravitreal administration of miR-124 mimics in mice led to a reduction in both retinal inflammation and photoreceptor loss. Given that ocular inflammation is a contributing factor in the progression of retinal degeneration in rd1 mouse models and RP patients (Mohan et al., 2022), it is plausible that the observed improvements in light aversive-behavior following AAV-miR-124 treatment reflect an immunomodulatory effect. This potential effect requires further investigation to fully understand the mechanism and therapeutic implications in a larger cohort to increase the statistical power. Furthermore, precise miRNA processing and function is essential for maintaining cone OS survival. The conditional knockout of the DGCR8 protein in cone photoreceptors, a subunit of the microprocessor complex, led to the loss of cone OS *in vivo* (Busskamp et al., 2014a). In this context, miR-182 and miR-183 were identified as the two miRNAs that were sufficient to preserve cone OS. The same study demonstrated that the introduction of the miRNA cluster miR-182/96/183 into

mESC-derived retinal organoids resulted in the formation of light-responsive OS. Although structural preservation of cone OS could not be confirmed in retinal sections from P21 injected rd1 mice, a trend towards improved light avoidance behavior was also observed in the AAV-miR-182/183-treated group. This suggests a potential neuroprotective effect of miR-182 and miR-183 on cones, which also requires further investigation in a larger cohort.

4.3 Cataract formation may be associated with anesthesia for subretinal injections at P21

Not all animals underwent behavioral testing for the final therapeutic assessment due to the development of cataracts post-surgery. It was hypothesized that this was likely caused by the anesthetics used for the subretinal injection procedure. The anesthetic combination of ketamine and xylazine was safely used in studies where subretinal injections were performed in P21 old mice (Qian et al., 2022). However, it was reported that the combined administration of ketamine and xylazine can lead to the acute formation of reversible cataracts (Calderone et al., 1986). My results showed no evidence of reversibility of the cataract; rather, the cataracts were irreversible. This was a potential indication that additional factors may have contributed to the formation of cataracts, such as corneal dehydration or hypothermia during the subretinal injection procedure (Boyd and Petersen-Jones, 2024). Constant monitoring of these factors is essential to prevent these adverse effects. Complications may also arise from the subretinal injection procedure itself, which may promote cataract formation or even retinal detachment (Qi et al., 2015; Parikh et al., 2016). However, the access to the subretinal space through a posterior transscleral approach, which was also used in this study, has been associated with a reduction in collateral damage, such as cataracts, in comparison to the commonly used anterior approaches (Parikh et al., 2016). It is important to emphasize that due to the collateral damage that may be caused by the subretinal injection procedure itself, there remains a need for the development of optimized viral capsid variants in the field of ocular therapies that can be safely delivered via the minimally invasive intravitreal route, with the goal of improved capsid variants to reduce immunogenicity (Timmers et al., 2020). In any case, the animals were excluded from the behavioral trials, which resulted in a reduction in

statistical power and the absence of statistically significant differences between the blind animals and the treated animals due to the small cohort size. In sum it seems reasonable to recommend alternative anesthetic compounds to circumvent the formation of cataracts. Anesthetics that can be reversed at any time by other agents may also be helpful in preventing body temperature fluctuations that can favor cataract formation. Cardio depressant effects of ketamine/xylazine anesthesia can be reversed with the antagonist atipamezole, which could also be considered for future studies (Gargiulo et al., 2012).

Despite cataract formation, my results demonstrated that the subretinal injections in rd1 mice at P21 achieved high success rates, as demonstrated by live eGFP fluorescence in numerous *ex vivo* retinal explants at P42 and P60. The results confirmed that the AAV2.NN serotype and the subretinal route of administration were effective for targeting photoreceptors *in vivo* and were consistent with the results of previous studies (Pavlou et al., 2021; Acland et al., 2001; Russell et al., 2017).

4.4 Treatment may have negative effects on spatial vision in animals injected at P21

The OMR test is a valuable tool for assessing spatial frequency and contrast sensitivity in various retinal disease models and is widely used to evaluate the efficacy of therapeutic interventions (Gudapati et al., 2020; Shi et al., 2018). The OMR is an innate compensatory eye movement in response to a moving stimulus and results in a head movement in healthy animals in the direction of the stimulus (Cowey and Franzini, 1979). The visual tracking drum is a reliable non-invasive method to assess visual performance in healthy and visually impaired animals (Thaung et al., 2002). The OptoDrum (Striatech GmbH), an automated system for visual performance assessment in rodents, offers a significant improvement over manual methods by reducing potential human bias. In this study, OMR-based visual acuity measurement using the OptoDrum facilitated the evaluation of the potential therapeutic effects of AAV miRNA vectors in rd1 mice. My results showed that after P21 injections, non-injected sides outperformed the injected sides, suggesting that the procedure or the treatment had negative effects. The inclusion of a PBS-injection control group for the P1 injection time point revealed, that unlike the P21 group, the PBS-

injected mice did not perform better on the non-injected vs. the injected sides. This was an implication that the observed results might be treatment related in the P21 group. However, the results also showed a high variability in visual acuity measurements on the PBS-injected sides at P42, with some visual acuities unexpectedly close to those of healthy controls. Given that optomotor testing of rd1 mice at P30 in previous studies has shown a high degree of visual impairment (Narayan et al., 2019b), these results may reflect false-positive measurements, suggesting limitations in the automated system when assessing visual performance in visually impaired animals. This is why rigorous data examination should be considered to identify and exclude potential false positives and avoid misinterpretation. To draw definitive conclusions if the negative effects observed after treatment at P21 are caused by the treatment itself, injection control groups should be included for every injection time point in the future.

4.5 Potential limitations of the OptoDrum when analyzing visually impaired animals

In the OptoDrum trials, healthy non-visually impaired and visually impaired controls (rd1 mice) also served as an experimental reference. The healthy controls exhibited visual acuity measurements, aligning with reported literature values (Da Silva Souza et al., 2011). In contrast, rd1 mice showed markedly impaired vision compared to the healthy controls. However, my results indicated that some rd1 mice exhibited visual acuities approaching those of healthy controls at P42 and P60, a finding inconsistent with the reported progression of vision loss in this model (Narayan et al., 2019b), suggesting that these results might be again false positive measurements. Despite these concerns, the values were retained in the analysis due to the low animal number. The company released a software update in 2023, which was designed to address this issue and included improved measurements to reduce false positive outcomes. This demonstrated the company's awareness of and responsiveness to the issue. The initial measurement of a head movement triggered by a stimulus is now treated with greater caution. This involves presenting the stimulus one additional time before confirming that the animal's head movement has been triggered before the algorithm progresses to the next, more challenging stimulus. Despite this, some of the data from visually impaired animals were

analyzed with the previous software version, which is why the data should be interpreted critically. Future analyses should consider these limitations and the potential need for further software refinements by the company to ensure accurate assessments.

4.6 Technical challenges impact subretinal injection success and light aversion behavior in rd1 mice treated at P1

The P1 subretinal injection time point was selected in this study to assess the treatment effect before the onset of retinal degeneration. My results showed that animals treated with AAV-miR-124 exhibited improvement in light aversion behavior. This supported the findings from the light/dark box trials involving P21-injected animals, suggesting that the miR-124 may be a viable treatment option both in the later stages of disease progression and for the application prior to the onset of retinal degeneration. Furthermore, the miR-124 administration appears effective regardless of the retina's developmental stage, since the miRNAs were also applied before retinal development was finished (Mu et al., 2001). To fully evaluate the potential of miR-124, further studies with larger cohorts at the P1 injection time point are necessary, especially given the low success rate of P1 injections compared to the P21 injections. It is important to note that P1 injections were started after the successful completion of the P21 subretinal injections. Initially, the goal of the study was to administer the miRNAs exclusively at P21. After consulting with numerous scientists at the ARVO 2023 Annual Meeting, it was decided to include the P1 injection time point due to the highly degenerative nature of the rd1 mouse model. Including the P1 injection enabled a dual investigation: it allowed to study the neuroprotective effects in degenerating retinas, while also providing a more detailed examination of the roles of miR-124, miR-182, and miR-183 on cone survival when expressed during retinal development in degenerative models, as they take over crucial functions during development in healthy mouse retinas (Sanuki et al., 2011; Busskamp et al., 2014a). Accordingly, an amendment request was submitted to the relevant authorities. Unfortunately, this led to a reduction in the number of training animals, as some had already been used for practicing the P21 injections. Training for P1 injections was crucial due to significant technical differences between the P21 and P1 subretinal injection procedures. A total of five neonatal mice were used for surgical training before the experimental groups were initiated. Given that

even highly trained surgeons have an average success rate of only 27 % in their initial 50 cases of murine subretinal injections (Huang et al., 2022), it is reasonable to conclude that the lack of sufficient surgical training contributed to the low success rate and a limited number of successfully injected animals included in the final assessment of the treatment's efficacy. It is important to highlight, that in recent years, regulations governing animal research have become more stringent, making it increasingly difficult to request additional animals for studies which also requires a significant administrative and bureaucratic effort.

In contrast, only one animal in the AAV-miR-182/183 treatment group was successfully treated at P1 and therefore included in the final treatment efficacy assessment. This animal did not show any improvement in light aversion behavior. Since definitive conclusions cannot be drawn from a single case, further studies are needed to determine the impact of miR-182/183 on treatment efficacy. However, it is important to note that the accumulation of miR-182/96/183 cluster early in development negatively affected retinal layer morphology (Krol et al., 2015). Therefore, and adjustment of the injection time point after retinal development may be advisable. An injection time between P8 and P11 could enhance the treatment outcomes, as retinal development is complete by this stage (Mu et al., 2001). The P8 injection time point has also been used in other studies that aimed at rescuing retinal degeneration in rd1 mice (A et al., 2019). In conclusion, miR-182/183 treatment may need to be carefully timed according to the developmental status of the retina to improve efficacy.

The small sample size again precluded conclusions about statistically significant results despite visible positive treatment effects after treatment at P1, leading to potential misinterpretation of a relevant treatment that should be subjected to further investigation. It is notable, that the issue of reduced sample size has been highlighted in numerous studies that have critically examined the reliability of results in animal research when sample sizes are small, as well as the ethical concerns associated with increasing sample sizes. This has led to the development of models that increase the power of the results while using the minimum number of animals (Bonapersona et al., 2021). However, the use of the minimum number of animals in animal studies remains a challenging issue, ultimately leading to a lack of statistical power (Vasbinder and Locke, 2016). In conclusion,

all the observations provide a sound foundation for further research into the impact of miRNAs on the improvement of light aversion behavior. Expanding the cohort size by including additional animals is of great importance to enhance the statistical significance of the results, particularly also considering the post-surgery complications in the P21 group. This objective may be accomplished through the submission of a follow-up application or a request for authorization to utilize additional rd1 mice. Nevertheless, the rd1 model should still be subjected to critical analysis, as it is a highly degenerative model. The substantial and accelerated loss of photoreceptors has been shown to limit the scope of potential therapeutic intervention, making this model somewhat suboptimal for this study (Pennesi et al., 2012). Given the potential beneficial effects of the respective miRNAs on improved light aversion behavior, it may be advantageous to use different mouse models of retinal degeneration. Mouse models with pronounced cone degeneration could be used, such as the cone photoreceptor function loss 9 (cpfl9) mice, which are characterized by an early loss of cone and rod photoreceptor function followed by a progressive loss of cone and rod photoreceptors in later stages (Naggert et al., 2022; Chang et al., 2002). This may facilitate the observation of enhanced outcomes associated with this cone-focused approach. The rd10 mouse may also be a suitable subject for future treatment trials. Here, rod degeneration begins only between P16 and P20 and peaks between P21 and P25 (Chang et al., 2007). Since photoreceptor degeneration is much slower in this model, a later onset of photoreceptor degeneration expands the scope of potential therapeutic intervention and likely provides a better basis for investigating the potential of the treatment. It is also important to emphasize that most of the cones completely lose their OS by P25 and are highly degenerated by P28 in the rd1 mouse model (Lin et al., 2009; Punzo and Cepko, 2007). Since the AAV vector DNA is single-stranded and requires second-strand synthesis (Hauck et al., 2004), treatment at P21 may prove insufficient to counteract the effects of cone degeneration, as the transgene reaches its expression plateau approximately 4 to 6 weeks after the gene transfer to the cell. It is therefore expressed at a time when cone death is already highly advanced. In general, it would be advantageous to increase the number of animals injected at an earlier time point to ensure that vector expression is at a stable level prior to cone OS loss. The use of self-complementary AAVs can circumvent the need for second-strand synthesis (Buie et al., 2010) but could not be used in the present study due to their limited cargo size of 2.4 kb

(Casey et al., 2020). The present study still provides a good rationale to request more animals in a follow-up animal permit for future experiments. Nevertheless, from an ethical standpoint, the inclusion of regulations that improve animal welfare is undoubtedly a crucial aspect. This underscores the importance on the improvement of alternative models, such as advanced human *in vitro* systems like hROs, to complement or replace animal studies, aligning with the 3Rs principle of Replacement, Reduction, and Refinement (Russell and Burch, 1992).

4.7 Typical rd1 retinal morphology after treatment with notable changes in a single treated animal

The observed retinal changes following rod loss in rd1 mice matched previously reported patterns of cone photoreceptor persistence and degeneration. Typically cones exhibit prolonged survival after rod degeneration, as confirmed by my study and earlier research (Carter-Dawson et al., 1978). In all treatment groups, regardless of whether the treatment occurred at P1 or P21, the OS were retracted, and the ONL was notably thinned in most animals, aligning with a typical rd1 retinal morphology at this stage (Pennesi et al., 2012; Lin et al., 2009; Narayan et al., 2019a). Notably, the P1 cohort treated with AAV-miR-124 exhibited neurite sprouting from cones to cells in the INL layer. This finding was consistent with reports of cones extending their neurites around P20, to form ectopic connections with rod bipolar cells in the INL in degenerating retinas (Haq et al., 2014; Marc et al., 2003). Such synaptic rewiring reflects a compensatory mechanism in response to rod death and underscores the synaptic plasticity of cone PRs in this model (Peng et al., 2000).

Notably, the animal treated with AAV-miR-124 at P1, which showed improved visual performance, also had better preservation of the ONL. The injected retina showed multiple layers of cones at P60, in contrast to the single layer cone arrangement seen in the non-injected sides. The non-injected side of this animal again reflected the typical morphology at this stage of disease progression. This suggests that AAV-miR-124 treatment may have enhanced cone photoreceptor survival through a neuroprotective effect, which may also have induced anti-apoptotic effects, helping to maintain retinal structure in a highly

degenerative environment. However, a substantial number of eGFP+ cells in the ONL did not colocalize with ARR3, which may indicate downregulation of cone-specific genes, as it was reported for the blue opsin (Punzo and Cepko, 2007). This led to the hypothesis that while AAV-miR-124 treatment may have slowed the progression of cone degeneration in one animal, it may not completely prevent the molecular changes associated with retinal degeneration.

In contrast, the animal treated with AAV-miR-182/183 at P1 showed complete loss of the ONL by P60. The structural analysis supports the earlier finding that the accumulation of miR-182 and miR-183 during early retinal development may have adversely affected retinal layer morphology (Krol et al., 2015). The limited success in preserving retinal morphology following P1 and P21 injections highlights the challenges of therapeutic intervention in such highly degenerative models which again emphasized the need of using different mouse models with a slower retinal degeneration characteristic.

4.8 Positive treatment outcome after P1 injection may correlate with increased retinal transduction rate

One animal showed improvement of light aversion behavior as well as improvement of visual acuity on the injected side after AAV-miR-124 treatment at P1. This animal was the only one in the P1 injection group that showed improvement in visual acuity and exhibited the most extensive viral spread throughout the retina compared to the other two animals. This led to the hypothesis that the positive treatment outcome may be related to an enhanced cone cell tropism. Given the overall effect on visual improvement in this animal, additional animals should be treated with the goal to achieve similar extensive eGFP signals throughout the retina to further validate miR-124 as a viable treatment option.

In contrast, the P21-treated animals all showed widespread eGFP signals throughout the retina, but no explant showed the intensity observed in the animal with improved visual performance. Because a different viral batch was used for the P21 injections, decreased tropism may be due to inferior viral batch quality. Poor quality can result from the presence of empty capsids or capsids containing DNA other than the AAV vector genome, which

reduces transduction efficiency (Schnödt and Büning, 2017). Poor cone tropism is a significant drawback especially for this cone focused approach. It is also important to highlight, that a cone-focused approach in mouse models have inherent limitations since mice have a rod dominant retina (Jeon et al., 1998), which underscores the need for improved model systems for studying cone function. For a better assessment of AAV transduction rates in the future, retinal whole-mount preparations should be used as they contain the whole area of transduction (Nieuwenhuis et al., 2023; Busskamp et al., 2010). This approach was not feasible in the present study due to the limited number of animals and the focus on structural analysis requiring retinal sectioning. Although live imaging of *ex vivo* retinal explants provided some insights into transduction effectiveness, a more detailed *in vivo* analysis of eGFP signals using techniques such as scanning laser ophthalmoscopy (SLO) could be beneficial for assessing eGFP signals *in vivo*. SLO is a non-invasive imaging technique that enables single-cell fluorescence in the retina and could provide valuable information on the transduction efficiency and the spread across the retina (Williams, 2011).

In one animal successfully treated with AAV-miR-124, visual acuity on the non-injected side improved over time compared to the injected side. A similar phenomenon has been reported with gene therapy, where monocular treatments led to improvement in both eyes (Yu-Wai-Man et al., 2020). This was explained by an unexpected transfer of viral vector DNA from the injection side to the non-injected side. In the present study, no eGFP signals were observed on the non-injected sides, ruling out the possibility of the same phenomenon. In addition, there was no improvement in visual acuity on the injected side in this animal. In summary, it is reasonable to conclude that treatment did not result in improvement of spatial vision in most cases, except for one case in this highly degenerative model, regardless of the time point of retinal development at which treatment was applied.

4.9 eGFP signals detectable in INL and the GCL in retinal sections following injection at P1

In addition to the eGFP signals observed in cones located in the ONL, signals were also detected in the INL, which may be related to remodeling processes in the degenerating retina of rd1 mice, including migration of cones to other retinal layers, as described previously (Kalloniatis et al., 2016; Cuenca et al., 2014; Marc et al., 2003). Besides migrating cones, these eGFP+ cells in the INL could be BCs. Future studies should incorporate cell-specific antibodies, such as Protein Kinase C - alpha (PKCα), to confirm this (Ruether et al., 2010). The eGFP+ cells that were observed in the GCL might be RGCs. To specifically label RGCs, antibodies against brain-specific homeobox/POU domain protein 3A (BRN3A) could be incorporated into the immunostaining procedure of future studies (Nadal-Nicolás et al., 2023). The ectopic expression in non-photoreceptor cell types could also be related to off-target transgene expression due to the promoter used, as previous research has documented similar off-target effects with the human cone arrestin (hCAR) and the mCAR promoter (McDougald et al., 2019; Dyka et al., 2014). It is also possible that off-target expression results from transduction of other retinal cell types, as has been demonstrated for the AAV2.NN serotype (Xia and Guo, 2023). Typically, photoreceptor-specific promoters are used to address this issue, resulting in more specific transgene expression in photoreceptors (Dalkara et al., 2013). However, my results suggest that this might not be the case for the mCAR promoter when used in the combination with the AAV2.NN serotype. Therefore, antibodies to counterstain other cell types in the retina is essential for future experiments to identify potential ectopic expression. Furthermore, alternative cone-specific promoters could be considered for future studies to enhance specificity.

4.10 AAV-miR-183 shows higher transduction rate of hROs

There is an urgent need for alternative rodent models to study retinal degenerative diseases, especially since rodents lack a macula and have a different composition of photoreceptors in the retina, making them an imperfect model for studying diseases in which cone loss in the central parts of the retina is the primary cause of blindness, such

as AMD (Volland et al., 2015). Cone-related studies are inherently complex to study in mice because cones make up an average of 2.8 % of all photoreceptors in the retina (Jeon et al., 1998). Therefore, hROs serve as a valuable research tool, providing insight into the distinct functions of different cell types. It has been demonstrated that hROs recapitulate the five layered structure of the human retina, establish functional synapses and similar transcriptomic characteristics to the human peripheral retina (Cowan et al., 2020). The AMASS protocol that was used to grow hROs in my study allowed to produce hROs in large quantities, thus overcoming the tissue limitations encountered in animal studies. The AAV2.NN serotype has been shown to efficiently transduce photoreceptors in hROs (Völkner et al., 2021). However, because the previous study used a different protocol and cell line to generate hROs, I evaluated transduction efficiency in hROs that were generated using the AMASS protocol (Cowan et al., 2020). My results confirmed successful transduction of W19 old hRO with AAVs encoding miR-182, miR-183, and eGFP under the mCAR promoter. These results demonstrate that the AAV2.NN serotype efficiently transduces cone photoreceptors, even across different hRO protocols and cell lines. However, the reduced transduction efficiency of AAV-miR-182 suggests that the viral batch may have been of inferior quality, as discussed earlier. Improving the quality of this viral batch should be considered for future experiments. Since this viral batch was also used for the P1 injections in the mice, it seems likely that the different eGFP signals observed in the *ex vivo* retinal explants were due to a compromised viral batch. Nevertheless, the AAV2.NN serotype appears to be effective in transducing hROs generated by alternative protocols.

4.11 miR-183 supplementation enhances cone photoreceptor protrusion length in developing hROs

In addition to studying miRNA expression when expressed at later stages of hRO development using AAV, I generated hROs using a transgenic cell line expressing miR-183 under the mCAR promoter. The aim was to investigate the effect of miR-183 during hRO development. It was hypothesized that miR-183 supplementation could potentially enhance cone maturation, based on previously reported effects of miR-183 on cone maturation and retinal function *in vivo* and the positive impact of the miR-182/96/183

cluster in promoting the outgrowth of photosensitive OS in mESC-derived retinal organoids (Zhang et al., 2020; Busskamp et al., 2014a). To modify the default hiPSC line for growing hROs, I employed the PB transposon system, which operates through DNA transposons (Woodward and Wilson, 2015).

The eGFP reporter gene placed downstream of miR-183 allowed expression to be monitored by live fluorescence imaging at regular intervals throughout the hRO culture period to confirm expression indicative of mCAR promoter activity. However, the eGFP signals were weak, consistent with the compromised live eGFP signal strength in the AAV-transduced organoids. This was attributed to the low resolution and a low signal-to-noise ratio, which are known to hinder accurate analysis of fluorescent signals in 3D tissue (Engelbrecht et al., 2022). Therefore, hROs were isolated and fixed at various developmental stages for immunohistochemical analysis using confocal microscopy. This technique confirmed the successful expression, as evidenced by the eGFP signals in W30 hROs. In addition to eGFP counterstaining, cone-specific staining using ARR3 and L/M opsin markers, showed that cones in miR-183-modified hROs exhibited a more developed morphology, characterized by elongated shapes and protrusions that appeared more extended compared to WT organoids. L/M opsin staining visualized a cone protrusion, although the signal was mislocalized to cytoplasmic regions. This was an indication that the cone protrusion was likely not fully developed at this stage and that some opsin proteins remained in the cytoplasm where they are synthesized, rather than being fully transported to the cone protrusion. Notably, no other cones showed this type of staining, and the staining was absent in WT organoids. These observations reinforced the hypothesis that this cone photoreceptor was likely more developed and already expressed opsin proteins. While confocal microscopy was effective for visualizing cone protrusions, it did not provide clear evidence on the presence of disc membranes at W30, which would indicate a higher level of cone maturation (Spencer et al., 2020). To gain further insight into protrusion structure, employing transmission electron microscopy (TEM) would be beneficial for future experiments (Graham and Orenstein, 2007). TEM could resolve the ultrastructural morphology of cone OS in both WT and the miR-183- modified hROs, facilitating the evaluation of potential signs of accelerated maturation as demonstrated in previous studies (Busskamp et al., 2014a). In conclusion, miR-183 may have positively

influenced cone maturation in growing hROs, consistent with previously reported effects, although further investigation is needed to explore the full potential.

The W35 hROs harvested for immunostaining, as well as earlier time points, did not show eGFP signals, suggesting the potential presence of hROs lacking the miRNA expression cassette. The lack of eGFP signals prevented the quantification of protrusion lengths in these organoids, which hindered the analysis of miR-183 effects at earlier and later time points. In this context it is important to note that the transposon copy number can vary significantly depending on the size of the PB transposon plasmid. Smaller vectors have generally been shown to achieve higher copy numbers per cell compared to larger vectors (Nakazawa et al., 2013). Given the substantial size of the expression cassette (over 9 kb), it is plausible that copy numbers were low, possibly resulting in the absence of eGFP signals in some hROs. In future experiments, the integrant copy number could be further adjusted and improved by modifying the ratios between the transposon (gene of interest) and the transposase, which might enhance the integration rate into the host genome. To evaluate potential improvements in transposon integration, copy number determination using RT-qPCR could be implemented. To this end, the genomic copy numbers of the Puro resistance gene, which is part of the PB transposon vector, is compared against the ribonuclease P RNA component H1 (*RPPH1*) reference gene. *RPPH1* is a well-known and a commonly used reference gene, typically present in two copies per diploid genome (Weaver et al., 2010; Baer et al., 1990). It was further hypothesized that the silencing or repression of transposable elements (TEs) by intrinsic mechanisms, might explain the differential effects observed among different organoids, considering that each hRO is a self-organizing tissue (Bourque et al., 2018; Eiraku et al., 2011). Epigenetic silencing of promoters may also have caused transcriptional silencing, resulting in lower levels of *eGFP* throughout hRO development. Epigenetic modification is essential for tissue differentiation and can influence gene expression during development (Newell-Price et al., 2000; Lim et al., 2019). Changing the promoter could potentially address the unexpected changes in gene expression. In general, the PB system offers advantages over viral delivery systems, allowing the introduction of large vectors, and demonstrated long-term expression over a thirty-week period in the hROs in my study (Kim and Pyykko, 2011). Nevertheless, the use of LV systems as a gene delivery tool might be beneficial to achieve

more homogeneous and stable expression across different hROs (Hu et al., 2024). The use of AAVs could also be further explored in future studies, as my results showed that gene delivery by AAVs to hROs is feasible and effective. Further optimization and longer culture periods after AAV transduction should be tested for more controlled gene expression.

A comparative analysis of the transcriptomes of the cells that are present in hROs and those of adult human retinal cell types derived from post-mortem retinal tissues revealed that hROs exhibit a closer resemblance to the cell compositions of the peripheral retina (Cowan et al., 2020). This means that the hROs comprise a combination of cones and rods, as the number of cones decreases from the foveal region, which is composed solely of cones, to the periphery of the retina, which contains a combination of rod and cone cells (Kolb et al., 1995; Farber et al., 1985). Protocols that generate hROs with a higher quantity of cones could be tested in the future to assess whether they produce more pronounced effects with this cone focused approach (Kim et al., 2019). Despite this, the number of cones present in the organoids was sufficient to evaluate a first idea of the impact of miR-183 on the accelerated development of cones. This provides a foundation for future experiments to further investigate the effects miR-183. Given the potential beneficial effects of miR-183, it would be valuable to test miR-183 modifications in patient-derived hiPSCs affected by IRDs and generate hROs. This approach may facilitate the study of miR-183 effects in disease models *in vitro*. The use of patient-derived hiPSCs for disease modeling has already proven successful in other hROs studies (Kallman et al., 2020; Mayerl et al., 2022) suggesting that this approach could provide further insights into the therapeutic potential of miR-183 in an *in vitro* human model of IRDs. However, this requires a comprehensive optimization process, as the original development of this protocol involved evaluating a wide range of cell lines, some of which failed to form high-quality hROs and did not meet the criteria for this specific protocol (Cowan et al., 2020).

4.12 Temporal increase of miR-183 and eGFP expression in miR-183 modified hROs

Analysis of transcriptomic levels of miR-183 and *eGFP* was used to validate the activity of the miRNA expression cassette, in addition to quantification of cone protrusion length as a hallmark of cone maturation. To this end, bulk RT-qPCR was employed to facilitate a comparison of the transcriptomic differences in expression levels of miR-183 in WT and the modified hROs. Furthermore, the transcriptomic levels of *eGFP* were determined in the miR-183-modified hROs. This required the dissection of the retinal regions prior to the RNA isolation procedure. This method ensured that the isolated RNA transcripts originated from retinal cells and were not derived from non-retinal cells that were also present in the hROs. In addition, the efficiency of hRO formation is approximately 80 %, with 20 % of the organoids failing to develop into retinal organoids (Cowan et al., 2020). Therefore, dissection of the retinal parts also allowed the elimination of non-retinal organoids, which could potentially decrease the detection of miR-183 and *eGFP* due to the higher abundance and diversity of alternative transcripts in these samples (Levesque-Sergerie et al., 2007).

The transcriptomic levels of miR-183 in miR-183-modified hROs showed a significant increase from W24 to W30. However, it was evident that miR-183 expression levels were also increased from W24 to W30 in the WT organoids. This was consistent with previously reported transcriptomic levels of miRNAs in hROs, where photoreceptor-specific miRNAs showed increased expression over time in hROs, including miR-183 (Celiker et al., 2023). This underscores that hROs are suitable *in vitro* model systems for miRNA studies, as miRNAs present in the developing retina can also be detected in developing hROs. It is important to note that the expression levels were first normalized to the W24 time point within each experimental group, making it difficult to draw direct conclusions regarding whether miR-183 expression levels were indeed higher in the modified hRO group. Accordingly, the transcriptomic data for miR-183 in WT and miR-183-modified organoids at W30 were normalized to a common reference point, namely the W24 time point for WT organoids. This demonstrated that the miR-183 expression in the modified organoids was significantly higher in comparison to the WT organoid group at W30. This led to the

assumption that the miR-183 had been successfully supplemented in the miR-183-modified organoids, which suggested that the miR-183 supplementation had biologically relevant effects, supporting greater protrusion length. Nevertheless, miR-183 expression showed a decrease at W35 in both groups. A possible explanation for this observation is that hROs become more complex at later stages due to the presence of late-born rod photoreceptor cells (Cowan et al., 2020). This may have led to the dilution effects on miR-183 transcripts caused by increased levels of other transcripts. Moreover, increased biological variability and complexity can reduce transcript detection, introducing errors into RT-qPCR experiments and negatively impacting the reproducibility of results (Taylor et al., 2019).

It is also important to exercise caution when interpreting the results of miR-183 transcriptome levels, as changes in miR-183 expression levels may be influenced by light exposure. Previous research has shown that the miR-182/96/183 cluster is upregulated in the retina in response to light exposure, as well as after exposure to specific wavelengths of light in hROs (Krol et al., 2010a; Celiker et al., 2023). As this factor was not previously considered prior to the dissection of the retinal parts of hROs, future studies on miR-183-modified hROs should incorporate light or dark adaptation prior to the dissection procedure of the hROs to prevent potential misinterpretation of the transcriptomic data.

The transcriptomic analysis of *eGFP* expression levels revealed a gradual increase from W24 to W35 in the miR-183-modified hROs, providing further evidence for the long-term activity of the PB expression cassette over a period exceeding thirty weeks. This was in contrast to the observations regarding miR-183 expression, as miR-183 expression was decreased at W35, reinforcing the notion that light-regulated up- and downregulation or internal regulatory mechanisms influenced miR-183 expression. However, the *eGFP* levels were generally observed to be expressed at lower levels. This finding was consistent with the previous observations of the live eGFP signals. Since eGFP signals were not detectable during live imaging, it is also likely that dissected retinal parts of hROs that were not eGFP+ were included, resulting in a dilution effect on the detection of transcriptomic levels of *eGFP.* These limitations, along with technical difficulties that can

arise make bulk RT-qPCR an imperfect tool for drawing definitive conclusions about transcriptomic changes (Taylor et al., 2019). In the future, adaptations to RNA isolation protocols may also prove beneficial in improving the efficacy of bulk RT-qPCR. The RNA isolation from three-dimensional tissues used in my study was comparable to the methodology used for two-dimensional systems, with some additional steps to improve tissue lysis. It has been reported that protocols established for 2D systems may require adjustments when applied to 3D systems to ensure sufficient RNA isolation (Gysens et al., 2023). This scientific paper also presents a protocol for direct lysis of 3D cultures, which could be implemented in future experiments. It would still be advisable to dissociate the tissues and sort the eGFP+ cones via fluorescent-activated cell sorting (FACS) in the future, to isolate the RNA from eGFP+ cells only (Macaulay and Voet, 2014). This may help to reduce data variability in these highly heterogeneous and complex tissues and lead to more pronounced effects. This could also facilitate the analysis of potential differential expression of miR-183 target genes, such as *PAX6*, over the time course of hRO development, as the miR-182/96/183 cluster has been implicated as an important morphogenic factor in hROs by targeting *PAX6* (Peskova et al., 2020)

4.13 Conclusions and Outlook

The aim of my project was to investigate the potential therapeutic applications of miR-182 and miR-183 as well as miR-124 in mouse models of RP to prevent blindness. The goal was to develop a therapeutic approach that is independent of the underlying mutation and has the potential to protect against cone degeneration in other IRDs and potentially also in acquired forms of retinal degeneration such as AMD. To this end, subretinal injections were administered to rd1 mice at varying disease stages, with the objective of fully exploiting their potential as a neuroprotective therapeutic tool. The neuron-specific miR-124 was identified as a potential treatment option for improving light aversion behavior, irrespective of the developmental stage of the retina or the stage of the disease. My results also showed that miR-182 and miR-183 treatment is unlikely to be independent of the retinal developmental stage and showed a tendency to improve light aversion behavior only when administered at late stages of the disease. However, the treatments did not result in an improvement in spatial vision in most cases.

The beneficial effect on overall visual performance was observed to correlate with the efficacy of viral spread across the retina and, therefore, cone photoreceptor tropism. At this time, it is unclear whether the miRNAs have the potential to be considered as a potential therapeutic agent to prevent cone degeneration. Nevertheless, the project established a robust foundation for further investigation in the future. To increase the statistical power of the study, a larger number of animals should be included in future experiments, especially considering the complications that occurred after surgery, which were likely caused by the anesthetic compounds. Therefore, it seems reasonable to explore the potential benefits of modifying the anesthetic compound to avoid the complications that may be associated with the current anesthetic agent. However, a primary objective should be the modification of the injection time point, particularly regarding the miR-182/183 treatment. As noted above, the efficacy of this treatment may depend on the developmental stage of the retina, as deleterious effects on the development of retinal structure have been reported after forced expression of the cluster (Krol et al., 2015). In addition, the miRNA cluster is typically expressed at lower levels during the early stages of retinal development, highlighting the need for a different injection time point (Xu et al., 2007). Considerable inter-animal variability in virus spread was observed, with some retinal explants showing minimal spread throughout the retina, suggesting that low tropism may have contributed to the lack of treatment response in some animals. This again highlights the need for larger sample sizes in future studies to achieve improved viral transduction rates to further test the hypothesis that transduction efficiency correlates with treatment response. Another goal will be to use alternative mouse models with a slower degeneration profile, which may allow for more pronounced effects due to an extended range of therapeutic intervention. The behavioral studies will also be complemented by functional studies, such as multi-electrode array (MEA) retinal recordings of treated retinal explants (Meister et al., 1994), as this method could provide valuable information on the preserved light sensitivity of cone photoreceptors after treatment, since the functionality of the retinal circuitry relies on the presence of cone OS for generating light-evoked action potentials in RGCs.

My study also aimed to accelerate cone photoreceptor development in growing hROs to obtain mature photoreceptors at earlier stages of hRO development. The increased cone

protrusion length resulting from miR-183 expression was substantiated in this study, providing a solid basis for future investigations. The observation that RGCs degenerate before photoreceptor development is complete (Cowan et al., 2020) highlights the importance to accelerate PR development in hROs to ensure the RGCs are still present at a stage where PRs are present in the tissues. This would facilitate more advanced functional studies, such as those involving MEA recordings (Hallam et al., 2018). As MEA recordings were not feasible within the scope of this project, the future objective is to place the miR-183-modified hROs on MEA chips to ascertain whether these organoids exhibit light responsiveness at earlier time points. Functional recordings are critical for disease modeling, especially for retinal degenerative diseases that affect photoreceptors, as these conditions require intact retinal circuitry to mimic the pathological state. Another functional approach to be explored in future studies is the utilization of patch-clamp recordings of cone photoreceptors, as previously reported in other studies (Li et al., 2021). This would necessitate the generation of more robust live eGFP signals in cone photoreceptors, which remained a significant challenge when the PB system and the mCAR promoter was utilized. Given the hypothesis that epigenetic silencing of promoters or silencing of TEs caused low live eGFP signals, the aim would be to replace the mCAR promoter by other cone-specific promoters or to utilize other gene delivery systems, such as LV systems, to gain better control over the number of transgene copies present in the cells (Hu et al., 2024). The use of AAV as a gene delivery tool in hROs will be further explored in the future and may also help to achieve more stable transgene expression, as was successfully demonstrated in this study. In addition, TEM studies can provide a more comprehensive analysis of cone ultrastructure.

In summary, the study of miRNA function can be challenging, particularly in the context of ophthalmic research. The inherently dynamic nature of miRNAs makes accurate analysis of their effects a challenging task. It is important to note that I have used a variety of independent methods to investigate their potential to counteract retinal degeneration. Future studies will focus on implementing different mouse models of retinal degeneration, increasing the number of animals to improve statistical power, and adjusting injection time points to improve therapeutic effects to fully realize the potential of these miRNAs to potentially prevent blindness in the future. The use of a specific gene delivery system and

the possible modification of the promoter to enhance transgene expression are the main goals for future studies on hROs. Functional studies and ultrastructural analysis of cone photoreceptors will provide valuable insights to support the hypothesis that miR-183 plays an important role in accelerating the cone maturation process.

5 Abstract

Inherited retinal diseases (IRDs) and age-related macular degeneration (AMD) are characterized by the loss of photoreceptors, the sensory neurons in the retina, leading to severe vision loss. Retinitis pigmentosa (RP), the most common IRD, involves mutations in more than 80 known genes, while AMD affects older individuals and is associated with both genetic and environmental risk factors. Central vision loss, primarily caused by cone degeneration in the central parts of the retina, severely impacts quality of life due to loss of high acuity vision. Given the complexity of genetic and non-genetic factors involved in disease development, gene therapy approaches are often impractical, highlighting the need for gene-independent therapeutic approaches.

This study investigated the neuroprotective role of specific neuronal microRNAs (miRNA), miR-124, miR-182 and miR-183, on cone photoreceptors in the retinal degeneration mouse 1 (rd1) model of RP, as a gene-independent approach. In addition, the potential of miR-183 to accelerate cone photoreceptor development was investigated using stem cell-derived human retinal organoids (hRO). The goal was to enhance cone maturation to overcome the time-delayed development of photoreceptors and retinal ganglion cells (RGCs) that currently limits advanced functional analysis.

Subretinal injections of adeno-associated viral (AAV) vectors encoding miR-124, miR-182 and miR-183 were performed at different stages of disease and retinal development in rd1 mice. miR-124 demonstrated promising effects, resulting in trends toward improved light-aversion behavior after treatment, regardless of disease or retinal developmental stage. miR-182 and miR-183 treatment also resulted in trends toward improved light aversion behavior after treatment, although their efficacy seemed to depend on retinal developmental stage. In hROs, miR-183 significantly increased cone protrusion lengths, demonstrating its potential to enhance cone photoreceptor development in growing hROs.

These findings highlight the therapeutic potential of miRNAs in both *in vivo* and *in vitro* models and suggest further exploration of their role in neuroprotection and cone photoreceptor development.

6 List of figures

7 List of tables

8 References

A L, Zou T, He J, Chen X, Sun D, Fan X, Xu H. Rescue of Retinal Degeneration in rd1 Mice by Intravitreally Injected Metformin. Frontiers in molecular neuroscience 2019; 12: 102

Abdeljalil J, Hamid M, Abdel-Mouttalib O, Stéphane R, Raymond R, Johan A, José S, Pierre C, Serge P. The optomotor response: a robust first-line visual screening method for mice. Vision research 2005; 45: 1439–1446

Acland GM, Aguirre GD, Ray J, Zhang Q, Aleman TS, Cideciyan AV, Pearce-Kelling SE, Anand V, Zeng Y, Maguire AM, Jacobson SG, Hauswirth WW, Bennett J. Gene therapy restores vision in a canine model of childhood blindness. Nature genetics 2001; 28: 92–95

Agarwal V, Bell GW, Nam J-W, Bartel DP. Predicting effective microRNA target sites in mammalian mRNAs. eLife 2015; 4

Altuvia Y, Landgraf P, Lithwick G, Elefant N, Pfeffer S, Aravin A, Brownstein MJ, Tuschl T, Margalit H. Clustering and conservation patterns of human microRNAs. Nucleic acids research 2005; 33: 2697–2706

Anand V, Duffy B, Yang Z, Dejneka NS, Maguire AM, Bennett J. A deviant immune response to viral proteins and transgene product is generated on subretinal administration of adenovirus and adeno-associated virus. Molecular therapy: the journal of the American Society of Gene Therapy 2002; 5: 125–132

Applebury ML, Antoch MP, Baxter LC, Chun LL, Falk JD, Farhangfar F, Kage K, Krzystolik MG, Lyass LA, Robbins JT. The murine cone photoreceptor: a single cone type expresses both S and M opsins with retinal spatial patterning. Neuron 2000; 27: 513–523

Auricchio A, Hildinger M, O'Connor E, Gao GP, Wilson JM. Isolation of highly infectious and pure adeno-associated virus type 2 vectors with a single-step gravity-flow column. Human gene therapy 2001a; 12: 71–76

Auricchio A, Kobinger G, Anand V, Hildinger M, O'Connor E, Maguire AM, Wilson JM, Bennett J. Exchange of surface proteins impacts on viral vector cellular specificity and transduction characteristics: the retina as a model. Human molecular genetics 2001b; 10: 3075–3081

Ayton LN, Guymer RH, Luu CD. Choroidal thickness profiles in retinitis pigmentosa. Clinical & experimental ophthalmology 2013; 41: 396–403

B Domènech E, Marfany G. The Relevance of Oxidative Stress in the Pathogenesis and Therapy of Retinal Dystrophies. Antioxidants (Basel, Switzerland) 2020; 9

Baehr W, Wu SM, Bird AC, Palczewski K. The retinoid cycle and retina disease. Vision research 2003; 43: 2957–2958

Baer M, Nilsen TW, Costigan C, Altman S. Structure and transcription of a human gene for H1 RNA, the RNA component of human RNase P. Nucleic acids research 1990; 18: 97–103

Bakri SJ, Bektas M, Sharp D, Luo R, Sarda SP, Khan S. Geographic atrophy: Mechanism of disease, pathophysiology, and role of the complement system. Journal of managed care & specialty pharmacy 2023; 29: S2-S11

Bartel DP. MicroRNAs: genomics, biogenesis, mechanism, and function. Cell 2004; 116: 281–297

Bartel DP. MicroRNAs: target recognition and regulatory functions. Cell 2009; 136: 215–233

Ben-Yosef T. Inherited Retinal Diseases. International journal of molecular sciences 2022; 23

Bloomfield SA, Völgyi B. The diverse functional roles and regulation of neuronal gap junctions in the retina. Nature reviews. Neuroscience 2009; 10: 495–506

Bonapersona V, Hoijtink H, Sarabdjitsingh RA, Joëls M. Increasing the statistical power of animal experiments with historical control data. Nature neuroscience 2021; 24: 470–477

Bonezzi PJ, Tarchick MJ, Renna JM. Ex vivo electroretinograms made easy: performing ERGs using 3D printed components. The Journal of physiology 2020; 598: 4821–4842

Borchert GM, Lanier W, Davidson BL. RNA polymerase III transcribes human microRNAs. Nature structural & molecular biology 2006; 13: 1097–1101

Bourin M, Hascoët M. The mouse light/dark box test. European journal of pharmacology 2003; 463: 55–65

Bourque G, Burns KH, Gehring M, Gorbunova V, Seluanov A, Hammell M, Imbeault M, Izsvák Z, Levin HL, Macfarlan TS, Mager DL, Feschotte C. Ten things you should know about transposable elements. Genome biology 2018; 19: 199

Bowes C, Li T, Danciger M, Baxter LC, Applebury ML, Farber DB. Retinal degeneration in the rd mouse is caused by a defect in the beta subunit of rod cGMP-phosphodiesterase. Nature 1990; 347: 677–680

Boyd RF, Petersen-Jones SM. Techniques for subretinal injections in animals. Veterinary ophthalmology 2024

Bringmann A, Pannicke T, Grosche J, Francke M, Wiedemann P, Skatchkov SN, Osborne NN, Reichenbach A. Müller cells in the healthy and diseased retina. Progress in retinal and eye research 2006; 25: 397–424

Buie LK, Rasmussen CA, Porterfield EC, Ramgolam VS, Choi VW, Markovic-Plese S, Samulski RJ, Kaufman PL, Borrás T. Self-complementary AAV virus (scAAV) safe and long-term gene transfer in the trabecular meshwork of living rats and monkeys. Investigative ophthalmology & visual science 2010; 51: 236–248

Busskamp V, Duebel J, Balya D, Fradot M, Viney TJ, Siegert S, Groner AC, Cabuy E, Forster V, Seeliger M, Biel M, Humphries P, Paques M, Mohand-Said S, Trono D, Deisseroth K, Sahel JA, Picaud S, Roska B. Genetic reactivation of cone photoreceptors restores visual responses in retinitis pigmentosa. Science (New York, N.Y.) 2010; 329: 413–417

Busskamp V, Krol J, Nelidova D, Daum J, Szikra T, Tsuda B, Jüttner J, Farrow K, Scherf BG, Alvarez CPP, Genoud C, Sothilingam V, Tanimoto N, Stadler M, Seeliger M, Stoffel M, Filipowicz W, Roska B. miRNAs 182 and 183 are necessary to maintain adult cone photoreceptor outer segments and visual function. Neuron 2014a; 83: 586–600

Busskamp V, Lewis NE, Guye P, Ng AHM, Shipman SL, Byrne SM, Sanjana NE, Murn J, Li Y, Li S, Stadler M, Weiss R, Church GM. Rapid neurogenesis through transcriptional activation in human stem cells. Molecular systems biology 2014b; 10: 760

Bustin SA. Absolute quantification of mRNA using real-time reverse transcription polymerase chain reaction assays. Journal of molecular endocrinology 2000; 25: 169–193

Butryn A, Raza H, Rada H, Moraes I, Owens RJ, Orville AM. Molecular basis for GTP recognition by light-activated guanylate cyclase RhGC. The FEBS journal 2020; 287: 2797–2807

Calderone L, Grimes P, Shalev M. Acute reversible cataract induced by xylazine and by ketamine-xylazine anesthesia in rats and mice. Experimental eye research 1986; 42: 331–337

Campbell BC, Paez-Segala MG, Looger LL, Petsko GA, Liu CF. Chemically stable fluorescent proteins for advanced microscopy. Nature methods 2022; 19: 1612–1621

Campochiaro PA, Mir TA. The mechanism of cone cell death in Retinitis Pigmentosa. Progress in retinal and eye research 2018; 62: 24–37

Carter-Dawson LD, LaVail MM, Sidman RL. Differential effect of the rd mutation on rods and cones in the mouse retina. Investigative ophthalmology & visual science 1978; 17: 489–498

Casey G, Askew C, Brimble MA, Samulski RJ, Davidoff AM, Li C, Walters BJ. Self-complementarity in adeno-associated virus enhances transduction and gene expression in mouse cochlear tissues. PloS one 2020; 15: e0242599

Celiker C, Weissova K, Cerna KA, Oppelt J, Dorgau B, Gambin FM, Sebestikova J, Lako M, Sernagor E, Liskova P, Barta T. Light-responsive microRNA molecules in human retinal organoids are differentially regulated by distinct wavelengths of light. iScience 2023; 26: 107237

Chang B, Hawes NL, Hurd RE, Davisson MT, Nusinowitz S, Heckenlively JR. Retinal degeneration mutants in the mouse. Vision research 2002; 42: 517–525

Chang B, Hawes NL, Pardue MT, German AM, Hurd RE, Davisson MT, Nusinowitz S, Rengarajan K, Boyd AP, Sidney SS, Phillips MJ, Stewart RE, Chaudhury R, Nickerson JM, Heckenlively JR, Boatright JH. Two mouse retinal degenerations caused by missense mutations in the beta-subunit of rod cGMP phosphodiesterase gene. Vision research 2007; 47: 624–633

Chen Y, Tristan CA, Chen L, Jovanovic VM, Malley C, Chu P-H, Ryu S, Deng T, Ormanoglu P, Tao D, Fang Y, Slamecka J, Hong H, LeClair CA, Michael S, Austin CP, Simeonov A, Singeç I. A versatile polypharmacology platform promotes cytoprotection and viability of human pluripotent and differentiated cells. Nature methods 2021; 18: 528–541

Cheng L-L, Han R-Y, Yang F-Y, Yu X-P, Xu J-L, Min Q-J, Tian J, Ge X-L, Zheng S-S, Lin Y-W, Zheng Y-H, Qu J, Gu F. Novel mutations in PDE6B causing human retinitis pigmentosa. International journal of ophthalmology 2016; 9: 1094–1099

Chernykh VV, Varvarinsky EV, Smirnov EV, Chernykh DV, Trunov AN. Proliferative and inflammatory factors in the vitreous of patients with proliferative diabetic retinopathy. Indian journal of ophthalmology 2015; 63: 33–36

Chou C-H, Shrestha S, Yang C-D, Chang N-W, Lin Y-L, Liao K-W, Huang W-C, Sun T-H, Tu S-J, Lee W-H, Chiew M-Y, Tai C-S, Wei T-Y, Tsai T-R, Huang H-T, Wang C-Y, Wu H-Y, Ho S-Y, Chen P-R, Chuang C-H, Hsieh P-J, Wu Y-S, Chen W-L, Li M-J, Wu Y-C, Huang X-Y, Ng FL, Buddhakosai W, Huang P-C, Lan K-C, Huang C-Y, Weng S-L, Cheng Y-N, Liang C, Hsu W-L, Huang H-D. miRTarBase update 2018: a resource for experimentally validated microRNA-target interactions. Nucleic acids research 2018; 46: D296-D302

Chu-Tan JA, Cioanca AV, Feng Z-P, Wooff Y, Schumann U, Aggio-Bruce R, Patel H, Rutar M, Hannan K, Panov K, Provis J, Natoli R. Functional microRNA targetome undergoes degeneration-induced shift in the retina. Molecular neurodegeneration 2021; 16: 60

Chu-Tan JA, Natoli R. The potential for microRNA-based therapeutics in retinal disorders. Annals of translational medicine 2020; 8: 419

Chu-Tan JA, Rutar M, Saxena K, Aggio-Bruce R, Essex RW, Valter K, Jiao H, Fernando N, Wooff Y, Madigan MC, Provis J, Natoli R. MicroRNA-124 Dysregulation is Associated With Retinal Inflammation and Photoreceptor Death in the Degenerating Retina. Investigative ophthalmology & visual science 2018; 59: 4094–4105

Ciganda M, Williams N. Eukaryotic 5S rRNA biogenesis. Wiley interdisciplinary reviews. RNA 2011; 2: 523–533

Cowan CS, Renner M, Gennaro M de, Gross-Scherf B, Goldblum D, Hou Y, Munz M, Rodrigues TM, Krol J, Szikra T, Cuttat R, Waldt A, Papasaikas P, Diggelmann R, Patino-Alvarez CP, Galliker P, Spirig SE, Pavlinic D, Gerber-Hollbach N, Schuierer S, Srdanovic A, Balogh M, Panero R, Kusnyerik A, Szabo A, Stadler MB, Orgül S, Picelli S, Hasler PW, Hierlemann A, Scholl HPN, Roma G, Nigsch F, Roska B. Cell Types of the Human Retina and Its Organoids at Single-Cell Resolution. Cell 2020; 182: 1623-1640.e34

Cowey A, Franzini C. The retinal origin of uncrossed optic nerve fibres in rats and their role in visual discrimination. Experimental brain research 1979; 35: 443–455

Cuenca N, Fernández-Sánchez L, Campello L, Maneu V, La Villa P de, Lax P, Pinilla I. Cellular responses following retinal injuries and therapeutic approaches for neurodegenerative diseases. Progress in retinal and eye research 2014; 43: 17–75

Czarnek M, Sarad K, Karaś A, Kochan J, Bereta J. Non-targeting control for MISSION shRNA library silences SNRPD3 leading to cell death or permanent growth arrest. Molecular therapy. Nucleic acids 2021; 26: 711–731

Da Silva Souza G, Gomes BD, Silveira LCL. Comparative neurophysiology of spatial luminance contrast sensitivity. Psychology & Neuroscience 2011; 4: 29–48

Dalkara D, Byrne LC, Klimczak RR, Visel M, Yin L, Merigan WH, Flannery JG, Schaffer DV. In vivo-directed evolution of a new adeno-associated virus for therapeutic outer retinal gene delivery from the vitreous. Science translational medicine 2013; 5: 189ra76

Dambal S, Shah M, Mihelich B, Nonn L. The microRNA-183 cluster: the family that plays together stays together. Nucleic acids research 2015; 43: 7173–7188

DeVries SH, Baylor DA. Synaptic circuitry of the retina and olfactory bulb. Cell 1993; 72 Suppl: 139–149

Díaz-Lezama N, Kajtna J, Wu J, Ayten M, Koch SF. Microglial and macroglial dynamics in a model of retinitis pigmentosa. Vision research 2023; 210: 108268

Ding J-D, Salinas RY, Arshavsky VY. Discs of mammalian rod photoreceptors form through the membrane evagination mechanism. The Journal of cell biology 2015; 211: 495–502

Dong N, Xu B, Shi H, Tang X. Baicalein Inhibits Amadori-Glycated Albumin-Induced MCP-1 Expression in Retinal Ganglion Cells via a MicroRNA-124-Dependent Mechanism. Investigative ophthalmology & visual science 2015; 56: 5844–5853

Dräger UC, Hubel DH. Studies of visual function and its decay in mice with hereditary retinal degeneration. The Journal of comparative neurology 1978; 180(1): 85–114.

Duncan JL, Pierce EA, Laster AM, Daiger SP, Birch DG, Ash JD, Iannaccone A, Flannery JG, Sahel JA, Zack DJ, Zarbin MA. Inherited Retinal Degenerations: Current Landscape and Knowledge Gaps. Translational vision science & technology 2018; 7: 6

Dyka FM, Boye SL, Ryals RC, Chiodo VA, Boye SE, Hauswirth WW. Cone specific promoter for use in gene therapy of retinal degenerative diseases. Advances in experimental medicine and biology 2014; 801: 695–701

Ebert MS, Sharp PA. Roles for microRNAs in conferring robustness to biological processes. Cell 2012; 149: 515–524

Eiraku M, Takata N, Ishibashi H, Kawada M, Sakakura E, Okuda S, Sekiguchi K, Adachi T, Sasai Y. Self-organizing optic-cup morphogenesis in three-dimensional culture. Nature 2011; 472: 51–56

Engelbrecht L, Ollewagen T, Swardt D de. Advances in fluorescence microscopy can reveal important new aspects of tissue regeneration. Biochimie 2022; 196: 194–202

Evans JR, Lawrenson JG. Antioxidant vitamin and mineral supplements for preventing age-related macular degeneration. The Cochrane database of systematic reviews 2017; 7: CD000253

Fahim AT, Daiger SP, Weleber RG. Nonsyndromic Retinitis Pigmentosa Overview. In: Adam MP, Feldman J, Mirzaa GM, Pagon RA, Wallace SE, Bean LJH, Gripp KW, Amemiya A, editors. Seattle (WA): University of Washington, 1993

Farber DB, Flannery JG, Lolley RN, Bok D. Distribution patterns of photoreceptors, protein, and cyclic nucleotides in the human retina. Investigative ophthalmology & visual science 1985; 26: 1558–1568

Farber DB, Lolley RN. Cyclic guanosine monophosphate: elevation in degenerating photoreceptor cells of the C3H mouse retina. Science (New York, N.Y.) 1974; 186: 449–451

Felekkis K, Touvana E, Stefanou C, Deltas C. microRNAs: a newly described class of encoded molecules that play a role in health and disease. Hippokratia 2010; 14: 236–240

Fernando N, Wong JHC, Das S, Dietrich C, Aggio-Bruce R, Cioanca AV, Wooff Y, Chu-Tan JA, Schumann U, Ngo C, Essex RW, Dorian C, Robertson SA, Man SM, Provis J, Natoli R. MicroRNA-223 Regulates Retinal Function and Inflammation in the Healthy and Degenerating Retina. Frontiers in cell and developmental biology 2020; 8: 516

Fire A, Albertson D, Harrison SW, Moerman DG. Production of antisense RNA leads to effective and specific inhibition of gene expression in C. elegans muscle. Development (Cambridge, England) 1991; 113: 503–514

Fletcher EL, Jobling AI, Greferath U, Mills SA, Waugh M, Ho T, Iongh RU de, Phipps JA, Vessey KA. Studying age-related macular degeneration using animal models. Optometry and vision science: official publication of the American Academy of Optometry 2014; 91: 878–886

Ganini D, Leinisch F, Kumar A, Jiang J, Tokar EJ, Malone CC, Petrovich RM, Mason RP. Fluorescent proteins such as eGFP lead to catalytic oxidative stress in cells. Redox biology 2017; 12: 462–468

Gargiulo S, Greco A, Gramanzini M, Esposito S, Affuso A, Brunetti A, Vesce G. Mice anesthesia, analgesia, and care, Part II: anesthetic considerations in preclinical imaging studies. ILAR journal 2012; 53: E70-81

Gasparini SJ, Llonch S, Borsch O, Ader M. Transplantation of photoreceptors into the degenerative retina: Current state and future perspectives. Progress in retinal and eye research 2019; 69: 1–37

Gheorghe A, Mahdi L, Musat O. AGE-RELATED MACULAR DEGENERATION. Romanian journal of ophthalmology 2015; 59: 74–77

Ghildiyal M, Zamore PD. Small silencing RNAs: an expanding universe. Nature reviews. Genetics 2009; 10: 94–108

Gibson DG, Young L, Chuang R-Y, Venter JC, Hutchison CA, Smith HO. Enzymatic assembly of DNA molecules up to several hundred kilobases. Nature methods 2009; 6: 343–345

Goel K, Ploski JE. RISC-y Business: Limitations of Short Hairpin RNA-Mediated Gene Silencing in the Brain and a Discussion of CRISPR/Cas-Based Alternatives. Frontiers in molecular neuroscience 2022; 15: 914430

Graham L, Orenstein JM. Processing tissue and cells for transmission electron microscopy in diagnostic pathology and research. Nature Protocols. 2007; 2:2439-2450.

Grieger JC, Choi VW, Samulski RJ. Production and characterization of adeno-associated viral vectors. Nature protocols 2006; 1: 1412–1428

Gudapati K, Singh A, Clarkson-Townsend D, Phillips SQ, Douglass A, Feola AJ, Allen RS. Behavioral Assessment of Visual Function via Optomotor Response and Cognitive Function via Y-Maze in Diabetic Rats. Journal of visualized experiments: JoVE 2020

Gwilliam K, Sperber M, Perry K, Rose KP, Ginsberg L, Paladugu N, Song Y, Milon B, Elkon R, Hertzano R. A cell type-specific approach to elucidate the role of miR-96 in inner ear hair cells. Frontiers in audiology and otology 2024; 2

Gysens F, Ostyn L, Goeteyn E, Blondeel E, Nuyttens J, Wever O de, Bony E de, Crabbé A, Mestdagh P. Direct lysis of 3D cell cultures for RT-qPCR gene expression quantification. Scientific reports 2023; 13: 1520

Ha M, Kim VN. Regulation of microRNA biogenesis. Nature reviews. Molecular cell biology 2014; 15: 509–524

Ha T-Y. MicroRNAs in Human Diseases: From Cancer to Cardiovascular Disease. Immune network 2011; 11: 135–154

Hallam D, Hilgen G, Dorgau B, Zhu L, Yu M, Bojic S, Hewitt P, Schmitt M, Uteng M, Kustermann S, Steel D, Nicholds M, Thomas R, Treumann A, Porter A, Sernagor E, Armstrong L, Lako M. Human-Induced Pluripotent Stem Cells Generate Light Responsive Retinal Organoids with Variable and Nutrient-Dependent Efficiency. Stem cells (Dayton, Ohio) 2018; 36: 1535–1551

Haq W, Arango-Gonzalez B, Zrenner E, Euler T, Schubert T. Synaptic remodeling generates synchronous oscillations in the degenerated outer mouse retina. Frontiers in neural circuits 2014; 8: 108

Hasegawa Y, Mao W, Saha S, Gunner G, Kolpakova J, Martin GE, Futai K. Luciferase shRNA Presents off-Target Effects on Voltage-Gated Ion Channels in Mouse Hippocampal Pyramidal Neurons. eNeuro 2017; 4

Hauck B, Zhao W, High K, Xiao W. Intracellular viral processing, not single-stranded DNA accumulation, is crucial for recombinant adeno-associated virus transduction. Journal of virology 2004; 78: 13678–13686

Helwak A, Kudla G, Dudnakova T, Tollervey D. Mapping the human miRNA interactome by CLASH reveals frequent noncanonical binding. Cell 2013; 153: 654–665

Hoon M, Okawa H, Della Santina L, Wong ROL. Functional architecture of the retina: development and disease. Progress in retinal and eye research 2014; 42: 44–84

Hu X, Chen J, Dai W, Xiao Y, Chen X, Chen Z, Zhang S, Hu Y. PHLDA1-PRDM1 mediates the effect of lentiviral vectors on fate-determination of human retinal progenitor cells. Cellular and molecular life sciences: CMLS 2024; 81: 305

Huang K-C, Gomes C, Meyer JS. Retinal Ganglion Cells in a Dish: Current Strategies and Recommended Best Practices for Effective In Vitro Modeling of Development and Disease. Handbook of experimental pharmacology 2023; 281: 83–102

Huang P, Narendran S, Pereira F, Fukuda S, Nagasaka Y, Apicella I, Yerramothu P, Marion KM, Cai X, Sadda SR, Gelfand BD, Ambati J. The Learning Curve of Murine Subretinal Injection Among Clinically Trained Ophthalmic Surgeons. Translational vision science & technology 2022; 11: 13

Invergo BM, Montanucci L, Laayouni H, Bertranpetit J. A system-level, molecular evolutionary analysis of mammalian phototransduction. BMC evolutionary biology 2013; 13: 52

Issa SS, Shaimardanova AA, Solovyeva VV, Rizvanov AA. Various AAV Serotypes and Their Applications in Gene Therapy: An Overview. Cells 2023; 12

Jacobs GH. Evolution of colour vision in mammals. Philosophical transactions of the Royal Society of London. Series B, Biological sciences 2009; 364: 2957–2967

Jeon CJ, Strettoi E, Masland RH. The major cell populations of the mouse retina. The Journal of neuroscience: the official journal of the Society for Neuroscience 1998; 18: 8936–8946

Jin Z-B, Hirokawa G, Le Gui, Takahashi R, Osakada F, Hiura Y, Takahashi M, Yasuhara O, Iwai N. Targeted deletion of miR-182, an abundant retinal microRNA. Molecular vision 2009; 15: 523–533

Kallman A, Capowski EE, Wang J, Kaushik AM, Jansen AD, Edwards KL, Chen L, Berlinicke CA, Joseph Phillips M, Pierce EA, Qian J, Wang T-H, Gamm DM, Zack DJ. Investigating cone photoreceptor development using patient-derived NRL null retinal organoids. Communications biology 2020; 3: 82

Kalloniatis M, Nivison-Smith L, Chua J, Acosta ML, Fletcher EL. Using the rd1 mouse to understand functional and anatomical retinal remodelling and treatment implications in retinitis pigmentosa: A review. Experimental eye research 2016; 150: 106–121

Karali M, Guadagnino I, Marrocco E, Cegli R de, Carissimo A, Pizzo M, Casarosa S, Conte I, Surace EM, Banfi S. AAV-miR-204 Protects from Retinal Degeneration by Attenuation of Microglia Activation and Photoreceptor Cell Death. Molecular therapy. Nucleic acids 2020; 19: 144–156

Karali M, Peluso I, Gennarino VA, Bilio M, Verde R, Lago G, Dollé P, Banfi S. miRNeye: a microRNA expression atlas of the mouse eye. BMC genomics 2010; 11: 715

Karali M, Persico M, Mutarelli M, Carissimo A, Pizzo M, Singh Marwah V, Ambrosio C, Pinelli M, Carrella D, Ferrari S, Ponzin D, Nigro V, Di Bernardo D, Banfi S. High-resolution analysis of the human retina miRNome reveals isomiR variations and novel microRNAs. Nucleic acids research 2016; 44: 1525–1540

Kaspi H, Chapnik E, Levy M, Beck G, Hornstein E, Soen Y. Brief report: miR-290-295 regulate embryonic stem cell differentiation propensities by repressing Pax6. Stem cells (Dayton, Ohio) 2013; 31: 2266–2272

Kennedy B, Malicki J. What drives cell morphogenesis: a look inside the vertebrate photoreceptor. Developmental dynamics: an official publication of the American Association of Anatomists 2009; 238: 2115–2138

Kiani AK, Pheby D, Henehan G, Brown R, Sieving P, Sykora P, Marks R, Falsini B, Capodicasa N, Miertus S, Lorusso L, Dondossola D, Tartaglia GM, Ergoren MC, Dundar M, Michelini S, Malacarne D, Bonetti G, Dautaj A, Donato K, Medori MC, Beccari T, Samaja M, Connelly ST, Martin D, Morresi A, Bacu A, Herbst KL, Kapustin M, Stuppia L, Lumer L, Farronato G, Bertelli M. Ethical considerations regarding animal experimentation. Journal of preventive medicine and hygiene 2022; 63: E255-E266

Kim A, Pyykko I. Size matters: versatile use of PiggyBac transposons as a genetic manipulation tool. Molecular and cellular biochemistry 2011; 354: 301–309

Kim S, Lowe A, Dharmat R, Lee S, Owen LA, Wang J, Shakoor A, Li Y, Morgan DJ, Hejazi AA, Cvekl A, DeAngelis MM, Zhou ZJ, Chen R, Liu W. Generation, transcriptome profiling, and functional validation of cone-rich human retinal organoids. Proceedings of the National Academy of Sciences of the United States of America 2019; 116: 10824–10833

Kim Y-K, Kim VN. Processing of intronic microRNAs. The EMBO journal 2007; 26: 775–783

Kobat SG, Turgut B. Importance of Müller Cells. Beyoglu eye journal 2020; 5: 59–63

Kolb H, Nelson RF, Ahnelt PK, Ortuño-Lizarán I, Cuenca N. Webvision: The Organization of the Retina and Visual System. Salt Lake City (UT) 1995

Krichevsky AM, Sonntag K-C, Isacson O, Kosik KS. Specific microRNAs modulate embryonic stem cell-derived neurogenesis. Stem cells (Dayton, Ohio) 2006; 24: 857–864

Krol J, Busskamp V, Markiewicz I, Stadler MB, Ribi S, Richter J, Duebel J, Bicker S, Fehling HJ, Schübeler D, Oertner TG, Schratt G, Bibel M, Roska B, Filipowicz W. Characterizing light-regulated retinal microRNAs reveals rapid turnover as a common property of neuronal microRNAs. Cell 2010a; 141: 618–631

Krol J, Krol I, Alvarez CPP, Fiscella M, Hierlemann A, Roska B, Filipowicz W. A network comprising short and long noncoding RNAs and RNA helicase controls mouse retina architecture. Nature communications 2015; 6: 7305

Krol J, Loedige I, Filipowicz W. The widespread regulation of microRNA biogenesis, function and decay. Nature reviews. Genetics 2010b; 11: 597–610

Krützfeldt J, Poy MN, Stoffel M. Strategies to determine the biological function of microRNAs. Nature genetics 2006; 38 Suppl: S14-9

Lagos-Quintana M, Rauhut R, Yalcin A, Meyer J, Lendeckel W, Tuschl T. Identification of tissue-specific microRNAs from mouse. Current biology: CB 2002; 12: 735–739

Lamb TD. Why rods and cones? Eye (London, England) 2016; 30: 179–185

Lassoued A, Zhang F, Kurokawa K, Liu Y, Bernucci MT, Crowell JA, Miller DT. Cone photoreceptor dysfunction in retinitis pigmentosa revealed by optoretinography. Proceedings of the National Academy of Sciences of the United States of America 2021; 118

Lee RC, Feinbaum RL, Ambros V. The C. elegans heterochronic gene lin-4 encodes small RNAs with antisense complementarity to lin-14. Cell 1993; 75: 843–854

Lee Y, Ahn C, Han J, Choi H, Kim J, Yim J, Lee J, Provost P, Rådmark O, Kim S, Kim VN. The nuclear RNase III Drosha initiates microRNA processing. Nature 2003; 425: 415–419

Lee Y, Jeon K, Lee J-T, Kim S, Kim VN. MicroRNA maturation: stepwise processing and subcellular localization. The EMBO journal 2002; 21: 4663–4670

Lee Y, Kim M, Han J, Yeom K-H, Lee S, Baek SH, Kim VN. MicroRNA genes are transcribed by RNA polymerase II. The EMBO journal 2004; 23: 4051–4060

Levesque-Sergerie JP, Duquette M, Thibault C, Delbecchi L, Bissonnette N. Detection limits of several commercial reverse transcriptase enzymes: impact on the low- and high-abundance transcript levels assessed by quantitative RT-PCR. BMC molecular biology 2007; 8: 93.

Lewis BP, Burge CB, Bartel DP. Conserved seed pairing, often flanked by adenosines, indicates that thousands of human genes are microRNA targets. Cell 2005; 120: 15–20

Li L, Zhao H, Xie H, Akhtar T, Yao Y, Cai Y, Dong K, Gu Y, Bao J, Chen J, Zhang M, Zhong K, Xu W, Xue T. Electrophysiological characterization of photoreceptor-like cells in human inducible pluripotent stem cell-derived retinal organoids during in vitro maturation. Stem cells (Dayton, Ohio) 2021; 39: 959–974

Li S, Ma H, Yang F, Ding X. cGMP Signaling in Photoreceptor Degeneration. International journal of molecular sciences 2023; 24

Lim W-J, Kim KH, Kim J-Y, Jeong S, Kim N. Identification of DNA-Methylated CpG Islands Associated With Gene Silencing in the Adult Body Tissues of the Ogye Chicken Using RNA-Seq and Reduced Representation Bisulfite Sequencing. Frontiers in genetics 2019; 10: 346

Lin B, Masland RH, Strettoi E. Remodeling of cone photoreceptor cells after rod degeneration in rd mice. Experimental eye research 2009; 88: 589–599

Lin S-L, Miller JD, Ying S-Y. Intronic microRNA (miRNA). Journal of biomedicine & biotechnology 2006; 2006: 26818

Lin SW, Kochendoerfer GG, Carroll KS, Wang D, Mathies RA, Sakmar TP. Mechanisms of spectral tuning in blue cone visual pigments. Visible and raman spectroscopy of blue-shifted rhodopsin mutants. The Journal of biological chemistry 1998; 273: 24583–24591

Lin Y, Xu CL, Breazzano MP, Tanaka AJ, Ryu J, Levi SR, Yao K, Sparrow JR, Tsang SH. Progressive RPE atrophy and photoreceptor death in KIZ-associated autosomal recessive retinitis pigmentosa. Ophthalmic genetics 2020; 41: 26–30

Livak KJ, Schmittgen TD. Analysis of relative gene expression data using real-time quantitative PCR and the 2(-Delta Delta C(T)) Method. Methods (San Diego, Calif.) 2001; 25: 402–408

Lumayag S, Haldin CE, Corbett NJ, Wahlin KJ, Cowan C, Turturro S, Larsen PE, Kovacs B, Witmer PD, Valle D, Zack DJ, Nicholson DA, Xu S. Inactivation of the microRNA-183/96/182 cluster results in syndromic retinal degeneration. Proceedings of the National Academy of Sciences of the United States of America 2013; 110: E507-16

Lund E, Güttinger S, Calado A, Dahlberg JE, Kutay U. Nuclear export of microRNA precursors. Science (New York, N.Y.) 2004; 303: 95–98

Macaulay IC, Voet T. Single cell genomics: advances and future perspectives. PLoS genetics 2014; 10: e1004126

Marc RE, Jones BW, Watt CB, Strettoi E. Neural remodeling in retinal degeneration. Progress in retinal and eye research 2003; 22: 607–655

Martin-Fumadó C, Benet-Travé J, Morales-Ferrero JI, Arimany-Manso J. Medical professional liability in neurosurgery. Neurocirugia (English Edition) 2022

Masland RH. The neuronal organization of the retina. Neuron 2012; 76: 266–280

Mathur P, Yang J. Usher syndrome: Hearing loss, retinal degeneration and associated abnormalities. Biochimica et biophysica acta 2015; 1852: 406–420

Mayerl SJ, Bajgai S, Ludwig AL, Jager LD, Williams BN, Bacig C, Stoddard C, Sinha D, Philpot BD, Gamm DM. Human retinal organoids harboring IMPG2 mutations

exhibit a photoreceptor outer segment phenotype that models advanced retinitis pigmentosa. Stem cell reports 2022; 17: 2409–2420

McDougald DS, Duong TT, Palozola KC, Marsh A, Papp TE, Mills JA, Zhou S, Bennett J. CRISPR Activation Enhances In Vitro Potency of AAV Vectors Driven by Tissue-Specific Promoters. Molecular therapy. Methods & clinical development 2019; 13: 380–389

Meister M, Pine J, Baylor DA. Multi-neuronal signals from the retina: acquisition and analysis. Journal of neuroscience methods 1994; 51: 95–106

Michalakis S, Mühlfriedel R, Tanimoto N, Krishnamoorthy V, Koch S, Fischer MD, Becirovic E, Bai L, Huber G, Beck SC, Fahl E, Büning H, Paquet-Durand F, Zong X, Gollisch T, Biel M, Seeliger MW. Restoration of cone vision in the CNGA3-/- mouse model of congenital complete lack of cone photoreceptor function. Molecular therapy: the journal of the American Society of Gene Therapy 2010; 18: 2057–2063

Miyagishi M, Taira K. U6 promoter-driven siRNAs with four uridine 3' overhangs efficiently suppress targeted gene expression in mammalian cells. Nature biotechnology 2002; 20: 497–500

Mohan KV, Mishra A, Muniyasamy A, Sinha P, Sahu P, Kesarwani A, Jain K, Nagarajan P, Scaria V, Agarwal M, Akhter NS, Gupta C, Upadhyay P. Immunological consequences of compromised ocular immune privilege accelerate retinal degeneration in retinitis pigmentosa. Orphanet journal of rare diseases 2022; 17: 378

Molday RS, Moritz OL. Photoreceptors at a glance. Journal of cell science 2015; 128: 4039–4045

Moore CB, Guthrie EH, Huang MT-H, Taxman DJ. Short hairpin RNA (shRNA): design, delivery, and assessment of gene knockdown. Methods in molecular biology (Clifton, N.J.) 2010; 629: 141–158

Moshiri A. Animals Models of Inherited Retinal Disease. International ophthalmology clinics 2021; 61: 113–130

Mu X, Zhao S, Pershad R, Hsieh TF, Scarpa A, Wang SW, White RA, Beremand PD, Thomas TL, Gan L, Klein WH. Gene expression in the developing mouse retina by EST sequencing and microarray analysis. Nucleic acids research 2001; 29: 4983–4993

Nadal-Nicolás FM, Galindo-Romero C, Lucas-Ruiz F, Marsh-Amstrong N, Li W, Vidal-Sanz M, Agudo-Barriuso M. Pan-retinal ganglion cell markers in mice, rats, and rhesus macaques. Zoological research 2023; 44: 226–248

Naggert ASEN, Collin GB, Wang J, Krebs MP, Chang B. A mouse model of cone photoreceptor function loss (cpfl9) with degeneration due to a mutation in Gucy2e. Frontiers in molecular neuroscience 2022; 15: 1080136

Nakazawa Y, Saha S, Galvan DL, Huye L, Rollins L, Rooney CM, Wilson MH. Evaluation of long-term transgene expression in piggyBac-modified human T lymphocytes. Journal of immunotherapy (Hagerstown, Md.: 1997) 2013; 36: 3–10

Narayan DS, Ao J, Wood JPM, Casson RJ, Chidlow G. Spatio-temporal characterization of S- and M/L-cone degeneration in the Rd1 mouse model of retinitis pigmentosa. BMC neuroscience 2019a; 20: 46

Narayan DS, Chidlow G, Wood JPM, Casson RJ. Investigations Into Bioenergetic Neuroprotection of Cone Photoreceptors: Relevance to Retinitis Pigmentosa. Frontiers in neuroscience 2019b; 13: 1234

Newell-Price J, Clark AJ, King P. DNA methylation and silencing of gene expression. Trends in endocrinology and metabolism: TEM 2000; 11: 142–148

Newman AM, Gallo NB, Hancox LS, Miller NJ, Radeke CM, Maloney MA, Cooper JB, Hageman GS, Anderson DH, Johnson LV, Radeke MJ. Systems-level analysis of age-related macular degeneration reveals global biomarkers and phenotype-specific functional networks. Genome medicine 2012; 4: 16

Nickla DL, Wallman J. The multifunctional choroid. Progress in retinal and eye research 2010; 29: 144–168

Nieuwenhuis B, Laperrousaz E, Tribble JR, Verhaagen J, Fawcett JW, Martin KR, Williams PA, Osborne A. Improving adeno-associated viral (AAV) vector-mediated transgene expression in retinal ganglion cells: comparison of five promoters. Gene therapy 2023; 30: 503–519

Nishiguchi KM, Carvalho LS, Rizzi M, Powell K, Holthaus S-Mk, Azam SA, Duran Y, Ribeiro J, Luhmann UFO, Bainbridge JWB, Smith AJ, Ali RR. Gene therapy restores vision in rd1 mice after removal of a confounding mutation in Gpr179. Nature communications 2015; 6: 6006

O'Brien J, Hayder H, Zayed Y, Peng C. Overview of MicroRNA Biogenesis, Mechanisms of Actions, and Circulation. Frontiers in endocrinology 2018; 9: 402

O'Neal TB, Luther EE. Retinitis Pigmentosa. In: StatPearls. Treasure Island (FL): StatPearls Publishing, 2024

O'Neil D, Glowatz H, Schlumpberger M. Ribosomal RNA depletion for efficient use of RNA-seq capacity. Current protocols in molecular biology 2013; Chapter 4: Unit 4.19

Pang J, Dai X, Boye SE, Barone I, Boye SL, Mao S, Everhart D, Dinculescu A, Liu L, Umino Y, Lei B, Chang B, Barlow R, Strettoi E, Hauswirth WW. Long-term retinal function and structure rescue using capsid mutant AAV8 vector in the rd10 mouse, a model of recessive retinitis pigmentosa. Molecular therapy: the journal of the American Society of Gene Therapy 2011; 19: 234–242

Pardue MT, Allen RS. Neuroprotective strategies for retinal disease. Progress in retinal and eye research 2018; 65: 50–76

Parikh S, Le A, Davenport J, Gorin MB, Nusinowitz S, Matynia A. An Alternative and Validated Injection Method for Accessing the Subretinal Space via a Transcleral Posterior Approach. Journal of visualized experiments: JoVE 2016

Parnami K, Bhattacharyya A. Current approaches to vision restoration using optogenetic therapy. Frontiers in cellular neuroscience 2023; 17: 1236826

Paule MR, White RJ. Survey and summary: transcription by RNA polymerases I and III. Nucleic acids research 2000; 28: 1283–1298

Pavlou M, Schön C, Occelli LM, Rossi A, Meumann N, Boyd RF, Bartoe JT, Siedlecki J, Gerhardt MJ, Babutzka S, Bogedein J, Wagner JE, Priglinger SG, Biel M, Petersen-Jones SM, Büning H, Michalakis S. Novel AAV capsids for intravitreal gene therapy of photoreceptor disorders. EMBO molecular medicine 2021; 13: e13392

Pawlick JS, Zuzic M, Pasquini G, Swiersy A, Busskamp V. MiRNA Regulatory Functions in Photoreceptors. Frontiers in cell and developmental biology 2020; 8: 620249

Pearring JN, Salinas RY, Baker SA, Arshavsky VY. Protein sorting, targeting and trafficking in photoreceptor cells. Progress in retinal and eye research 2013; 36: 24–51

Peng YW, Hao Y, Petters RM, Wong F. Ectopic synaptogenesis in the mammalian retina caused by rod photoreceptor-specific mutations. Nature neuroscience 2000; 3: 1121–1127

Pennesi ME, Michaels KV, Magee SS, Maricle A, Davin SP, Garg AK, Gale MJ, Tu DC, Wen Y, Erker LR, Francis PJ. Long-term characterization of retinal degeneration

in rd1 and rd10 mice using spectral domain optical coherence tomography. Investigative ophthalmology & visual science 2012; 53: 4644–4656

Perkins BD, Fadool JM. Photoreceptor structure and development analyses using GFP transgenes. Methods in cell biology 2010; 100: 205–218

Peskova L, Jurcikova D, Vanova T, Krivanek J, Capandova M, Sramkova Z, Sebestikova J, Kolouskova M, Kotasova H, Streit L, Barta T. miR-183/96/182 cluster is an important morphogenetic factor targeting PAX6 expression in differentiating human retinal organoids. Stem cells (Dayton, Ohio) 2020

Phelan JK, Bok D. A brief review of retinitis pigmentosa and the identified retinitis pigmentosa genes. Molecular vision 2000; 6: 116–124

Popova E. ON-OFF Interactions in the Retina: Role of Glycine and GABA. Current neuropharmacology 2014; 12: 509–526

Poy MN, Eliasson L, Krutzfeldt J, Kuwajima S, Ma X, Macdonald PE, Pfeffer S, Tuschl T, Rajewsky N, Rorsman P, Stoffel M. A pancreatic islet-specific microRNA regulates insulin secretion. Nature 2004; 432: 226–230

Pritchard CC, Cheng HH, Tewari M. MicroRNA profiling: approaches and considerations. Nature reviews. Genetics 2012; 13: 358–369

Privalov PL, Crane-Robinson C. Forces maintaining the DNA double helix. European biophysics journal: EBJ 2020; 49: 315–321

Punzo C, Cepko C. Cellular responses to photoreceptor death in the rd1 mouse model of retinal degeneration. Investigative ophthalmology & visual science 2007; 48: 849–857

Purves D, Augustine GJ, Fitzpatrick D, Katz LC, LaMantia A-S, McNamara JO, Williams SM. Neuroscience. Sunderland (MA): Sinauer Associates, 2001

Qi Y, Dai X, Zhang H, He Y, Zhang Y, Han J, Zhu P, Zhang Y, Zheng Q, Li X, Zhao C, Pang J. Trans-Corneal Subretinal Injection in Mice and Its Effect on the Function and Morphology of the Retina. PloS one 2015; 10: e0136523

Qian X, Liu H, Fu S, Lu J, Hung Y-T, Turner C, Gu H, Chen R. AAV8-Mediated Gene Therapy Rescues Retinal Degeneration Phenotype in a Tlcd3b Knockout Mouse Model. Investigative ophthalmology & visual science 2022; 63: 11

Rabinowitz JE, Samulski J. Adeno-associated virus expression systems for gene transfer. Current opinion in biotechnology 1998; 9: 470–475

Rodrigues GA, Shalaev E, Karami TK, Cunningham J, Slater NKH, Rivers HM. Pharmaceutical Development of AAV-Based Gene Therapy Products for the Eye. Pharmaceutical research 2018; 36: 29

Ruether K, Feigenspan A, Pirngruber J, Leitges M, Baehr W, Strauss O. PKC{alpha} is essential for the proper activation and termination of rod bipolar cell response. Investigative ophthalmology & visual science 2010; 51: 6051–6058

Russell S, Bennett J, Wellman JA, Chung DC, Yu Z-F, Tillman A, Wittes J, Pappas J, Elci O, McCague S, Cross D, Marshall KA, Walshire J, Kehoe TL, Reichert H, Davis M, Raffini L, George LA, Hudson FP, Dingfield L, Zhu X, Haller JA, Sohn EH, Mahajan VB, Pfeifer W, Weckmann M, Johnson C, Gewaily D, Drack A, Stone E, Wachtel K, Simonelli F, Leroy BP, Wright JF, High KA, Maguire AM. Efficacy and safety of voretigene neparvovec (AAV2-hRPE65v2) in patients with RPE65-mediated inherited retinal dystrophy: a randomised, controlled, open-label, phase 3 trial. Lancet (London, England) 2017; 390: 849–860

Russell WMS, Burch RL. The principles of humane experimental technique. Potters Bar, Herts.: Universities Federation for Animal Welfare, 1992

Sahel J-A, Boulanger-Scemama E, Pagot C, Arleo A, Galluppi F, Martel JN, Degli Esposti S, Delaux A, Saint Aubert J-B de, Montleau C de, Gutman E, Audo I, Duebel J, Picaud S, Dalkara D, Blouin L, Taiel M, Roska B. Partial recovery of visual function in a blind patient after optogenetic therapy. Nature medicine 2021; 27: 1223–1229

Sanuki R, Onishi A, Koike C, Muramatsu R, Watanabe S, Muranishi Y, Irie S, Uneo S, Koyasu T, Matsui R, Chérasse Y, Urade Y, Watanabe D, Kondo M, Yamashita T, Furukawa T. miR-124a is required for hippocampal axogenesis and retinal cone survival through Lhx2 suppression. Nature neuroscience 2011; 14: 1125–1134

Saxena K, Rutar MV, Provis JM, Natoli RC. Identification of miRNAs in a Model of Retinal Degenerations. Investigative ophthalmology & visual science 2015; 56: 1820–1829

Schindelin, J., Arganda-Carreras, I., Frise, E., Kaynig, V., Longair, M., Pietzsch, T., Preibisch, S., Rueden, C., Saalfeld, S., Schmid, B., Tinevez, J. Y., White, D. J., Hartenstein, V., Eliceiri, K., Tomancak, P., & Cardona, A. Fiji: an open-source platform for biological-image analysis. Nature methods 2012; 9(7): 676–682.

Schnödt M, Büning H. Improving the Quality of Adeno-Associated Viral Vector Preparations: The Challenge of Product-Related Impurities. Human gene therapy methods 2017; 28: 101–108

Schwartz GW. Color vision: More than meets the eye. Current biology: CB 2021; 31: R948-R950

Shi C, Yuan X, Chang K, Cho K-S, Xie XS, Chen DF, Luo G. Optimization of Optomotor Response-based Visual Function Assessment in Mice. Scientific reports 2018; 8: 9708

Shi Y. Mammalian RNAi for the masses. Trends in genetics: TIG 2003; 19: 9–12

Simó R, Villarroel M, Corraliza L, Hernández C, Garcia-Ramírez M. The retinal pigment epithelium: something more than a constituent of the blood-retinal barrier—implications for the pathogenesis of diabetic retinopathy. Journal of biomedicine & biotechnology 2010; 2010: 190724

Slijkerman RWN, Song F, Astuti GDN, Huynen MA, van Wijk E, Stieger K, Collin RWJ. The pros and cons of vertebrate animal models for functional and therapeutic research on inherited retinal dystrophies. Progress in retinal and eye research 2015; 48: 137–159

Sontheimer EJ, Carthew RW. Silence from within: endogenous siRNAs and miRNAs. Cell 2005; 122: 9–12

Spencer WJ, Lewis TR, Pearring JN, Arshavsky VY. Photoreceptor Discs: Built Like Ectosomes. Trends in cell biology 2020; 30: 904–915

Stanca HT, Stanca S, Tabacaru B, Boruga M, Balta F. Bevacizumab in Wet AMD treatment: A tribute to the thirteen years of experience from the beginning of the anti-VEGF era in Romania. Experimental and therapeutic medicine 2019; 18: 4993–5000

Strauss O. The retinal pigment epithelium in visual function. Physiological reviews 2005; 85: 845–881

Sun AX, Crabtree GR, Yoo AS. MicroRNAs: regulators of neuronal fate. Current opinion in cell biology 2013; 25: 215–221

Sun Y, Luo Z-M, Guo X-M, Su D-F, Liu X. An updated role of microRNA-124 in central nervous system disorders: a review. Frontiers in cellular neuroscience 2015; 9: 193

Sundermeier TR, Palczewski K. The impact of microRNA gene regulation on the survival and function of mature cell types in the eye. FASEB journal: official publication of the Federation of American Societies for Experimental Biology 2016; 30: 23–33

Szymanski M, Barciszewska MZ, Erdmann VA, Barciszewski J. 5S Ribosomal RNA Database. Nucleic acids research 2002; 30: 176–178

Taylor, S. C., Nadeau, K., Abbasi, M., Lachance, C., Nguyen, M., & Fenrich, J. The Ultimate qPCR Experiment: Producing Publication Quality, Reproducible Data the First Time. Trends in biotechnology 2019; 37(7): 761–774.

Thaung C, Arnold K, Jackson IJ, Coffey PJ. Presence of visual head tracking differentiates normal sighted from retinal degenerate mice. Neuroscience letters 2002; 325: 21–24

Timmers AM, Newmark JA, Turunen HT, Farivar T, Liu J, Song C, Ye G-J, Pennock S, Gaskin C, Knop DR, Shearman MS. Ocular Inflammatory Response to Intravitreal Injection of Adeno-Associated Virus Vector: Relative Contribution of Genome and Capsid. Human gene therapy 2020; 31: 80–89

U.S. Food and Drug Administration, 2017: LUXTURNA™ - voretigene neparvovec-rzyl. Available from https://www.fda.gov/media/109487/download (Accessed: 02.09.2024)

van Heyningen V, Williamson KA. PAX6 in sensory development. Human molecular genetics 2002; 11: 1161–1167

Vasbinder MA, Locke P. Introduction: Global Laws, Regulations, and Standards for Animals in Research. ILAR journal 2016; 57: 261–265

Vasudevan S, Tong Y, Steitz JA. Switching from repression to activation: microRNAs can up-regulate translation. Science (New York, N.Y.) 2007; 318: 1931–1934

Veleri S, Lazar CH, Chang B, Sieving PA, Banin E, Swaroop A. Biology and therapy of inherited retinal degenerative disease: insights from mouse models. Disease models & mechanisms 2015; 8: 109–129

Verbakel SK, van Huet RAC, Boon CJF, Hollander AI den, Collin RWJ, Klaver CCW, Hoyng CB, Roepman R, Klevering BJ. Non-syndromic retinitis pigmentosa. Progress in retinal and eye research 2018; 66: 157–186

Verra DM, Sajdak BS, Merriman DK, Hicks D. Diurnal rodents as pertinent animal models of human retinal physiology and pathology. Progress in retinal and eye research 2020; 74: 100776

Vidigal JA, Ventura A. The biological functions of miRNAs: lessons from in vivo studies. Trends in cell biology 2015; 25: 137–147

Voisin A, Pénaguin A, Gaillard A, Leveziel N. Stem cell therapy in retinal diseases. Neural regeneration research 2023; 18: 1478–1485

Völkner M, Pavlou M, Büning H, Michalakis S, Karl MO. Optimized Adeno-Associated Virus Vectors for Efficient Transduction of Human Retinal Organoids. Human gene therapy 2021; 32: 694–706

Volland S, Esteve-Rudd J, Hoo J, Yee C, Williams DS. A comparison of some organizational characteristics of the mouse central retina and the human macula. PloS one 2015; 10: e0125631

Wakabayashi Y, Usui Y, Okunuki Y, Kezuka T, Takeuchi M, Iwasaki T, Ohno A, Goto H. Increases of vitreous monocyte chemotactic protein 1 and interleukin 8 levels in patients with concurrent hypertension and diabetic retinopathy. Retina (Philadelphia, Pa.) 2011; 31: 1951–1957

Wang X, Wang X, Varma RK, Beauchamp L, Magdaleno S, Sendera TJ. Selection of hyperfunctional siRNAs with improved potency and specificity. Nucleic acids research 2009; 37: e152

Wang Y, Wang X, Jiang Y, Liu R, Di Cao, Pan J, Luo Y. Identification of key miRNAs and genes for mouse retinal development using a linear model. Molecular medicine reports 2020; 22: 494–506

Wang Z. The guideline of the design and validation of MiRNA mimics. Methods in molecular biology (Clifton, N.J.) 2011; 676: 211–223

Ware AP, Satyamoorthy K, Paul B. CmirC update 2024: a multi-omics database for clustered miRNAs. Functional & integrative genomics 2024; 24: 133

Weaver S, Dube S, Mir A, Qin J, Sun G, Ramakrishnan R, Jones RC, Livak KJ. Taking qPCR to a higher level: Analysis of CNV reveals the power of high throughput qPCR to enhance quantitative resolution. Methods (San Diego, Calif.) 2010; 50: 271–276

Wells-Gray EM, Choi SS, Bries A, Doble N. Variation in rod and cone density from the fovea to the mid-periphery in healthy human retinas using adaptive optics scanning laser ophthalmoscopy. Eye (London, England) 2016; 30: 1135–1143

Westholm JO, Lai EC. Mirtrons: microRNA biogenesis via splicing. Biochimie 2011; 93: 1897–1904

Whitaker CM, Nobles G, Ishibashi M, Massey SC. Rod and Cone Connections With Bipolar Cells in the Rabbit Retina. Frontiers in cellular neuroscience 2021; 15: 662329

Williams DR. Imaging single cells in the living retina. Vision research 2011; 51: 1379–1396

Wohl SG, Jorstad NL, Levine EM, Reh TA. Müller glial microRNAs are required for the maintenance of glial homeostasis and retinal architecture. Nature communications 2017; 8: 1603

Woodard, LE, Wilson, MH. piggyBac-ing models and new therapeutic strategies. Trends in biotechnology 2015; 33(9): 525–533

Wright AF, Chakarova CF, Abd El-Aziz MM, Bhattacharya SS. Photoreceptor degeneration: genetic and mechanistic dissection of a complex trait. Nature reviews. Genetics 2010; 11: 273–284

Xia X, Guo X. Adeno-associated virus vectors for retinal gene therapy in basic research and clinical studies. Frontiers in medicine 2023; 10: 1310050

Xiang L, Zhang J, Rao F-Q, Yang Q-L, Zeng H-Y, Huang S-H, Xie Z-X, Lv J-N, Lin D, Chen X-J, Wu K-C, Lu F, Huang X-F, Chen Q. Depletion of miR-96 Delays, But Does Not Arrest, Photoreceptor Development in Mice. Investigative ophthalmology & visual science 2022; 63: 24

Xu S, Witmer PD, Lumayag S, Kovacs B, Valle D. MicroRNA (miRNA) transcriptome of mouse retina and identification of a sensory organ-specific miRNA cluster. The Journal of biological chemistry 2007; 282: 25053–25066

Yang S, Zhou J, Li D. Functions and Diseases of the Retinal Pigment Epithelium. Frontiers in pharmacology 2021; 12: 727870

Yi R, Qin Y, Macara IG, Cullen BR. Exportin-5 mediates the nuclear export of pre-microRNAs and short hairpin RNAs. Genes & development 2003; 17: 3011–3016

Yoo AS, Sun AX, Li L, Shcheglovitov A, Portmann T, Li Y, Lee-Messer C, Dolmetsch RE, Tsien RW, Crabtree GR. MicroRNA-mediated conversion of human fibroblasts to neurons. Nature 2011; 476: 228–231

Yu D-Y, Cringle SJ, Balaratnasingam C, Morgan WH, Yu PK, Su E-N. Retinal ganglion cells: Energetics, compartmentation, axonal transport, cytoskeletons and vulnerability. Progress in retinal and eye research 2013; 36: 217–246

Yu-Wai-Man P, Newman NJ, Carelli V, Moster ML, Biousse V, Sadun AA, Klopstock T, Vignal-Clermont C, Sergott RC, Rudolph G, La Morgia C, Karanjia R, Taiel M, Blouin L, Burguière P, Smits G, Chevalier C, Masonson H, Salermo Y, Katz B, Picaud S, Calkins DJ, Sahel J-A. Bilateral visual improvement with unilateral gene therapy injection for Leber hereditary optic neuropathy. Science translational medicine 2020; 12

Zhang C-J, Xiang L, Chen X-J, Wang X-Y, Wu K-C, Zhang B-W, Chen D-F, Jin G-H, Zhang H, Chen Y-C, Liu W-Q, Li M-L, Ma Y, Jin Z-B. Ablation of Mature miR-183 Leads to Retinal Dysfunction in Mice. Investigative ophthalmology & visual science 2020; 61: 12

Zhang L, Liu W, Wang H-Y, Qiang W, Wang R, Cui Z-L, Zhang Z-M. The temporal progression of retinal degeneration and early-stage idebenone treatment in the Pde6brd1/rd1 mouse model of retinal dystrophy. Scientific reports 2024; 14: 2019

Zhang Y, Zhang R, Su B. Diversity and evolution of MicroRNA gene clusters. Science in China. Series C, Life sciences 2009; 52: 261–266

Zhu Q, Sun W, Okano K, Chen Y, Zhang N, Maeda T, Palczewski K. Sponge transgenic mouse model reveals important roles for the microRNA-183 (miR-183)/96/182 cluster in postmitotic photoreceptors of the retina. The Journal of biological chemistry 2011; 286: 31749–31760

Zuzic M, Striebel J, Pawlick JS, Sharma K, Holz FG, Busskamp V. Gene-independent therapeutic interventions to maintain and restore light sensitivity in degenerating photoreceptors. Progress in retinal and eye research 2022; 90: 101065

9 Acknowledgements

I would like to sincerely thank my advisor, Prof. Dr. Volker Busskamp, for giving me the opportunity to conduct my Ph.D. research in his laboratory. His support and guidance during this time has been very valuable and I am grateful for the knowledge and experience I have gained under his mentorship.

I would also like to thank the current and former members of the Busskamp Lab. Especially, Kritika Sharma, Johannes Striebel, Elizaveta Podoliak, Jasmin Zorn, Dr. Rouhollah Habibey, Dr. Robert Prior, Dr. Sarah Kunze and Dr. Kirsten Harmening for their support. Their contributions made my time in Bonn unforgettable. A special thanks goes to Dr. Sarah Kunze for her great support during my experiments and the time she invested in helping and supporting me.

I want to thank my TAC committee members, Prof. Dr. Dr. Knut Stieger, Prof. Dr. Valentin Stein and Prof. Dr. Gunther Hartmann for their valuable discussions and advice during my TAC meetings. I would also like to thank Prof. Dr. Stylianos Michalakis for the collaboration and for providing the AAVs necessary for my research.

I want to thank the Bonn International Graduate School of Neuroscience for the scientific training and resources provided during my studies.

I am forever grateful to my family for their unconditional love and support. A special thank you also goes out to my friends who have always been there for me, especially Kritika Sharma for always reminding me to believe in myself and showing me that with the right friends by your side, anything is possible, but also to my friends Maximilian Stötzel, Liv Zimmermann, Lena Soppa, Alisa Rosenstengel and Ann-Sophie Giel who continued to support me on this journey even after we parted ways after the Master's program. Finally, I would like to take this opportunity to express my deepest appreciation to my partner, Joel Opitz, who has supported me tirelessly and unconditionally every step of the way.